SOFT X-RAY APPEARANCE POTENTIAL SPECTROSCOPY

by

K. N. RAMACHANDRAN

Submitted in partial fulfilment of the requirements
for the degree of Doctor of Philosophy

Department of Electrical Engineering
Faculty of Science and Engineering
University of Ottawa
Ottawa Canada
1972

This work is dedicated to the Security Staff of Shirley Bay, who kept me constant company during the countless quiet hours, when most of the experiments took shape.

ACKNOWLEDGEMENTS

It was Prof. Glinski, who introduced me to the fascinating field of Electron Beam Technology. I thank him for all his encouragements during the initial stages of my work and for providing me with the equipment necessary for the project.

I am grateful to my supervisors, Dr. C. D. Cox and Prof. P. M. Thompson, for guiding me through my work and for quickly correcting the thesis manuscripts.

I owe special thanks to Dr. Cox, who in addition to supervision and guidance, provided me access to all the facilities needed to materialize a project of this nature.

It is my pleasure to thank all the members of the various sections and groups of the Communications Research Centre, Shirley Bay, especially the Failure Analysis Group, who showed kindness and understanding.

I also wish to thank Mr. Le Henaff for his friendly advice and help.

I gratefully acknowledge the financial assistance for my study in Canada, provided by the Commonwealth Scholarships and Fellowships Committee.

A B S T R A C T

X-ray appearance potential spectroscopy using low energy electron excitation is a simple technique for surface analysis, particularly of light elements. The method also provides information about the valence states of elements.

The specimen is bombarded by electrons whose energy is continuously varied in the range, 0 to 1000 eV. As the energy is increased past an absorption edge (or appearance potential) of the specimen, a characteristic radiation is added to the general level of bremsstrahlung. The appearance potential is identified by plotting the total x-ray yield against electron energy. A small change in slope will occur at the appearance potential, which can be enhanced by differentiating the total yield. This is achieved by modulating the electron energy and detecting the synchronous component of the total x-ray yield measured by a windowless photon detector.

All light elements from Beryllium to Oxygen and a few heavier elements have been detected. The observed appearance potential spectra exhibited marked structure related to the density distribution of empty states in the valence bands and the valence states of the elements. Although the technique is potentially capable of detecting all elements, some elements were shown to have very low sensitivity.

C O N T E N T S

LIST OF SYMBOLS

A	energy absorbed by an atom
c	velocity of light = 3×10^{8} m sec^{-1}
C	Capacitance
e	electronic charge = 1.6×10^{-19} coul.
	small sinusoidal signal
E	energy of electron or quantum
f	frequency
h	Planck's constant = 6.6×10^{-27} erg sec
I	current
	intensity
j	quantum number
k	Boltzmann's constant = 1.38×10^{-16} erg $^{o}K^{-1}$
l	quantum number
m	electronic mass = 9.04×10^{-31} Kg
M	molecular weight of gas
	matrix pertaining to electronic transitions
n	quantum number
	density of energy levels
	number of atoms in a unit volume
p	pressure
	electronic momentum
	probability
P	probability
R	ratio of probabilities
S	surface of constant energy
t	time

T	temperature
v, V	voltage
w	fluorescent yield
x	distance
Z	atomic number impedance
α	energy absorbed by an atom in a transition
ε	energy level in the valence band
η	efficiency of x-ray production displacement of electron cloud
θ	angle of incidence of radiation
λ	wavelength of radiation
μ	absorption coefficient
ν	frequency specific rate of striking of molecules
σ	surface charge density
τ	time constant
ϕ	work function
ψ	wave function
ω	angular frequency
Ω	volume of unit cell

CHAPTER 1. X-RAY APPEARANCE POTENTIAL SPECTROSCOPY

X-rays are generated when energetic electrons interact with matter. Though the process is inefficient, it is one of the most widely exploited interactions, especially in the field of material analysis. Not long after their discovery by Röntgen in 1895, it was established that x-rays are produced as a result of the return to equilibrium of atoms excited to higher energy states, and this gives rise to x-ray spectra characteristic of each element. In conventional x-ray spectroscopy, this characteristic radiation is resolved like fingerprints to identify an unknown element. This technique has been developed to a high degree of sophistication over the past years, and detection sensitivities of the order of 10^{-15} gm have been achieved.

A recently applied approach is to measure the threshold value of incident electron energy at which the atom is excited to give off characteristic radiation. This threshold potential, which corresponds to the binding energy of an electron to its nucleus, has recently been named Appearance Potential, even though earlier workers used the terms Critical Potential, Excitation Potential and Absorption Edge. When the energy of the incident electrons is below the appearance potential of the target, the atoms are not excited, and there is no characteristic radiation. Instead, some continuous radiation or bremsstrahlung is emitted as a result of the slowing down of the electrons by the target, this being nearly independent of the target material itself. Now, if the electron energy is raised above the appearance

potential of the target, atoms are excited and as a result, characteristic radiation begins to appear. Appearance potential spectroscopy is based on this increase in the x-ray output which occurs at the threshold value of incident electron energy. The technique consists of measuring the *total yield* without any energy dispersion and plotting it against electron energy. The excitation curve so obtained will exhibit a break or discontinuity corresponding to the appearance potential. The relatively small changes in slope of the excitation curve can be greatly enhanced by differentiation of the total yield with respect to electron energy so that precise location of the break is possible. Depending on its electron configuration, an element will have a number of such appearance potentials which are distinct and different from those of other elements.

1.1 History of Development

The first systematic study of soft x-ray critical potentials was made by Richardson and Bazzoni[1] and Kurth[2], in 1921. X-rays from polished metal targets were excited by electrons accelerated from a hot Tungsten filament. A metallic cup facing the target was used to collect a large part of the emitted radiation, the resulting photoelectron current being measured by a sensitive electrometer. A system of properly biased vanes and grids was interposed between the target and detector so as to prevent electrons and ions from reaching the detector while allowing radiation to pass through. The entire structure was enclosed in a glass tube and pumped continuously to a very high vacuum in order to keep the target face free from contamination and to reduce the disturbance caused by residual

ions. The energy of the electrons was varied in small steps from a few volts to several hundred volts and the photoelectron yield per unit thermionic current was plotted against electron energy to obtain the excitation curve for the target. It displayed on a monotonically increasing background, several "breaks" or changes in slope which were reproducible within experimental error. A break was always found to occur corresponding to the K, L, M etc. electron levels of the target material, known by spectroscopic methods. Many more breaks were found, whose origin was not explained at that time.

In the succeeding years, many eminent investigators[3-20] repeated the experiment under carefully controlled conditions and tabulations of critical potentials to good accuracy were made for various elements. In 1926 Compton and Thomas[21] obtained the derivative of the excitation curve which greatly enhanced the structure near the critical potential. In 1932 Skinner[22] applied the technique to light elements like Lithium and sought to explain the anomalous structure close to the K edge.

The initial burst of activity on the critical potential analysis gradually faded, probably because of its poor sensitivity and versatility compared to diffraction crystal type x-ray spectrometers. It was in 1952 that Shinoda et al[23,24,25] revived the technique using vacuum tube circuits and electronic differentiation, as a result of which, the excitation curve could be displayed on a cathode ray tube. In 1969 Voparil[26] showed how electronic differentiation could be achieved by a modulated excitation followed by

detection of the harmonic content of the total x-ray yield. He, however, excited the target by a beam of modulated x-radiation rather than electrons. Park, Houston and Schreiner[27-30] demonstrated in 1970, the effectiveness of the modulated electron beam energy technique in obtaining the fine structure with high signal to noise ratio. They also designated the technique as Appearance Potential Spectroscopy (APS), and it has now been accepted as a relatively simple but powerful method of surface analysis.

1.2 The Present Work

The present work was started with the object of developing a scanning electron microprobe instrument based on the appearance potential technique. It was soon realized that the basic sensitivity of detection by the method is too poor to achieve this. Although the lowest current at which signals were detected was 15 μA, the normal currents required for most of the investigations were of the order of 1 mA, obtained from a flood source of electrons. By a proper design of the detector configuration and the electrometer circuits, the overall sensitivity was optimized, and the apparatus was able to detect all light elements from Beryllium to Oxygen and also a number of heavier elements. Oxidation studies made on a Nickel specimen showed that a few monolayers (10 $\mathring{A}$) of Oxygen can easily be detected. Experiments on Iron and its oxides and on an Iron Nickel alloy demonstrated the unique potential capability of the technique to distinguish between the different valence states of an element. Considerable anomalous structure was found in the low and high energy ends of the appearance potential spectra of many specimens.

This being primarily an experimental investigation oriented towards material analysis, no effort was made, either to obtain the detailed fine structure of all light elements, or to provide explanation for the observed structure in terms of quantum physics. Suggestions are made for future development, such as ion excitation with focused beams and the exploration of possible structure in specimen current and in back scattered electron yield.

CHAPTER 2. METHODS OF X-RAY ANALYSIS

X-ray analysis is basically a non-destructive method of determining the chemical composition of an unknown sample. This is done by temporarily disturbing the electronic structure of the atoms by a suitable primary excitation, which induces only a minimum (usually negligible) amount of permanent damage. The excited atoms return to their normal state in a very short time, of the order of 10^{-15} second, causing characteristic x-radiation to be emitted. The identification of the species hinges on the accurate determination of the energy of the characteristic x-rays. Depending on the way in which this is done, x-ray analysis can be classified into two distinct groups, namely, 1) Emission Analysis and 2) Absorption Analysis. Each of these is further subdivided, based on the mode of primary excitation and the scheme used for the detection of emitted radiation.

This chapter presents a brief review of the conventional methods of x-ray analysis, and the different types of x-ray detectors in use. The technique of appearance potential spectroscopy is described in detail in the last section.

2.1 X-ray Emission Analysis

X-ray emission analysis is the most widely used method for the x-ray analysis of materials. The primary excitation is in the form of an electron beam of several kilo electron volts energy and a few microamperes current focused to a micron sized spot on the specimen surface. The emitted radiation is resolved in wavelength

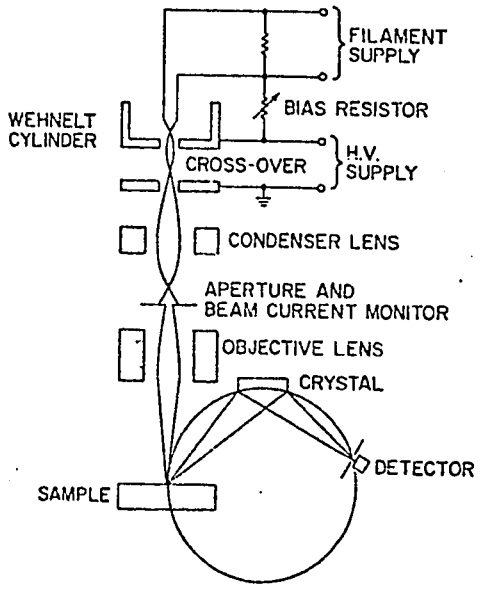

(a) Schematic Diagram

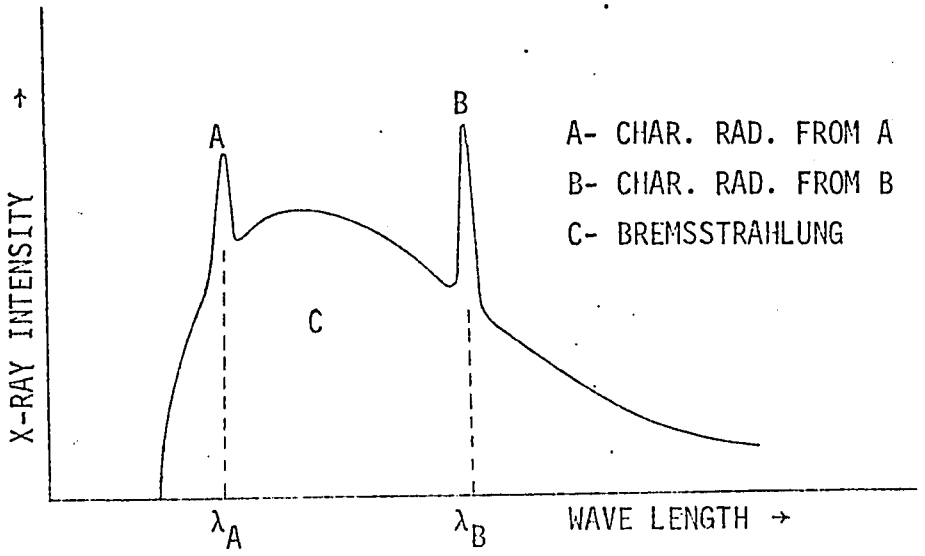

(b) A Typical Emission Spectrum

Fig. 2.1 X-Ray Emission Analysis

by a suitable energy dispersive system, usually a diffracting crystal (Fig. 2.1). Depending on its lattice spacing and the orientation of the incident radiation, the crystal focuses only a narrow wavelength of emitted radiation. These filtered rays are detected by a suitable x-ray counter. The emission spectrum is obtained by plotting the x-ray intensity which is proportional to the count rate, against the angle of diffraction which is related to the wavelength of radiation. The characteristic emission from the elements present in the sample will appear as sharp peaks in a background of continuous radiation, the height of the peak being proportional to the concentration of the element. Crystals of various lattice spacings have been made in a variety of sizes and shapes to yield excellent energy dispersion. References 31 and 32 give details of construction and performance of crystal spectrographs.

Probing the sample with a finely focused beam of electrons imparts a considerable amount of versatility and elegance to this method of microanalysis. In a static spot analysis, the beam is positioned on a given point on the specimen and the x-ray emission spectrum is obtained by plotting the counter output as a function of the diffracting angle. From the position of the peaks and their relative heights, the composition of elements in the probed volume can be computed. Alternatively, the distribution of an element on the sample face can be obtained by scanning the probe over the desired area. The detecting system is set to accept only the characteristic radiation from the element under consideration, and

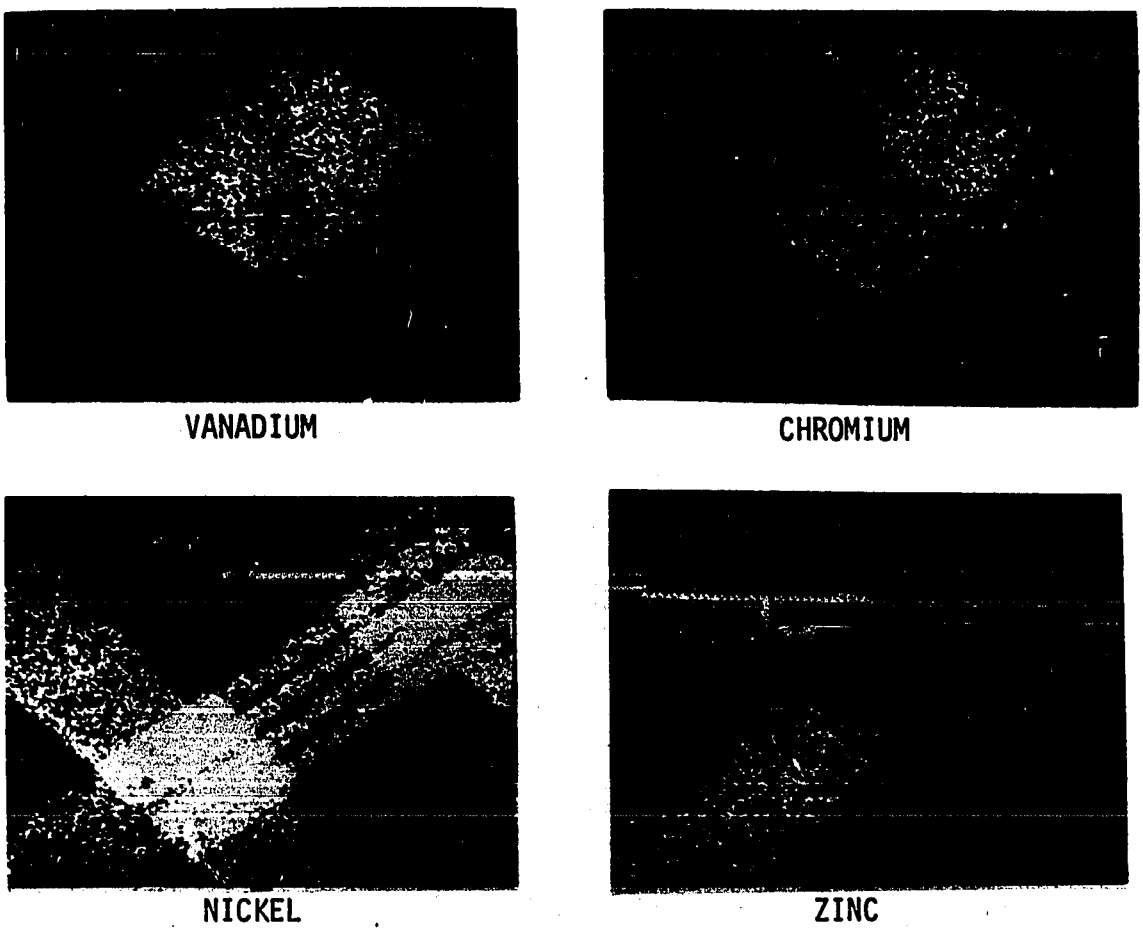

Fig. 2.2 An Example of Element Distribution Micrographs, obtained from a VO_2 Switching Device, using the CRC Microprobe

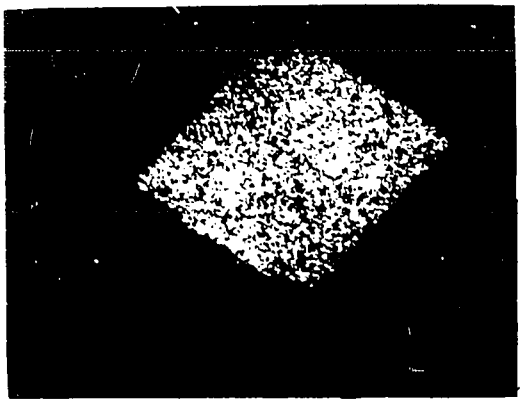

VANADIUM

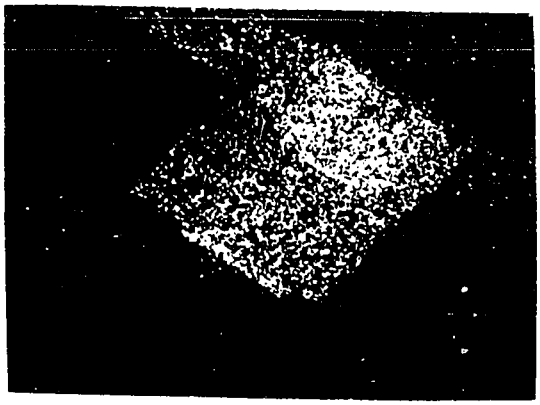

CHROMIUM

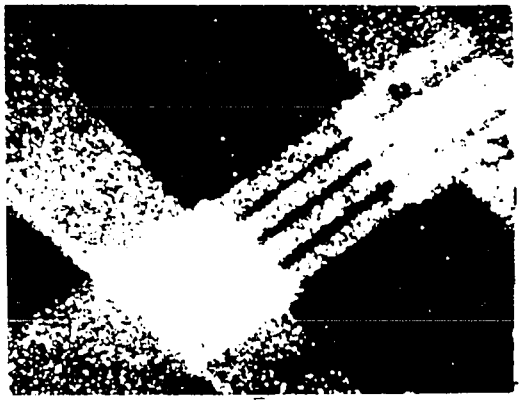

NICKEL

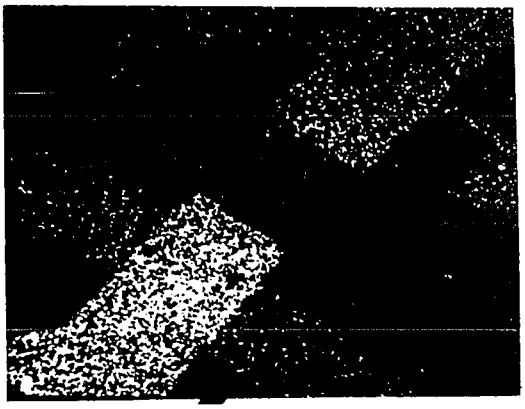

ZINC

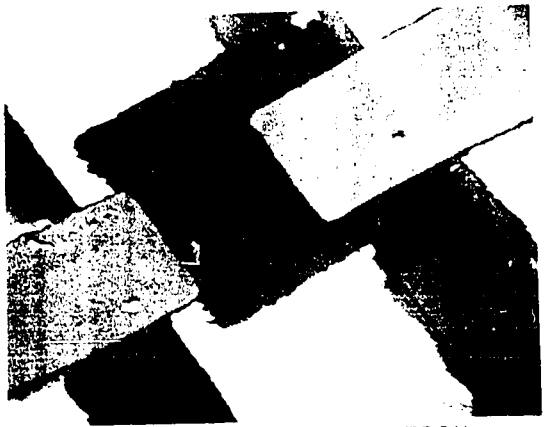

BACK SCATTERED ELECTRON
MICROGRAPH

Zn

Ni

Cr

2.5 WAVE LENGTH Å 2.0 1.5

A TYPICAL STATIC SPOT ANALYSIS

X-Ray Spectra of Element Distribution Micrographs, obtained
[illegible] Switching Device, using the CRC Microprobe

the output of the x-ray recorder is used to intensity modulate a cathode ray tube which is scanned in synchronism with the probe. Separate micrographs showing the distribution of various elements can be made in this way. Fig. 2.2 illustrates such micrographs obtained from a switching device made from Vanadium dioxide. A back-scattered electron picture of the same area and a typical static spot analysis result are also shown in the figure.

By choosing appropriate crystals, good resolution and sensitivity approaching 10^{-15} gm are attainable for the detection of high and medium atomic number elements. The main reasons for the poor performance at the low end of the periodic table ($Z<10$) are

1) decreased x-ray production efficiency,

2) the need for ruled gratings instead of crystals, with a consequent loss of sensitivity, and

3) the steep fall in the transmission of soft x-rays through the counter window used for detection.

Some of these problems can be overcome by employing large solid angle, non-dispersive type detectors and pulse height distribution analysis. This makes use of the pulse output at the detector being proportional to the energy of the x-ray quanta detected. A representation of the x-ray energy spectrum is obtained by plotting the number of counts per second in the energy interval $E+\Delta E$ and E, against E. The resolution attained in this manner is far inferior to that of a ruled grating or crystal. However, adjacent elements like Carbon, Nitrogen and Oxygen can be resolved when they are present

in reasonable proportions[31].

2.1.1 Differential Mirror Method

Yet another way in which dispersive analysis of radiation emitted from a sample could be carried out, has been suggested by Borovskii[33]. This makes use of the dependence of the critical angle of total internal reflection on the wavelength of x-rays. The arrangement is shown in Fig. 2.3. Metallic surfaces at glancing angles are used to reflect the radiation selectively. Two mirrors M_1 and M_2 are used, one at a time, to reflect the radiation before being measured. M_1 has a critical wavelength which lies just below the characteristic wavelength of the element being analyzed. The intensity measured in this case consists of characteristic radiation plus all radiations of lower energy. The second measurement with the mirror M_2 which has a cut off wavelength just above the characteristic wavelength, gives the total contribution due to all the radiations of lower energy. The difference between the two readings gives the intensity of characteristic radiation alone. The use of a windowless photon detector ensures efficient measurement of soft radiation. Alloys containing Beryllium and Boron have been analyzed by this method.

2.2 X-ray Fluorescence Analysis

In the x-ray fluorescence analysis, the primary excitation is in the form of a beam of x-rays of sufficient energy, obtained from a standard x-ray tube, as shown in Fig. 2.4. A roughly monochromatic beam of x-rays is obtained by separating out the intense characteristic radiation from the target using a thin window filter

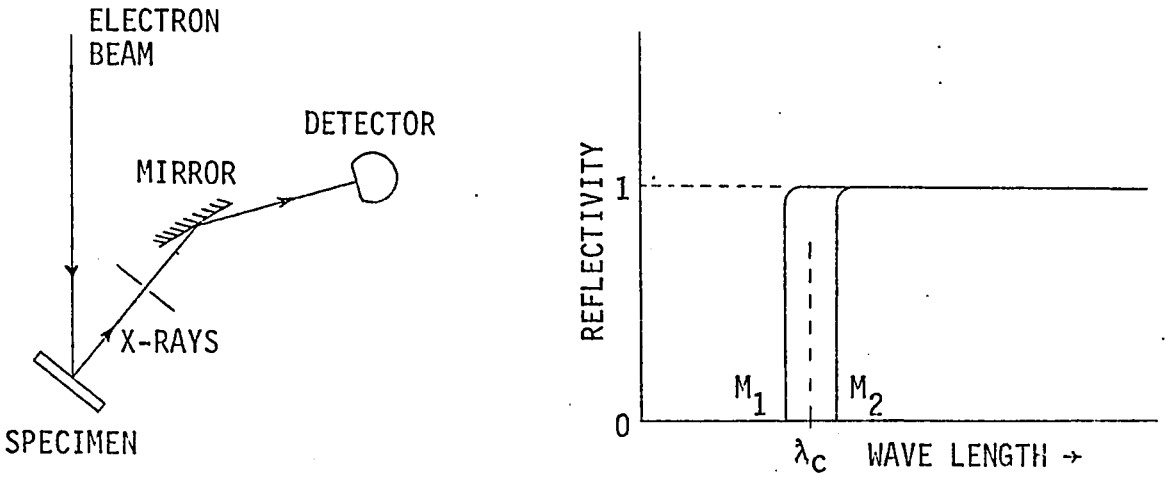

Fig. 2.3 Differential Mirror Method of Energy Dispersive Detection

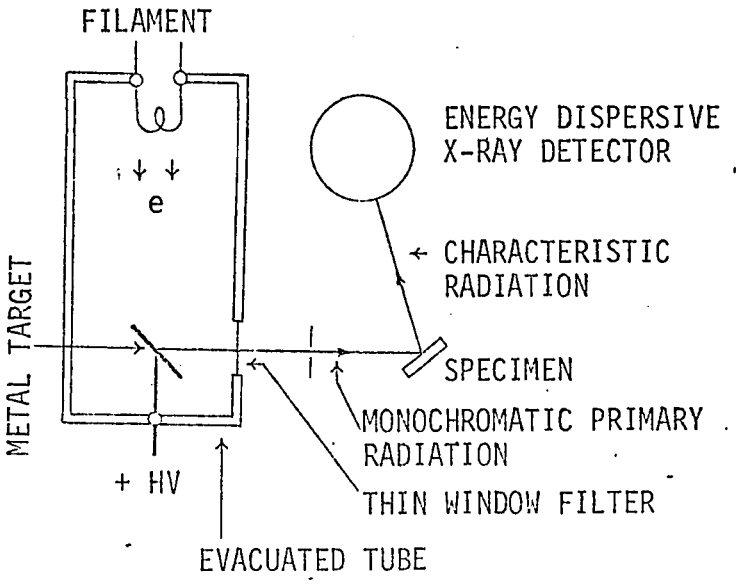

Fig. 2.4 Schematic Diagram of X-ray Fluorescence Analysis

of suitable material. The monochromatic primary radiation excites characteristic x-rays from the sample, and these are analyzed by an energy dispersive system as in the previous method. Ref. 31 discusses the variations of the technique and gives examples of analysis.

The fluorescence technique has a few note-worthy advantages. The specimen can be located outside vacuum, since x-rays* are not attenuated to any appreciable extent in air. Insulating specimens can readily be examined by this method, because an x-ray beam, unlike an electron beam, does not cause accumulation of charge on the specimen. The absence of continuous radiation or bremsstrahlung in the case of x-ray fluorescence reduces the unwanted background, and greatly improves the detection sensitivity.

The advantages mentioned above are overshadowed by the lack of facility with which x-rays can be collimated and deflected. There is no counterpart of lenses to focus x-rays. A system of curved, totally reflecting mirrors has the capability to focus, but is very inefficient. Furthermore, x-rays cannot be deflected like an electron beam, and the only way of positioning the beam on the sample is by mechanical means.

2.3 X-ray Absorption Analysis

If a thin section of an element is irradiated by x-rays, some of it is absorbed and some transmitted. The absorption spectrum obtained by plotting the loss of intensity against wavelength is characterized by abrupt discontinuities which are called absorption

* but not very soft x-rays

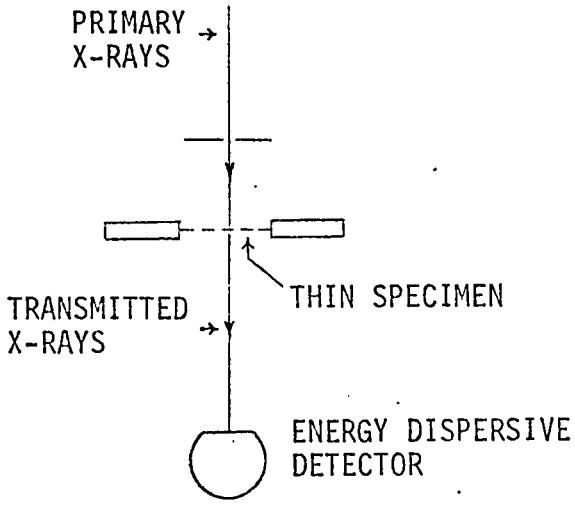

(a) Schematic Diagram

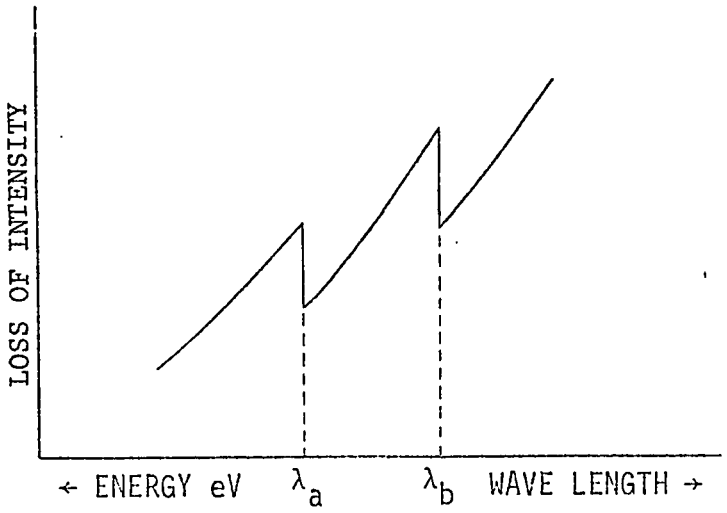

(b) A Simplified Absorption Spectrum

Fig. 2.5 X-ray Absorption Analysis.

edges (Fig. 2.5). As mentioned in Chapter 1, this value corresponds to the threshold energy at which the atoms can be excited from their ground state. The incident radiation is therefore strongly absorbed when its wavelength is below the absorption edge, the extra energy being utilized in exciting the atoms. The absorption curve thus exhibits step increases at the critical values of wavelength, which are characteristic of the elements present in the sample.

In absorption analysis, the primary radiation obtained from an x-ray tube falls on a specimen which is prepared in the form of a very thin foil or film. The transmitted intensity is measured as a function of wavelength, using an energy dispersive detector. If the primary beam energy spectrum is separately measured by removing the specimen, the absorption coefficient can be computed and plotted as a function of wavelength. The locations of the discontinuities identify the elements present, whereas their relative heights provide a quantitative measure of the concentrations. References 31 and 32 provide detailed information on x-ray absorption analysis.

The absorption analysis presents a convenient and direct means of observing electron binding energies in an atom. It can easily be applied to the gas and liquid phases of the specimen, as there is no vacuum requirement.

The preparation of the thin absorber specimen is the most difficult and involved process. Metals can be formed into micron-thick foils; but other materials have to be deposited by evaporation

or similar processes on to a supporting film, which itself has a low absorption in the wavelength range of interest.

2.4 Detection of X-rays

There are many ways in which x-rays can be detected and measured. The most important methods are reviewed in this section with particular reference to those suitable for appearance potential spectroscopy.

2.4.1 The Gas Filled Counter

This is the most commonly used type of x-ray detector. The ionization of a gas at low pressure under the action of an x-ray quantum is the basic process involved in detection. As shown in Fig. 2.6, it consists of a tube having a thin window through which x-rays pass with little attenuation. The central electrode, called the collector, is maintained at a high positive potential with respect to the walls. X-ray quanta entering the chamber interact with gas atoms and cause primary ionization. The primary ions, accelerated by the high collector field, produce further ionization, resulting in a chain reaction. As a result, a greatly amplified pulse of current will be produced at the collector electrode, which is detected and counted by electronic circuits. By a proper choice of gas mixture and pressure, the performance can be optimized for detecting a certain energy range of x-rays. The pulse rate registered at the output is proportional to the x-ray intensity, whereas the pulse height is a measure of the energy of the quantum. A typical gas mixture for the detection of low energy x-rays is made up of

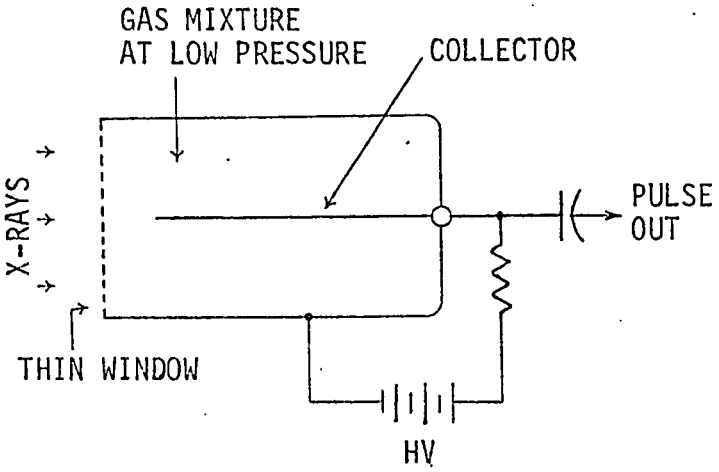

Fig. 2.6 The Gas filled Counter

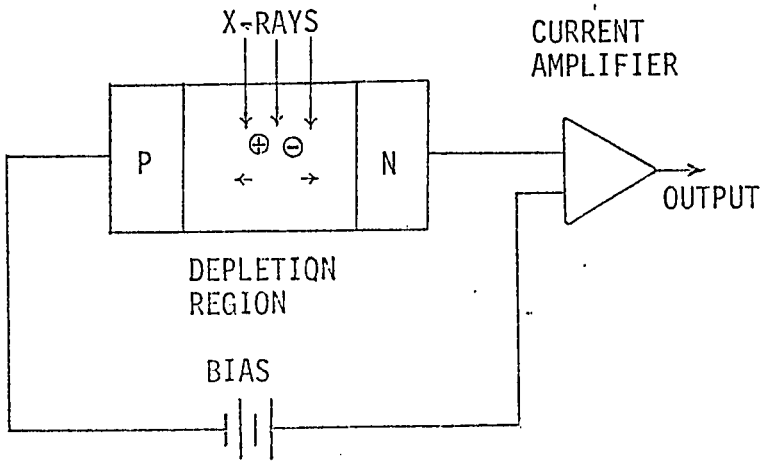

Fig. 2.7 The Semiconductor Detector

10% Argon and 90% Methane at a pressure of about 200 microns. Best performance is obtained by maintaining a dynamic pressure and replacing the gas mixture at a slow but constant rate.

The counting efficiency for the x-ray quanta *entering the tube* is close to unity. However, the low energy detection limit is decided by the transmission through the window. Even with a formvar film of half a micron thickness, the transmission of x-rays drops to 30% at 500 eV and to less than 5% at 250 eV[34]. Such windows are extremely delicate and require careful handling during chamber evacuation. There is also the problem of sealing and permeation through the film itself. For ultrahigh vacuum compability, multiple windows would be needed, which further cuts down the transparency. For conventional use, the gas counters are made with a small slit window. A detector for appearance potential spectroscopy would need as large a window as practicable, and the fragility of the film poses additional problems. Recent developments[35,36] in ultrathin organic films supported between fine meshes of high transmission, appear promising. Yet another serious disadvantage of this type of detector is the sudden change in the transmission of radiation in the vicinity of the absorption edges of the constituents of the film, such as Oxygen, Nitrogen and Carbon. This will adversely interfere with the appearance potential spectrum of these elements, when present in the sample.

2.4.2 The Semiconductor Detector

The semiconductor detector is based on the production of

hole electron pairs in a semiconducting material under the action of x-ray photons. The induced carriers are collected by a suitable field and the resulting current pulse output is a measure of the photon energy (Fig. 2.7). P-N junctions of both Germanium and Silicon can be used as detectors. An external potential difference of a few hundred volts is usually necessary to ensure good efficiency of collection. The leakage current associated with this high bias gives rise to the background noise in the device. In order to reduce this noise level, the device, together with the low noise pre-amplifier, is cooled to liquid Nitrogen temperatures.

The inherent low energy limit of detection is very low, as the ionization energy of a semiconductor is of the order of a few volts. However, in practice, a Beryllium foil window is necessary to separate the cooled detector from the vacuum, and this puts a limit on the transmission of low energy radiation. In a properly designed cooling system that avoids a window altogether, this limation can be overcome. Recent developments in Lithium-drifted Silicon devices have produced low energy detectors of low noise and high efficiency[34]. These are also available with large detecting surfaces suitable for appearance potential spectroscopy. However, the need for continuous cooling adds considerable complexity in design, and reduces their attractiveness.

2.4.3 The Scintillation Counter

There is a wide range of materials which scintillate when irradiated by x-rays. A photomultiplier can be used to amplify and detect the weak light output as shown in Fig. 2.8. X-ray photons

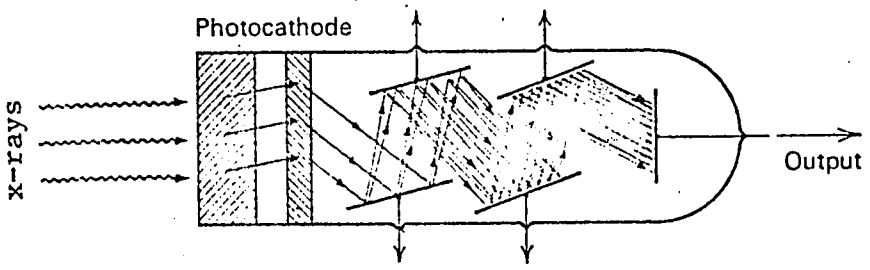

Fig. 2.8 The Scintillator Photomultiplier Detector

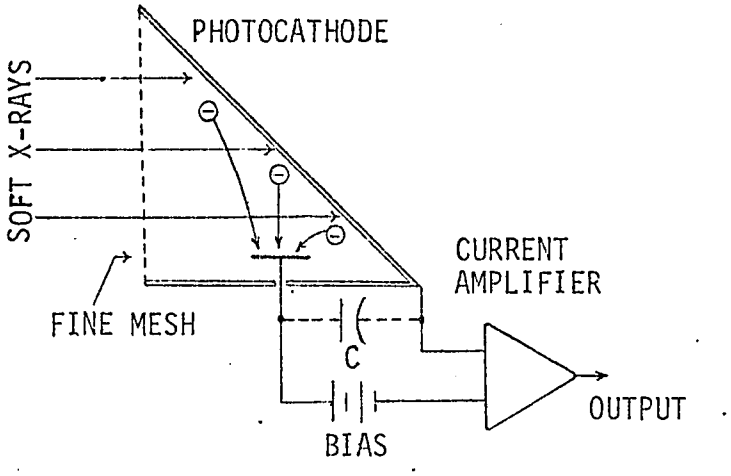

Fig. 2.9 The Principle of the Photoelectric Effect Soft X-ray Detector

striking the scintillator, produce output pulses whose height is related to the photon energy. For energies of several keV and above, conventional materials such as Sodium Iodide and plastic scintillators show good detection efficiency. For energies below 1 keV, the background noise becomes objectionably high[34]. $CaWO_4$:Pb has been successfully tried as a soft x-ray scintillator[37]. Very little is known about the detection sensitivities of other materials at low energies.

One serious disadvantage of the scintillator type detector is its non-compatibility with ultrahigh vacuum. These materials not only have a high outgassing rate, but they are generally not bakeable without serious loss of performance. If a suitable scintillating material can be found, it would offer considerable flexibility in the design of a large area total x-ray detector. By the use of a light pipe and a cooled photomultiplier, high efficiencies of detection can be achieved.

2.4.4 The Photoelectric Effect Detector

When x-rays fall on certain surfaces, photoelectrons are liberated. Measuring this photoelectron yield provides an excellent means of detecting soft x-rays. The absence of any intervening windows or films, almost entirely eliminates the low energy limit imposed on other types of detectors. The materials used are ultra-high vacuum compatible and there are no special problems in making a detector of large area.

Fig. 2.9 shows a simple way of collecting the photo-electrons and detecting them. The simple electrode collector can be

used when there is enough electron current ($\approx 10^{-12}$A), which can be measured by an electrometer type amplifier. Depending on the geometry and spacing, a positive bias of 30 to 100 volts at the electrode with respect to the cathode will ensure that most of the emitted photoelectrons are collected. The capacitance between the collector and photocathode is a limiting factor that decides the speed of response of the system. The collector area should be made small to minimize this capacitance, while maintaining sufficient cross section to intercept the photoelectrons.

When the current level is smaller than the limit of detectability of an electrometer, some form of multiplier will be needed to achieve the necessary gain with acceptable signal to noise ratio. A conventional electron multiplier can be used as a windowless photon detector by making the first dynode the photocathode (Fig. 2.10a). The photoelectrons liberated are accelerated on to the second dynode surface having a high secondary yield of 3 or more. Each electron is further multiplied and the process continues through a large number of stages. The number of dynodes generally used is in the range 10 to 20 and the overall gain achieved is over 10^6. The accelerating voltage between adjacent dynodes is supplied from a stabilized high voltage source and a metal film resistor chain, which is built as part of the multiplier structure itself. In this way, a large number of separate feedthroughs are avoided. Because of its all metallic construction, such a multiplier is bakeable and is readily compatible with ultrahigh vacuum. Activated Beryllium Copper is the most common dynode material, which exhibits stable gain even after repeated exposure to atmosphere.

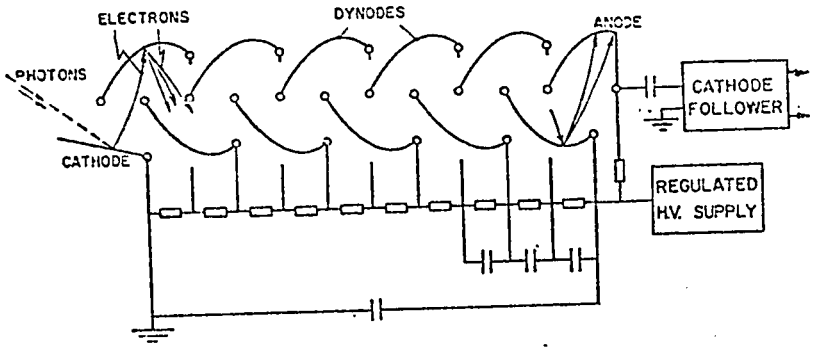

(a) Multiple Dynode

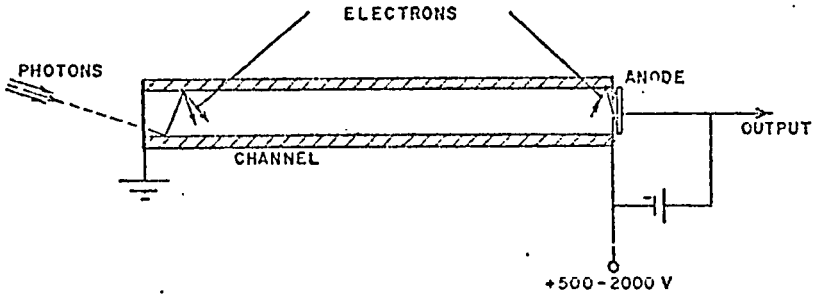

(b) Continuous Channel

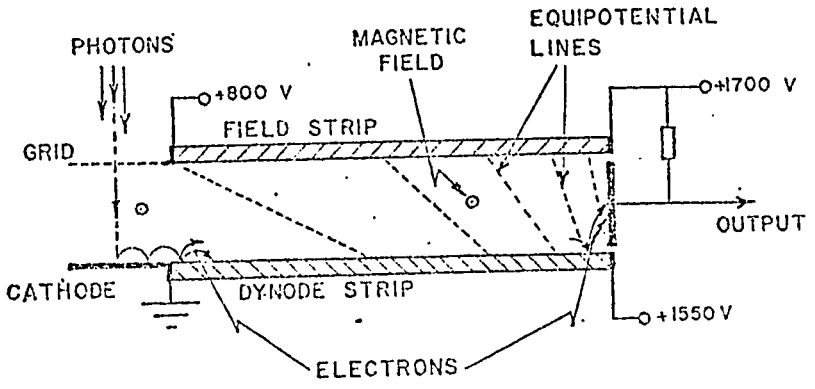

(c) Magnetic

Fig. 2.10 Types of Electron Multiplier Configurations to collect Photoelectrons

The maximum usable gain in a multiplier is limited by the background noise which consists mainly of thermionic emission from the dynodes and microdischarges at the insulators. At vacuums better than 10^{-7} torr, the noise due to residual ions is negligible[27]. Cooling the multiplier by external means will reduce the thermionic noise considerably, but it is seldom feasible because of its large size and the location inside vacuum. One way in which the background effects can be considerably minimized is by pulse height discrimination. The smaller pulses are rejected and the accepted ones are counted rather than averaged.

The channel multiplier (Fig. 2.10b) is an improved version of the electron multiplier. It consists of a set of parallel plates or a high resistivity tube, whose interior surface is coated with an active material of high secondary yield. A continuous potential gradient is maintained along the length of the multiplier, by applying a potential difference of a few thousand volts between the ends. The photons striking the entrance region liberate secondary electrons, which are accelerated towards the walls. Secondary multiplication occurs in succession along the channel, until in the end, the greatly increased number of electrons are collected by the anode. The number of stages of multiplication is not a definite quantity as in the case of the electron multiplier. It depends mainly on the physical dimensions. An overall gain of 10^5 is easily achieved in a channel only a few inches long.

In performance, the channel multiplier is very similar to the conventional electron multiplier. The smaller physical size is

the most significant improvement. Channels of only millimetres in diameter are available, which are also flexible to a certain extent, and this adds considerable versatility in actual use. An external photocathode can be used if need be, to achieve the desirable photon sensitivity. Because of the small size, several channels can be bunched together for efficient collection of electrons from large area photocathodes.

The resistance strip magnetic multiplier (Fig. 2.10c) makes use of the cycloidal motion of electrons in a crossed electric and magnetic field. The dynode strip is made of a semiconducting material or activated high resistance coating as in the channel multiplier. The field strip is merely a high resistance film, which forms the parallel electrode for the production of the electric field normal to the dynode strip. The crossed magnetic field is obtained from a permanent magnet suitably mounted. Photoelectrons released from the cathode fall on the entrance side of the dynode strip. The resultant secondaries travel in a cycloid path and strike the surface again, producing further secondaries. The cycloidal jumps are repeated along the length of the strip and finally, the electrons are collected by the anode. The magnetic multiplier has characteristics similar to those of the channel type.

Another way in which photoelectrons can be detected is by a scintillator-photomultiplier combination[38,39], as shown in Fig. 2.11. The electrons are accelerated on to a scintillator whose metallized surface is maintained at a high positive potential of 10 to 20 kV. The accelerated electrons striking the scintillator produce pulses

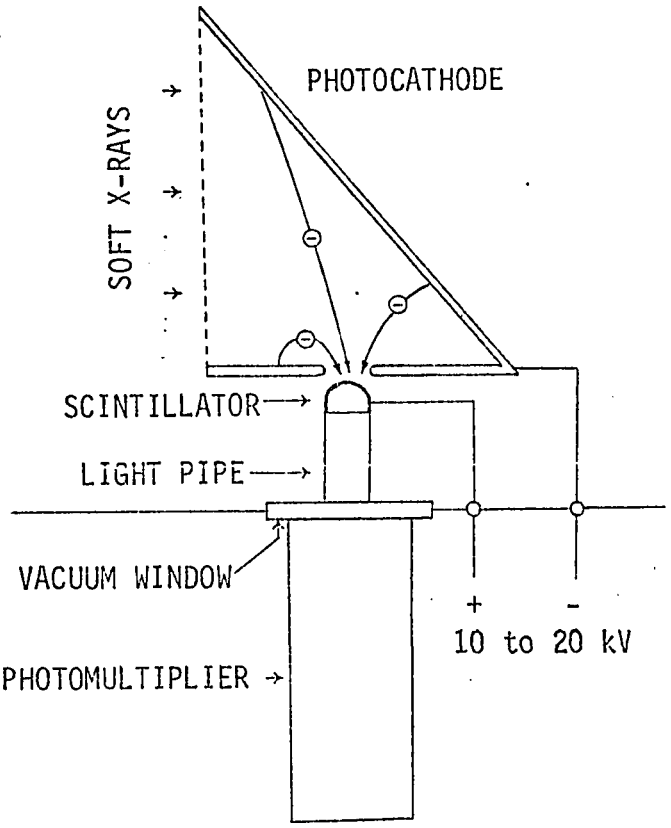

Fig. 2.11 The Photoelectric Effect Detector with Accelerated Electron Collector

of light, which are transmitted through the light pipe and optical vacuum window to the sealed photomultiplier situated outside the vacuum. Any type of scintillating material can be used for converting the electron energy to light, but commercially available plastic scintillators are a good choice, as they allow easy machining and polishing and can stand repeated exposure to atmosphere without loss of performance.

The greatest advantage of this type of detector is the extreme flexibility in its mechanical design. The scintillator can be made into a variety of shapes and sizes so as to collect a large fraction of photoelectrons. The transmission efficiency of light pipes is also quite high. The accelerating potential applied to the scintillator surface serves the dual purpose of collecting the low energy electrons that barely leave the photocathode and then imparting several keV of energy before being detected. It is in fact, an amplification process that introduces very little noise and it more than compensates for the scintillator conversion efficiency and the loss in transmission of light. The scintillator is made opaque to external light by evaporating a few thousand Angstrom layer of Aluminum, which has good transparency to high energy electrons. The conductive coating also serves as the high voltage electrode. Since a sealed photomultiplier is used, consistent good performance is assured at all times without the danger of exposure to air. Being outside the vacuum, there is no difficulty in cooling the multiplier to liquid Nitrogen temperatures, so that the background noise is greatly minimized. Using specially selected low noise tubes,

and discriminated pulse counting techniques, detection levels as low as a few tens of electrons per second can be achieved.

In common with the x-ray scintillator detector (Sec. 2.4.3), there is a problem with the incompatibility of scintillator materials with ultrahigh vacuum systems. All the commonly used scintillating materials like Sodium Iodide and plastic scintillators are non-bakeable and have high outgassing rates. However, it should be possible to find a scintillating material which can stand baking to a few hundred degrees Centigrade. For instance, quartz can be treated with Zinc oxide powder at high temperature to yield a scintillating layer on the surface. Another possibility is the deposition of a thin film of scintillating material by vacuum evaporation[40]. It is also possible to replace the scintillator and photomultiplier altogether by surface barrier electron detectors. Their smaller size is the main advantage; but additional problems arise in cooling the detector and input amplifier, which will have to be located in vacuum.

The main source of noise in the accelerated photoelectron detector is the corona discharge induced by the high electric fields. By providing proper spacings between electrodes and smoothly rounding off all corners, the electric field can be kept below the point of causing objectionable corona noise. For vacuums better than 10^{-5} torr, the noise due to residual ions has been found to be negligible[39].

2.4.5 Photoelectron Yields

The overall sensitivity of the photoelectric effect detector depends largely on the electron yield per unit quantum of radiation

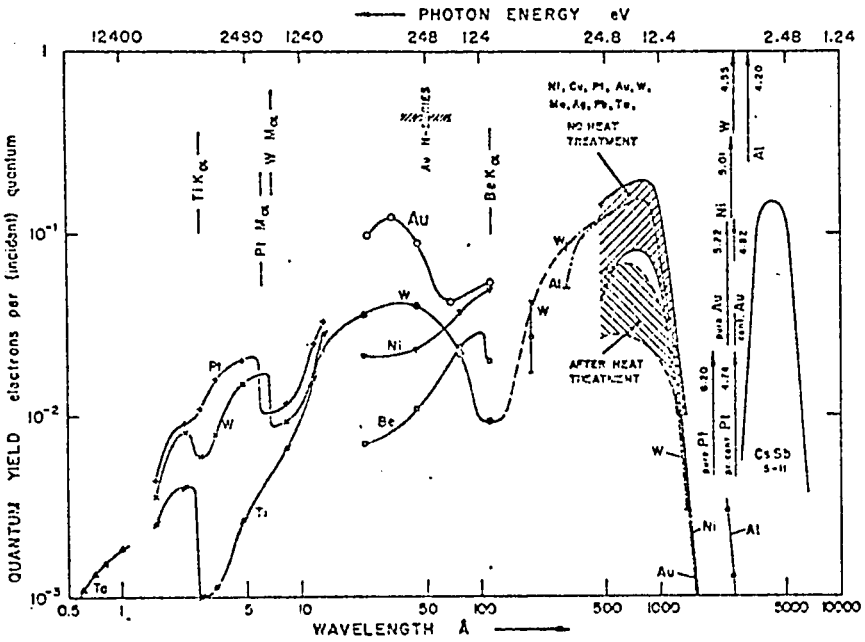

Fig. 2.12 The Variation of Photoelectron Yield with Photon Energy for different metallic surfaces

Values of Photoelectric Yields of Various Cathodes (%)

Photocathode material	Wavelength of characteristic line (Å)			
	O_K (23.6)	C_K (44)	B_K (67)	Be_K (113)
Be	0.7	1.1	2.35	2
Ni	2.1	2.3	3.7	4.9
W	3.6	4.0	2.2	0.94
LiF	—	6.0	17.0	61.0
NaF	3.2	12.5	26.0	85.0
CaF_2	15.9	7.1	14.2	25.0
SrF_2	22.0	31.0	27.0	24.0
NaCl	13.5	19.5	13.5	27.0

Table 2.1

falling on the cathode. All clean metal surfaces exhibit a certain degree of yield in the soft x-ray region. As a rule, the yield does not strongly depend on the work function of the surface, very much unlike secondary electron yield. This is because x-rays penetrate deeper into the material than electrons of the same energy. Most of the photoelectrons are produced beneath the surface layer and only a small fraction with sufficient energy manage to escape. Several investigators have studied the photoelectron yield in the soft x-ray region from various surfaces, metallic and otherwise. Fig. 2.12 shows a summary of results obtained by different authors[39]. It can be noticed that the yields from metals are small, generally lying between 1% and 10% in the photon energy range 0 to 1000 eV. The variation of yield with energy *does not* exhibit sharp discontinuities at the characteristic absorption edges of the cathode material, although gradual changes occur. This characteristic makes the photoelectric effect detector feasible for appearance potential spectroscopy, despite its poor quantum yield. Much higher yields have been observed from thin layers of certain salts deposited by vacuum evaporation on metal substrates[41,42]. Table 2.1 shows some of the results. The electron yield is also a function of the angle of incidence to the cathode, approximately secant in nature[43,44]. This implies that a higher detection sensitivity can be achieved by tilting the photocathode so that the radiation strikes at a glancing angle.

2.5 Appearance Potential Analysis

The appearance potential method of analysis can be considered as a modified version of absorption analysis. It is basically a

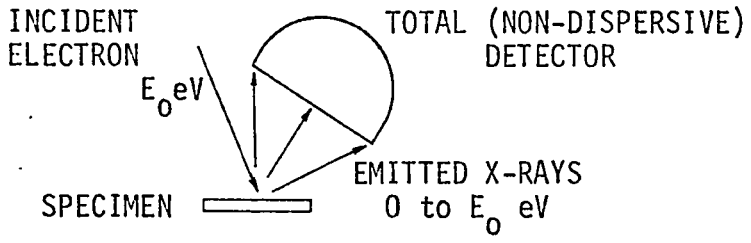

(a) Layout for Experiment

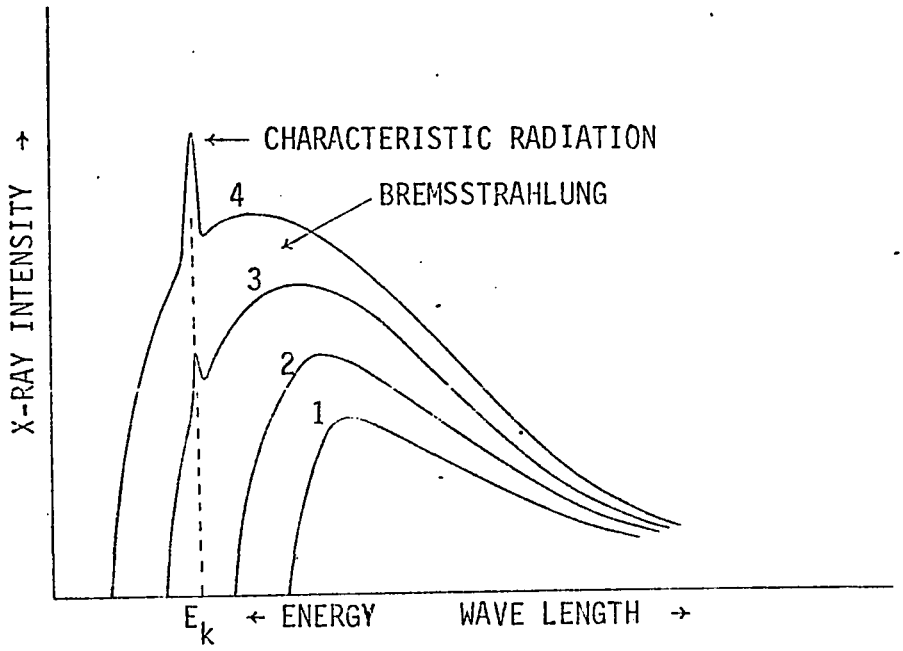

(b) Variation of X-ray Energy Distribution with Incident Energy

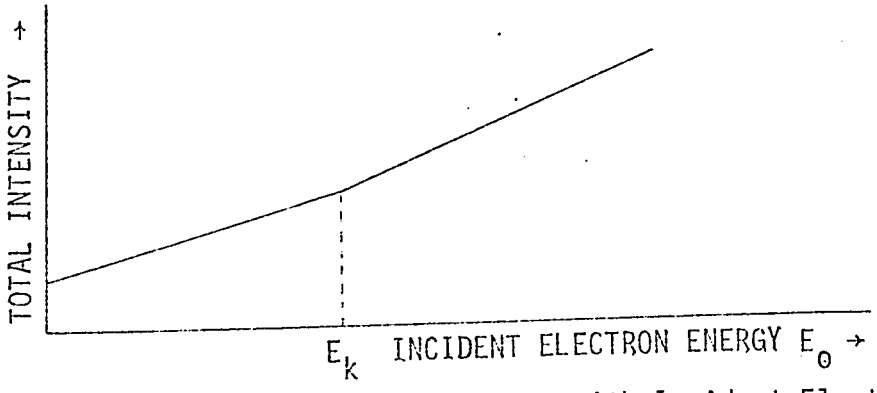

(c) Variation of Total Intensity with Incident Electron Energy

Fig. 2.13 The Principle of Appearance Potential Analysis

nondispersive technique which makes use of a simple total radiation detector. In all the conventional methods of x-ray analysis, the incident energy is fixed during analysis and does not have to be known precisely, but the emitted radiation is subjected to accurate energy analysis. In the appearance potential analysis, the incident energy is continuously varied and precisely measured at all times. The emitted x-rays are not energy analyzed, but changes in their total intensity are monitored.

Fig. 2.13 illustrates the basic principle of appearance potential analysis. The sample is bombarded by electrons from a source, accelerated through a continuously variable potential of E_o. A large solid angle detector facing the specimen and located close to it collects a significant fraction of the total x-radiation of all energies emitted. Fig. 2.13b shows the x-ray energy distribution at different values of incident electron energy for a hypothetical element having an absorption edge (or appearance potential) at E_k. Curves 1 and 2 are for the case when $E_o < E_k$, with only the bremsstrahlung present and no characteristic radiation. Curves 3 and 4 show small spikes occuring at the same value of energy E_k, which correspond to the characteristic radiation emitted, as $E_o > E_k$. The higher the value of E_o, the larger the spike. The type of detector used in appearance potential analysis does not see this energy distribution of x-rays. Instead, it measures the total x-rays falling on the detector, which is proportional to the area under the distribution curve for each value of the incident electron energy. In Fig. 2.13c, this is plotted against electron energy. Below E_k, the

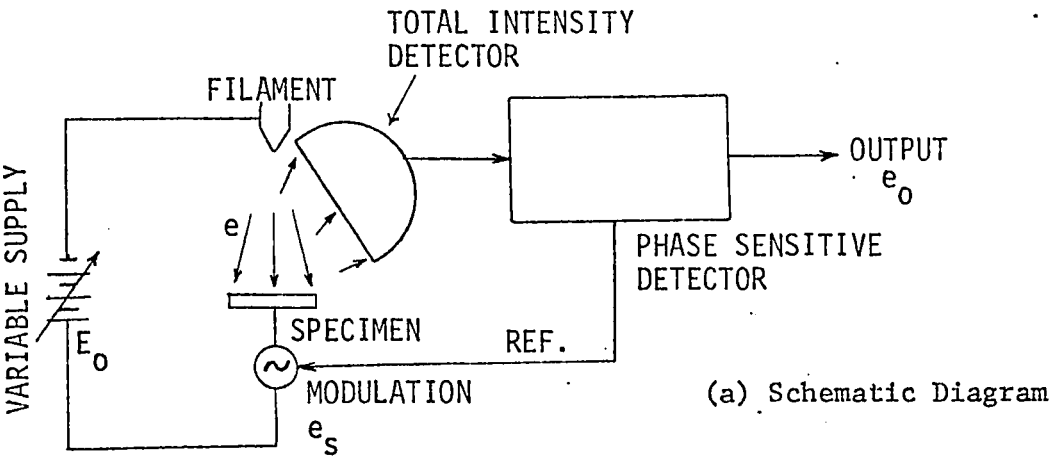

(a) Schematic Diagram

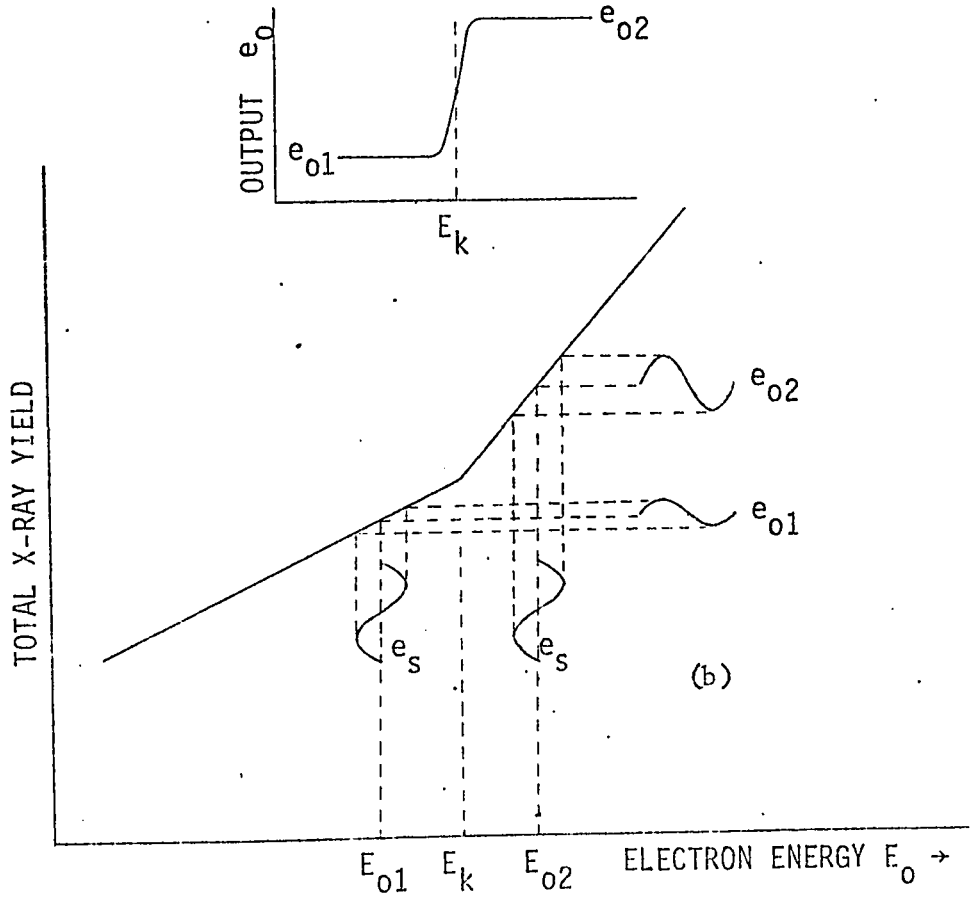

Fig. 2.14 Electronic Differentiation of the Total Yield Curve

only contribution is due to the bremsstrahlung which gives rise to a monotonically increasing but smooth line. Above E_k, there is an additional contribution from the characteristic radiation, which itself is monotonically increasing with incident energy. The net result is a sharp change in slope occurring at E_k.

In practice, the change in slope explained above is extremely small and is barely detectable in the total x-ray curve. This is because the characteristic x-ray production, which is a power function of the over voltage $(E_o - E_k)$, has a very low constant of proportionality[31]. In order to be able to discern the change in slope, the large background slope must be suppressed by some means. This can be achieved by electronic differentiation of the total signal. Fig. 2.14 explains how this is done by introducing a small modulation to the incident electron energy. At any value of E_o, the total x-ray output seen by the detector will consist of a large dc level and an ac component at the modulating frequency. As long as the modulation is small and the incident energy is scanned slowly, then, to a first approximation, the amplitude of the fundamental component is proportional to the slope of the total yield curve[45]. A phase sensitive detector at the output is an ideal way of extracting the ac component which contains the needed information. Electronically, the phase sensitive detector is equivalent to a selective filter of very high Q. The insert in Fig. 2.14b shows how the change in slope appears as a greatly exaggerated step with the large background level completely suppressed.

Appearance potential spectroscopy has several unique

features. The most important of all is the simplicity of the apparatus. The use of a total x-ray detector obviates the need for costly and elaborate energy dispersive units such as crystals and pulse height analyzers. On the contrary, the detecting electronics required in appearance potential spectroscopy consist of basic units which are generally available in laboratories as standard equipment. By using only low energy electrons (0 to 1000 eV), and a windowless soft x-ray detector, it is theoretically possible to detect all elements. This is so because all of the elements have at least one absorption edge in this energy range, as illustrated in Fig. 2.15 and the energy level tabulations in the Appendix. In contrast, all conventional forms of x-ray analysis use tens of kilo volts to accelerate the electrons, which gives rise to high voltage problems in equipment design and operation.

Because of the low energy of the probing electrons, the depth of sampling in appearance potential spectroscopy is less than about 100 Å. It is therefore, basically a surface analysis tool, which provides information complementary to that of Auger electron spectroscopy[46].

One important feature of appearance potential spectroscopy is that it gives a direct and precise measurement of electron binding energies in an atom. This will be a valuable facility in the study of chemical shifts evident in crystalline solids and compounds. Such measurements could shed considerable light on the various valence states of an element, which are difficult to observe by other means.

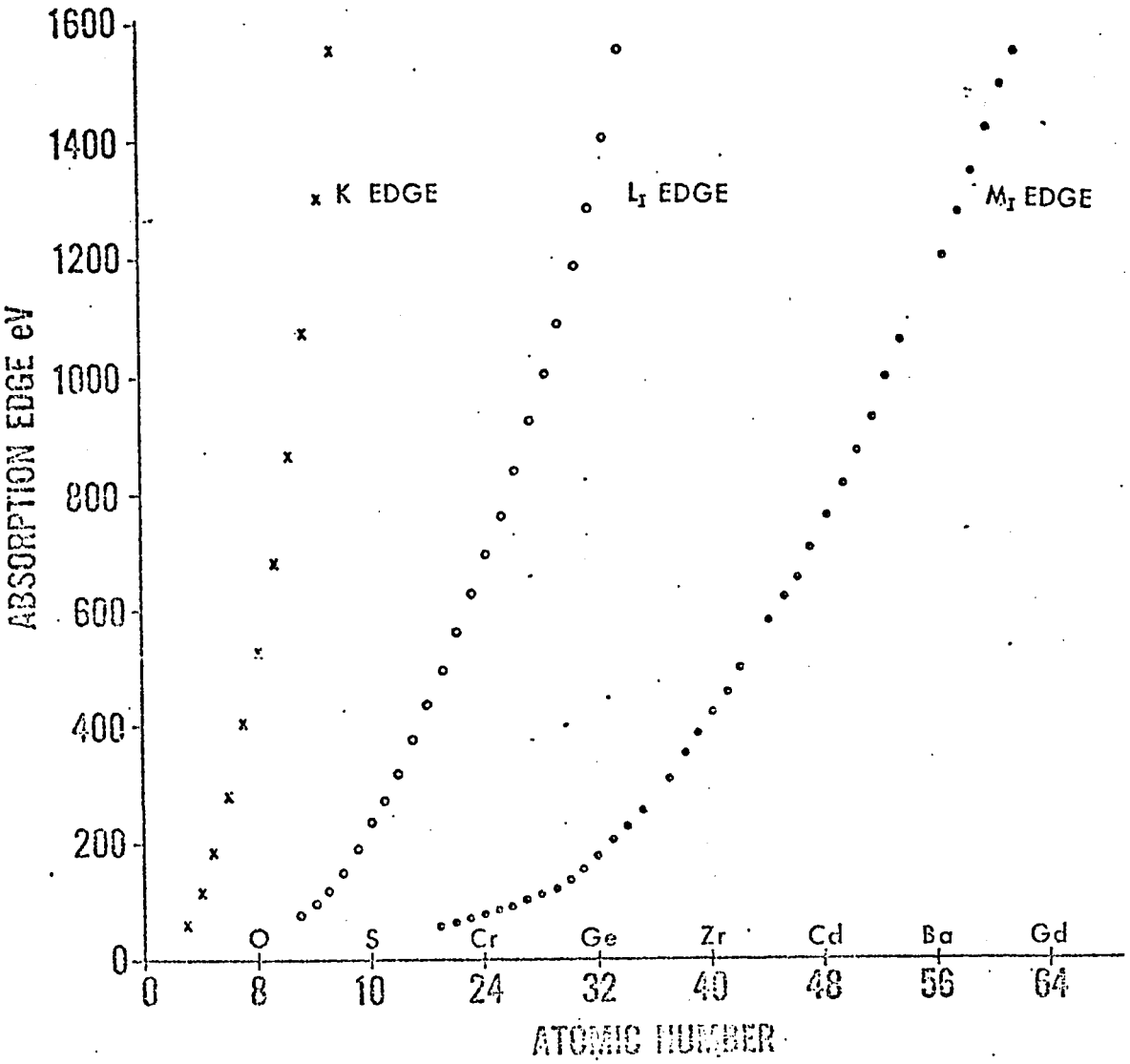

Fig. 2.15 The Variation of Absorption Edge Energy with Atomic Number

At the present time, the detection sensitivity of appearance potential spectroscopy is very modest compared with that of a conventional x-ray spectrometer. Electron currents in the milliampere range are needed in appearance potential spectroscopy, whereas a microampere of probe current will provide a good signal in conventional method. A focused beam has not been used in appearance potential spectroscopy, mainly because of the high current required. The detection sensitivity of appearance potential spectroscopy to different elements varies from good to poor, depending among other things, on their location on the periodic table. Some elements like Tungsten have failed to register any signal at all. Another serious problem is the handling of non-conducting materials, as it is almost impossible to pass currents in the milliampere range through the bulk of such specimens. Since the surface itself is probed, it is not possible to evaporate even a very thin conducting layer to overcome this limitation. There is also no control over the depth of sampling, which varies from element to element depending on the position of the absorption edge used for identification. Also, a clean, ultrahigh vacuum environment ($\simeq 10^{-8}$ torr or better) is essential to avoid surface contamination during appearance potential spectroscopic measurements.

CHAPTER 3. THEORETICAL ASPECTS OF APPEARANCE POTENTIAL SPECTROSCOPY.

In chapter 2, the x-ray excitation curve was shown to consist of segments of straight lines of different slopes, with break points corresponding to appearance potentials. The appearance potential spectrum obtained by differentiating the excitation curve exhibited steps at the critical values. However, most elements exhibit pronounced and complex structure in their appearance potential spectra, extending over several electron volts on the higher energy side of the known values of absorption edges, but little work has been reported on the theory of the phenomenon. This chapter summarizes the relation between the above effects and electronic transitions in atoms. No rigorous theory describing the process has been worked out yet, but the present theory, though qualitative, explains the main features observed in the appearance potential spectra.

Absorption spectra of elements in the higher energy ranges have been extensively reported in the literature, but very few results are available on the low energy absorption structure. Although the mode of primary excitation is different, the absorption spectrum and the appearance potential spectrum of an element resemble each other. The absorption spectra of light elements show considerable fine structure as do the appearance potential spectra. Some of the low energy spectra reported in the past years are reviewed in this chapter, in order to strike a comparison with the results of appearance potential spectroscopy.

The resolution with which the appearance potential spectrum can be obtained is limited by many of the experimental parameters. In addition to this, correction factors are necessary to establish absolute values of the appearance potentials and to compare them with the absorption edges, which are known from spectroscopic measurements. These effects also are discussed in this chapter.

Another quantity considered here is the quantum efficiency of electron excited x-ray generation. It is indicated that, in the soft x-ray region, the empirical relations normally used for high energy calculations, do not yield results that agree with experiment.

3.1 The Absorption Process

As a result of quantum mechanical considerations, it is known that electrons in an atom are distributed in discrete energy levels identified by a set of quantum numbers, n, l and j. For the sake of convenience in x-ray spectroscopy, these levels are called K, L, M etc., corresponding to n = 1, 2, 3 etc., in the order of increasing energy. Fig. 3.1 gives a graphical representation of these levels[47]. X-ray emission can take place when an electron makes an allowed jump from a higher level to a vacant position in one of the lower levels, the wavelength being given by the relation,

$$\frac{c}{\lambda} = \nu = \frac{E_1 - E_2}{h} \qquad \ldots (3.1)$$

where E_1 and E_2 are the energies of the two levels between which the transition takes place. In practical units, this equation reduces to

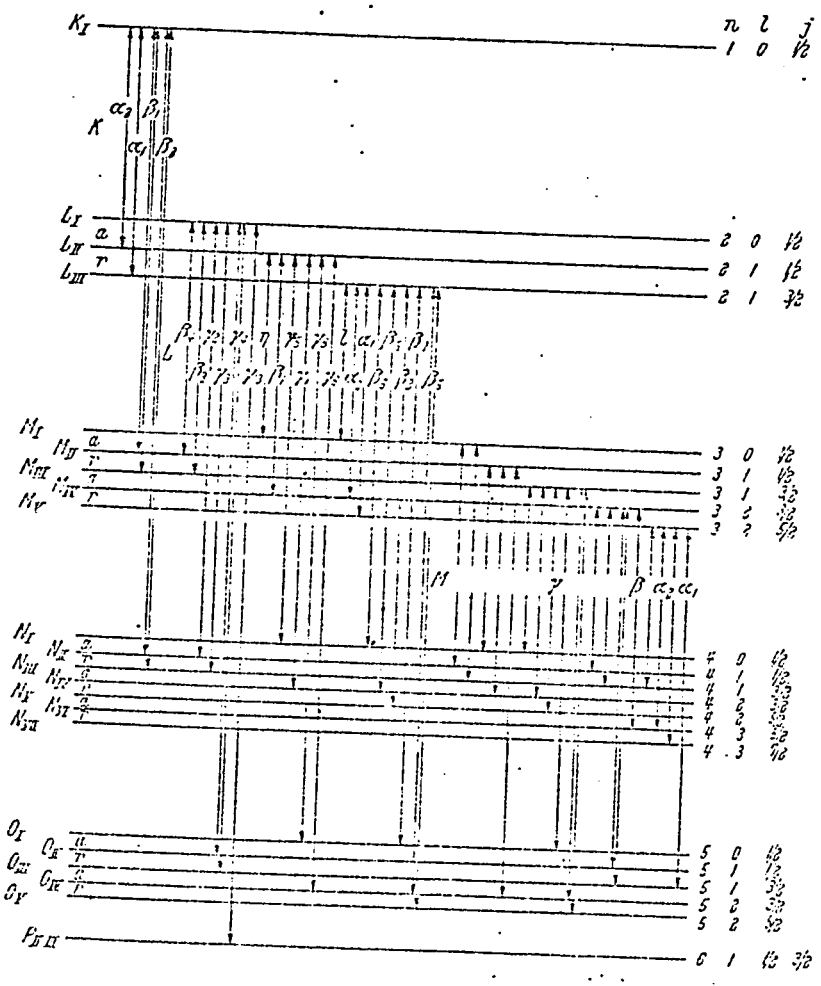

Fig. 3.1 Schematic Representation of Energy Levels in an Atom and the Designations of Emission Lines

$$\lambda \text{ in } \mathring{A} = \frac{12{,}400}{\text{Energy in electron volts}} \qquad \ldots (3.1a)$$

These jumps or transitions are governed by selection rules. All the allowed transitions and the designations of the corresponding emission lines are shown in the figure. In the normal state of the atom, the inner shells are filled by electrons, without leaving any vacancies. The first step in the x-ray generation process is the creation of a vacancy in one of the inner levels. This can happen when an external particle or quantum of sufficient energy interacts with the atom. An electron so liberated can go only to one of the outer empty levels. One necessary condition to be satisfied for this to happen is that the energy of the incident particle or quantum be more than the energy separation between the initial, filled and the final, empty levels. The absorption process results from the transition of electrons from an inner level to an outer, more energetic but empty one, whereas the emission process results from the refilling of an inner vacancy by one of the outer electrons. In an isolated atom, the available empty levels may either be the optical levels above the outermost filled level, or the continuum corresponding to the complete removal of the electron from the atom (Fig. 3.2). Absorption is denoted by upward arrows and emission by downward arrows. In the case of solids, the outermost or valence electrons are shared by neighbouring atoms and as a result, considerable change in the energy level structure occurs. Fig 3.3 shows the modified diagram for solid Magnesium. The main feature is the creation of a valence energy band, which under normal conditions is partly filled by valence electrons. In addition to this, the originally sharp inner

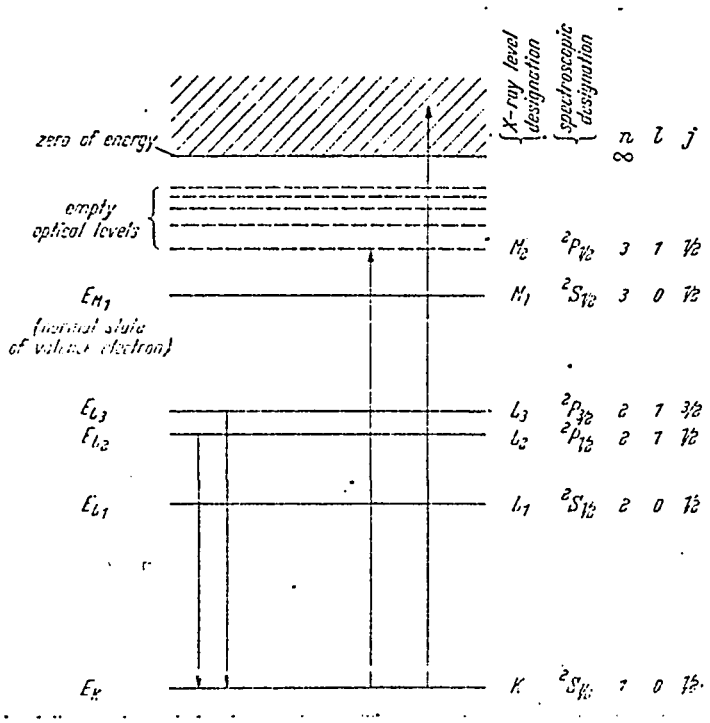

Fig. 3.2 Energy Levels in a Typical Atom (Z=11)

levels like K and L are broadened into bands of small but finite widths. Typical transitions are shown by arrows, upward for absorption and downward for emission.

The initial condition for an absorption transition is the undisturbed atom, with the inner shells and the lower portion of the valence band filled. When the incident energy is greater than the separation between a filled shell and the bottom of the empty states in the valence band, an absorption transition can occur. The process of absorption of radiation by the atoms in a solid has been mathematically formulated by Dirac[48] and quoted by Tamboulian[47]. In this section, the main steps in the development of the equations are given, without going into the details of formulation. It is by no means intended as a complete quantum mechanical presentation of the absorption process. However, the final form in which the equation is presented shows the key variables in the process.

Let $I_o(\nu)d\nu$ be the intensity of incident energy per unit area per unit time, where ν is the frequency of radiation. Absorption of a quantum of energy $h\nu$ results in the transition of the atom from an initial state denoted by ψ_o, to the final state denoted by ψ_k. The energy $\alpha(\nu)$ absorbed by the atom in a unit frequency range per unit time is the product of the incident intensity in that frequency range and the probability of transition from the state ψ_o to the state ψ_k. This can be expressed as[47]

$$\alpha(\nu) = \frac{e^2 h}{2\pi m^2 c\nu} \left| \int \psi_k^* \frac{\partial}{\partial x} \psi_o d\tau \right|^2 I_o(\nu) \qquad \ldots (3.2)$$

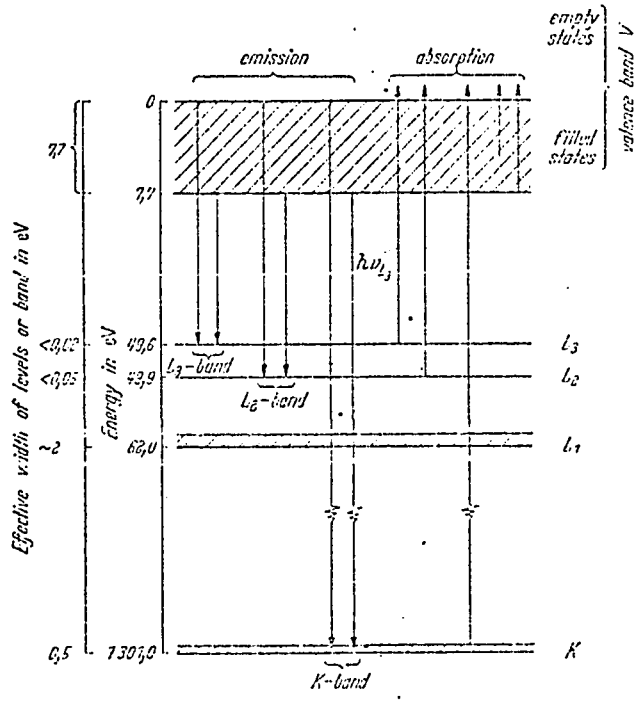

Fig. 3.3 Atomic Levels in Solid Magnesium (Z=12)

where $d\tau$ is an elemental volume.

The number of states per atom, in the energy range E and E+dE is given by

$$N(E)\, dE = \frac{\Omega}{4\pi^3} \int_S \frac{ds}{|\text{grad}E|}\, dE \qquad \ldots (3.3)$$

where Ω is the volume of the unit cell containing one atom and the integration is carried out over the surface S on which the energy E has a constant value. The gradient is taken with respect to the wave vector k.

If $h\nu_o$ is the energy separation between the inner level from which the transition takes place and the lowest unoccupied level in the valence band, then E, the excess energy of the electron above this level is given by

$$E = h\nu - h\nu_o$$

where $h\nu$ is the incident energy.

Associated with every value of E, there is a momentum vector having components p_x, p_y, p_z. The energy $A(\nu)$, absorbed by an atom as a result of electronic transitions from the filled inner level to empty levels in the valence band, is obtained by averaging the energy over all possible values of the three components of electron momentum. It can be shown that

$$A(\nu)\, d\nu = \frac{e^2\hbar^2\Omega}{6\pi^2 m^2 c\nu} I_o(\nu)\, d\nu \int_S \frac{|M_{ko}|^2}{|\text{grad}E|}\, ds \qquad \ldots (3.4)$$

where $|M_{ko}|^2$ replaces the sum

$$\sum_i \left| \int \psi_k^* \frac{\partial}{\partial x_i} \psi_o \, d\tau \right|^2$$

The absorption coefficient is defined by

$$\mu(\nu) = n \frac{A(\nu)\, d\nu}{I_o(\nu)\, d\nu} = \frac{n e^2 \hbar^2 \Omega}{6\pi^2 m^2 c\nu} \int_s \frac{|M_{ko}|^2}{|\text{grad}E|} \, ds \qquad \ldots (3.5)$$

where n is the number of atoms per unit volume. The integral of the form

$$\int \frac{|M_{ko}|^2}{|\text{grad}E|} \, ds$$

is a joint function of the energy gradient and the transition probability. In practice, the elements of the transition matrix cannot be evaluated. Assuming that $|M_{ko}|^2$ has an average, constant value on the surface of energy E, it can be written in terms of the density distribution N(E) from eq. 3.3 as

$$\mu \propto \frac{1}{\nu} |M_{ko}|^2 N(E) \qquad \ldots (3.5a)$$

It can be seen from the above equations that variations in the density of empty states in the valence band and variations of the electronic transition probability, will contribute to the structure observed in the absorption spectrum of an element. In general, neither of the two quantities is known, and the absorption spectrum can only qualitatively be related to the valence state of the atom.

3.2 The Appearance Potential Spectrum

In appearance potential spectroscopy, the primary excitation is achieved by an incident electron of energy E. As a result

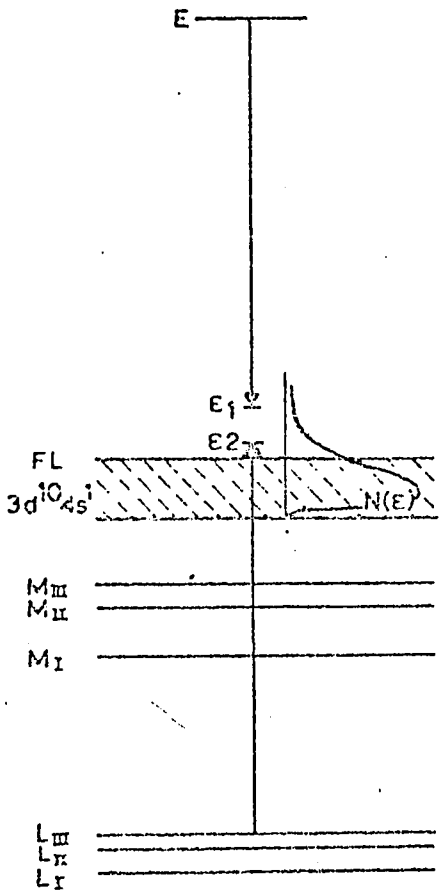

Fig. 3.4 Electronic Excitation of a Cu atom

of the interaction between the electron and the atom, a hole is created at an inner level E_b. Two electrons are released during the process, to the empty levels in the valence band:

1) the incident electron, and

2) the electron released from the core level

If ε_1 and ε_2 denote the energies of the two electrons referred to the fermi level (Fig. 3.4), it is required for energy balance that

$$E - E_b = \varepsilon_1 + \varepsilon_2 \qquad \ldots (3.6)$$

The total ionization probability of the core level E_b is the sum of the probabilities of all possible transitions of the two electrons to the empty levels in the valence band, which have a density distribution $N(\varepsilon)$ as shown in the figure. The total ionization probability $P(E)$ can be expressed as[49]

$$P(E) \propto \int_0^E \phi(E' - E_b)\, f(E, E')\, dE' \qquad \ldots (3.7)$$

where $\phi(E' - E_b)$ is a distribution function pertaining to the core level, E_b. This arises because of the finite spread in the energy level, E_b. Under the assumption that the levels are single valued at E_b, this term reduces to a constant. E' is the variable of integration, and can take values up to E. The term $f(E, E')$ denotes the probability function for the process involving the two electrons, and is given by

$$f(E,E') \propto \int_0^{E-E'} p_{e1}(\varepsilon_1, E)\, N(\varepsilon_1)\, p_{e2}(\varepsilon_2, E)\, N(\varepsilon_2)\, d\varepsilon_2 \qquad \ldots (3.8)$$

where p_{e1} is the probability that the electron 1 will go to the level

ε_1, p_{e2} the probability that the electron 2 will go to the level ε_2 and f(E,E') the overall probability for both the transitions to occur.

Assuming that p_{e1} and p_{e2} are constant, it can be written

$$f(E,E') \propto \int_{o}^{E-E'} N(\varepsilon_1)\ N(\varepsilon_2)\ d\varepsilon_2 \qquad \ldots (3.8a)$$

Park and Houston[50] give a simplified version of the above equations under the assumption that the core hole has negligible energy width and a density of n_c. Also, neglecting the variation of electronic transition probabilities, they obtain

$$P(E) = n_c \int_{o}^{E} N(E')\ N(E-E')\ dE' \qquad \ldots (3.9)$$

The principal features of an appearance potential spectrum can be explained using the above equation. Fig. 3.5 shows schematically the case of a typical 3d transition element. Curve (a) gives the approximate distribution of valence band density consisting of a relatively sharp 3d band overlapping the broad free-electron like 4s band. E_f is the fermi level up to which the valence band is filled with electrons under normal circumstances. The probability function P(E), as given by the eq. 3.9 will have a form shown by curve (b). This is also the shape of isochromats[49] obtained by plotting the characteristic x-ray yield against energy. The appearance potential spectrum is obtained by differentiating the total yield curve. This is indicated by (c), which is the derivative of (b).

It may be noted that in the case of transition elements with a band structure shown in Fig. 3.5, the appearance potential

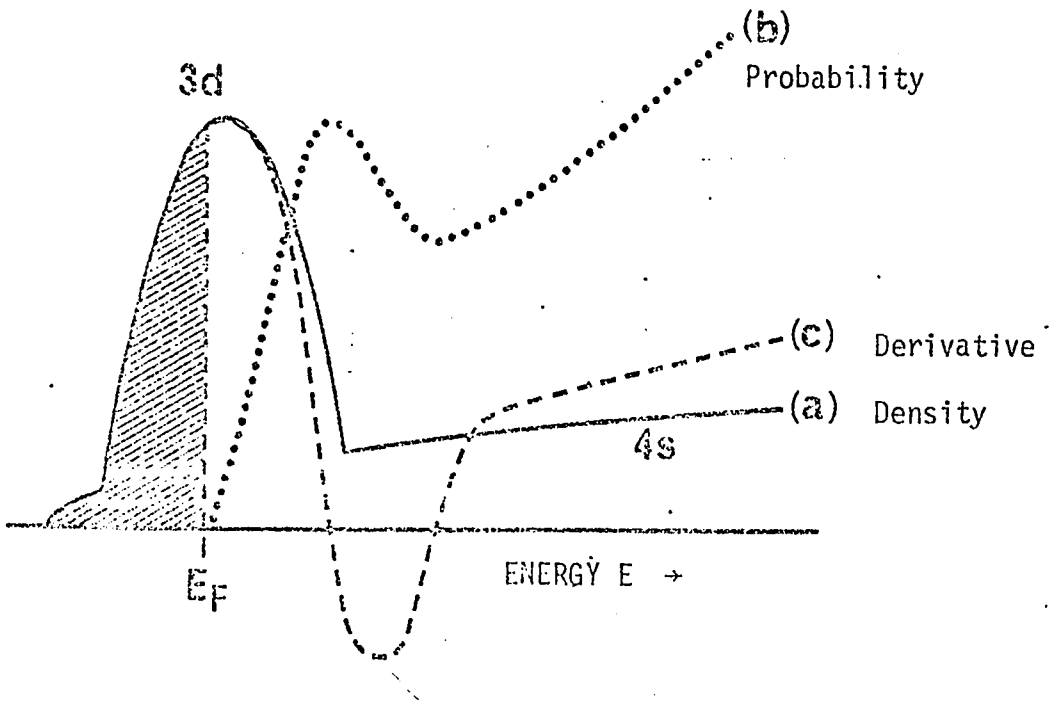

Fig. 3.5 Schematic representation of the Density of States Distribution in the valence band of a typical 3d transition element.

spectrum exhibits sharp positive and negative swings immediately above the absorption edge. For elements in the transition series, the position of the fermi level is shifted progressively to the right, with increasing atomic number, as the 3d band is filled. The appearance potential spectra of these elements exhibit similar variations above the corresponding threshold values of energy, the peaks being more or less pronounced. But for Copper, the last element in the series, the band is already full in the unexcited state, and no peaks in its appearance potential spectrum would be expected. It has been experimentally observed that Copper shows only a discontinuity at the absorption edge*. For other elements in the transition series, the presence of positive and negative peaks greatly enhances the detection sensitivity.

The assumption that the transition probabilities p_{e1} and p_{e2} in eq. 3.8, are constants, is not necessarily true in practice. Any variation of these quantities with energy, will cause additional structure in the appearance potential spectrum.

In the foregoing discussion based on the band structure, the total x-ray yield curve was considered to be analogous to the ionization probability P(E) of the atom. However, not every ionization of the inner level is followed by a radiative transition, resulting in the emission of a photon[45]. On the contrary, a hole created at low energy levels is most probably filled by a non-radiative Auger transition. Thus, what is observed in the appearance potential spectrum in the low energy ranges is only derived from a very small fraction (called the fluorescent yield) of the ionizations which

take place. If this fraction is constant, then the probability curve P(E) gives a true representation of the total photon yield. But any fluctuation of this fraction with incident energy, will contribute to the observed structure in the appearance potential spectrum.

3.3 Absorption Edge Structure

In this section, a few examples of low energy absorption spectra of light elements observed by various investigators and quoted by Tomboulian[47], are presented.

Skinner and Johnston obtained the K absorption edge of Lithium as shown in Fig. 3.6. The absorber was prepared by vacuum deposition of Lithium on a thin film. To eliminate the effect of the back-up film, measurements were made for two successive layers of different thickness on the same substrate, and the difference in absorption plotted, instead of the absolute value which is uncertain. The main absorption edge occurs around 55 eV and it agrees with the values obtained from the emission data. There is a prominent structure on the high energy side of the edge. This suggests fluctuations in the density of empty states beyond the fermi level.

The K absorption edge of Beryllium was investigated by Johnston and Tamboulian (Fig. 3.7). A thin foil of the metal was used as the absorber specimen. The spectrum shows a step at 111 eV which corresponds to the accepted value of the absorption edge. Immediately following this is a sharp peak which indicates a rapid rise in the density of empty states just above the fermi level. There is also some less prominent structure which extends over several

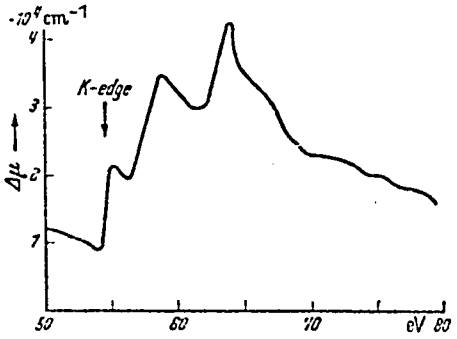

Fig. 3.6 K Absorption Edge of Lithium

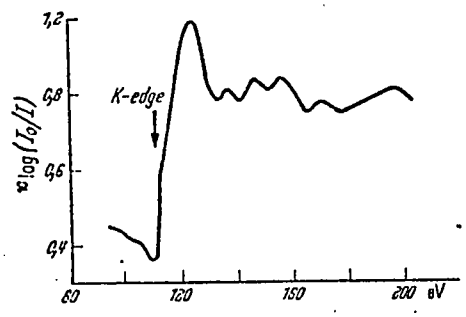

Fig. 3.7 K Absorption Edge of Beryllium

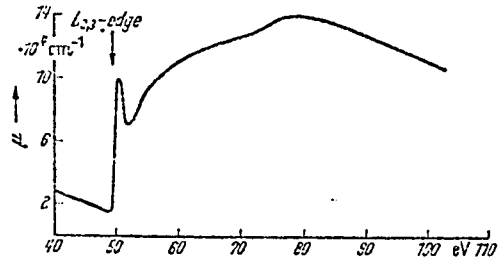

Fig. 3.9 L Absorption Edge of Magnesium

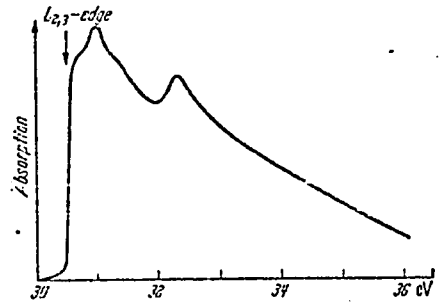

Fig. 3.8 L Absorption Edge of Sodium

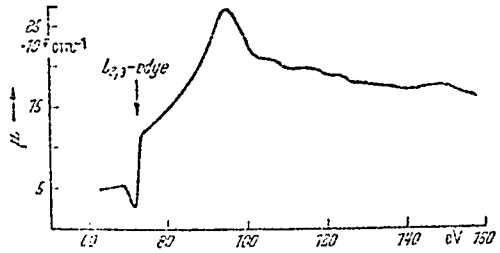

Fig. 3.10 L Absorption Edge of Aluminum

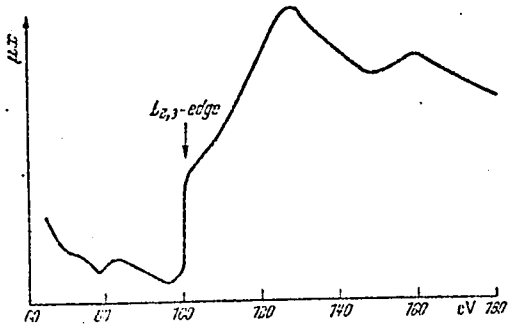

Fig. 3.11 L Absorption Edge of Silicon

volts on the high energy side.

Being a refractory material, Boron is difficult to work with. The emission spectra of Boron and Boron compounds have been published by many authors. There seems to have been no report on the absorption spectrum, probably because of the practical difficulties in forming a thin layer of the material.

Preliminary results on the absorption spectrum of Carbon were published by Chalklin and Magnusson. The absorption edge is located at 284 eV. However, there have been no reports on the detailed structure above the edge.

Fig. 3.8 shows the L absorption spectrum of Sodium obtained by O'Bryan. The $L_{2,3}$ edge is sharply displayed and it is followed by some structure.

The L absorption spectra of Magnesium published by Townsend, Aluminum by Tomboulian and Silicon by Tomboulian are shown in Fig. 3.9, 3.10 and 3.11 respectively.

All these absorption spectra exhibit discontinuities at the accepted values of the absorption edges and considerable structure on the high energy side. The structure is roughly divided into two types; one close to the edge and one at higher energies. According to the Hayasi theory[47], the former is a result of transitions to quasi-stationary final states. These states are produced as a result of electron standing wave patterns in the immediate vicinity of the atom. Using this concept, it was possible to calculate the prominent secondary structure close to the K edges of most light elements.

The fluctuations in the absorption spectrum occurring at about 100 eV or more above the edge are called Kronig structure. These are caused by the propagation of energetically released electrons through the lattice. The Kronig structure is largely dependent on the lattice structure and the direction of travel of the ejected electron. Because of the numerous possible combinations, it becomes difficult to locate these peaks.

3.4 Plasmon Effects

The collective, quantized oscillations of the free electron gas in a crystal are called plasmons[51]. The oscillations can be produced as a result of the displacement of the distribution of free electrons. This can be induced by an incident electron. Fig. 3.12 illustrates the mechanism of plasma oscillations. The shaded area represents the electron cloud and the positive charges represent the immobile atomic nuclei, in a slab of the crystal. At (b), the electron cloud is shown displaced by η from the equilibrium position. If n denotes the concentration of electrons, the surface charge induced is, $\sigma = \eta ne$, positive on the lower half and negative on the upper half. The electrical field $E = 4\pi\eta ne$ created between the two sides, moves the displaced electron cloud towards equilibrium, and this sets up oscillations about the equilibrium position. The resulting simple harmonic oscillations can be described by the equation,

$$nm \frac{d^2\eta}{dt^2} = -neE = -4\pi n^2 e^2 \eta \qquad \ldots (3.10)$$

The frequency ω_p of the oscillations is given by

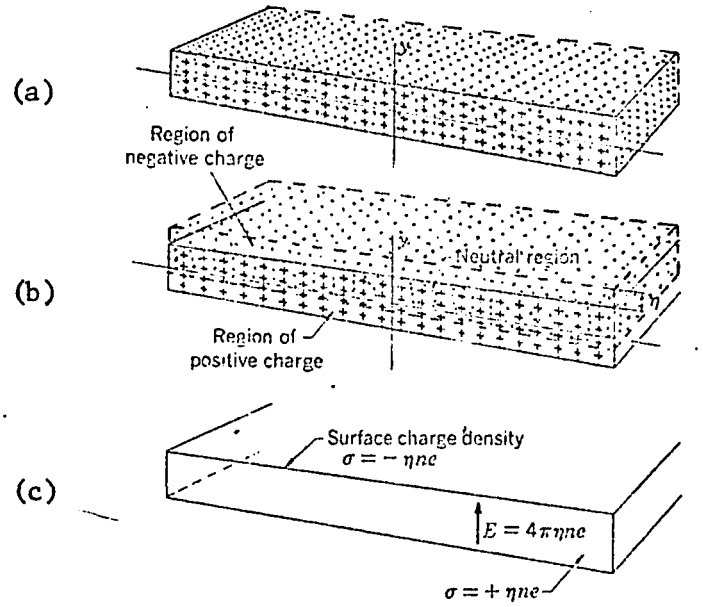

Fig. 3.12 Plasmon Oscillations in a Material

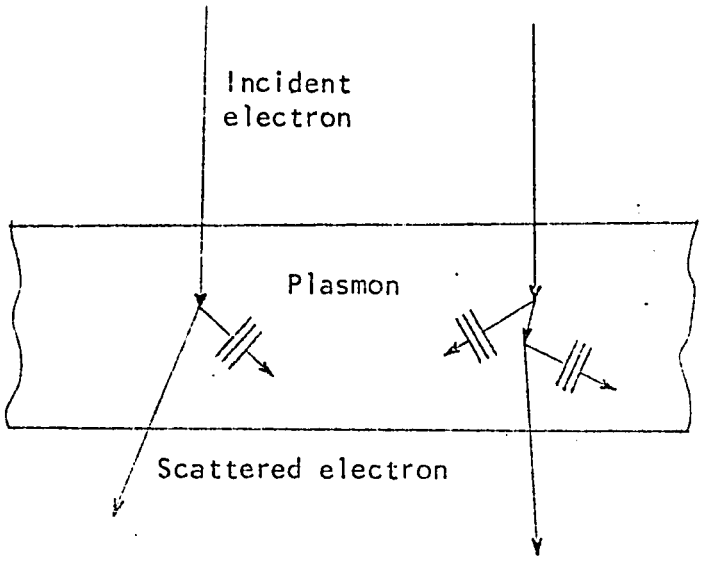

Fig. 3.13 Plasmon Excitation by Incident Electrons in a Thin Film

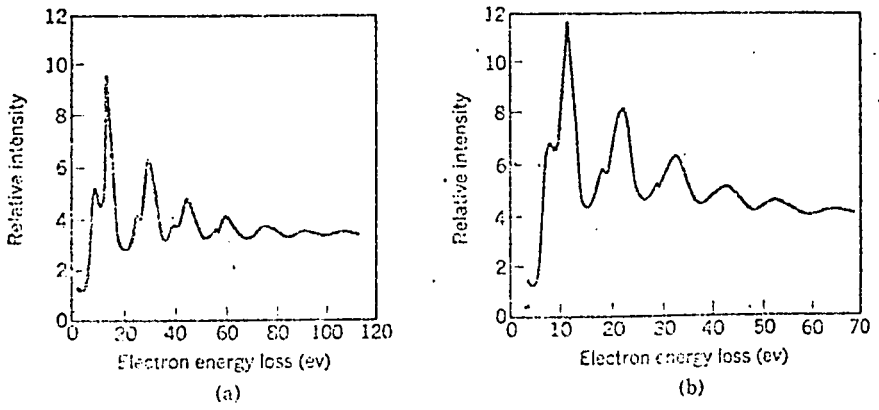

Fig. 3.14 Plasmon Energy Loss of Incident Electrons (a) Aluminum (b) Magnesium

$$\omega_p = \left(\frac{4\pi ne^2}{m} \right)^{\frac{1}{2}} \qquad \ldots (3.10)$$

Plasmons have been observed by reflecting electrons from a surface and by passing them through a thin section of many samples. As shown in fig 3.13, the incident electron is scattered after the creation of a plasmon. As a result of this process, the electron exhibits characteristic energy loss after interaction. Two such examples are shown in Fig. 3.14. The decay of plasmons can produce radiation of photons[52]. The presence of plasmons will cause secondary structure in the appearance potential spectrum of an element. This structure has been observed in the spectra of light elements such as Carbon and Boron[30]. In a recent publication, the effect of plasmons in appearance potential spectroscopy is treated from a theoretical point of view by Laramore[53].

3.5 Work Function Correction

The work function of a surface is defined as the energy in electron volts necessary to liberate an electron from the material. A contact potential difference exists between any two dissimilar materials, because of the differences in their work functions. As shown in Fig. 3.15, the value of this contact potential is equal to the difference between the work functions, when the two materials are in thermodynamic equilibrium.

For the accurate location of the structural features in appearance potential spectroscopy, the energy of the electrons striking the specimen must be precisely known. It is therefore necessary to apply a correction for the contact potential between the emitter

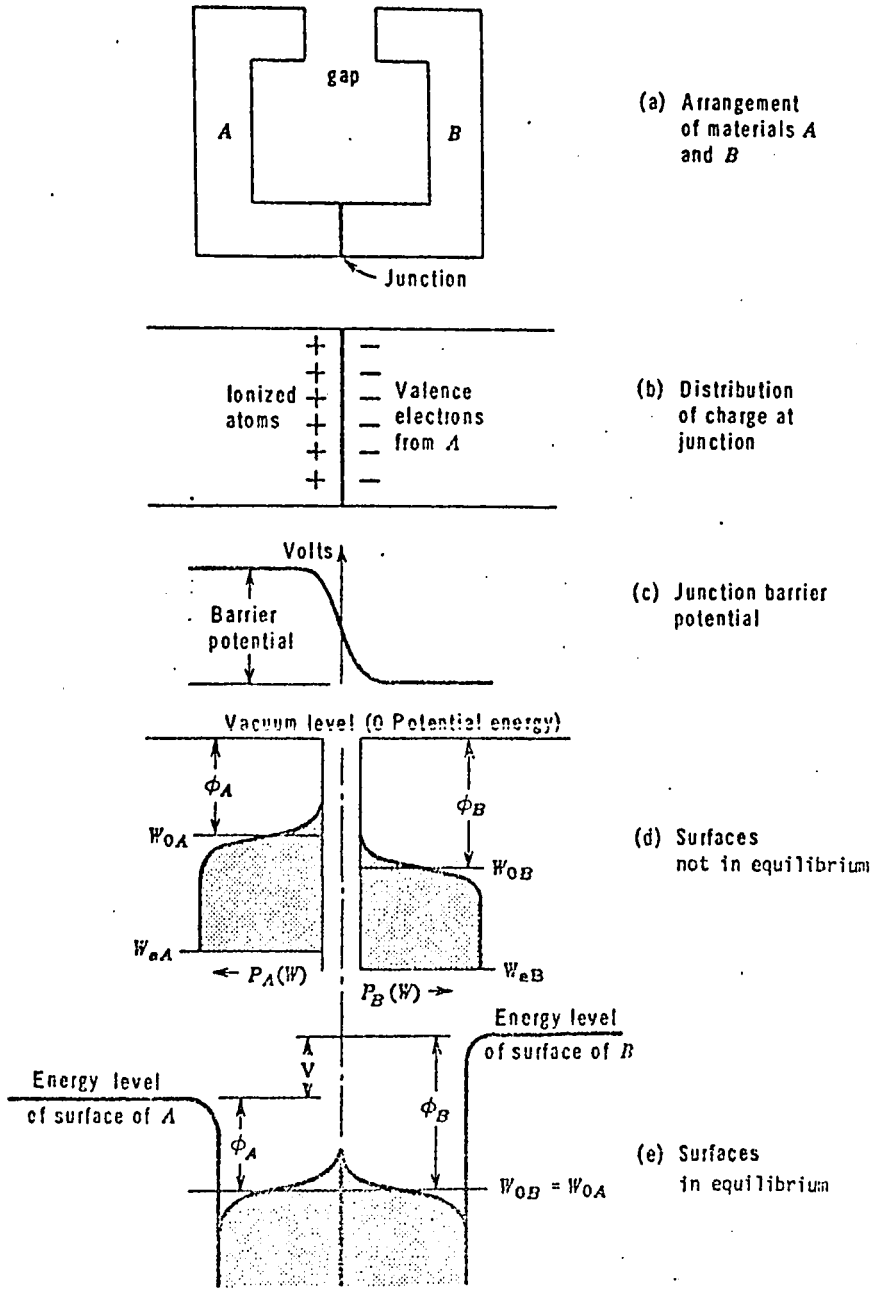

Fig. 3.15 Contact Difference of Potential between Dissimilar Materials
A - Specimen; B - Emitter

and the specimen. Referring to Fig. 3.15, in the absence of any external voltages, thermionically liberated electrons from the emitter B approach the surface of the specimen A with an energy $\phi_B - \phi_A$. However, once the electrons get close to the surface, they experience an accelerating force towards the interior of the specimen, because of the distribution of the surface field. Before striking an atom in the bulk of A, the electron would have gained an extra energy equal to the work function of A. The overall gain in energy by an electron starting from rest at the emitter surface and striking an atom in the bulk of A is

$$E = \phi_B - \phi_A + \phi_A = \phi_B \qquad \ldots (3.11)$$

Thus the work function of the target cancels out, and the correction to be applied to the electron energy reduces to the work function of the emitter, *as far as the atoms in the bulk of target are concerned.*

However, when the specimen is not a homogeneous material (consisting of different kinds of atoms), there is uncertainty in the correction to be applied. This is because different atoms on the surface have different energies with reference to the fermi level. Also, even in a homogeneous material, atoms close to the surface are bound differently from the atoms in the bulk. Because of this uncertainty in the location of the energy level of an atom situated close to the surface, the work function correction will cause a spread in the effective incident electron energy.

Another factor to be considered is the spread in electron

energy due to thermionic emission from the filament. The electrons come off with a Maxwellian energy distribution of mean energy 2kT. For a Tungsten filament which operates around a temperature of 2800 ^{o}K, the mean energy is about 0.5 eV. The energy distribution of emitted electrons has an extended tail, and therefore it is difficult to define the effective energy spread. For a Tungsten filament, this energy spread is empirically taken as 1 volt.

3.6 Effect of Modulation Amplitude

In appearance potential spectroscopy, the derivative of the total yield is obtained by introducing a small modulation on the electron beam energy, and observing the amplitude of the fundamental component at the output. True differentiation is achieved only when the amplitude of modulation is vanishingly small.

Let the modulation be of the form

$$\Delta E = v \sin\omega t$$

The x-ray output I, which is a function of the incident electron energy E, can be expressed in terms of the derivatives (denoted by primes) by Taylor expansion[45].

$$I(E+\Delta E) = I(E) + I'(E)\,\Delta E + \frac{I''(E)}{2!}\,\Delta E^2 + \frac{I'''(E)}{3!}\,\Delta E^3 + \frac{I''''(E)}{4!}\,\Delta E^4 + \cdots$$

After substituting for ΔE and simplifying, the above equation becomes

$$I = I_o + \left(I'v + \frac{I'''v^3}{8}\right)\sin\omega t - \left(\frac{I''v^2}{4} + \frac{I''''v^4}{48}\right)\cos 2\omega t + \cdots\cdots$$

For a small modulation, higher order terms can be neglected. Thus

$$I \simeq I_o + I'v \sin\omega t - \frac{I''v^2}{4} \cos 2\omega t \qquad \ldots (3.12)$$

The first term represents the dc background, and can be eliminated by ac coupling. The second term represents the fundamental component, and has an amplitude proportional to the first derivative. The larger the modulation, the larger the amplitude; but for too large a modulation, the approximation is no longer valid. The second harmonic component of the output contains information on the second derivative, and the amplitude is v/4 times that of the fundamental. However, a larger value of v can be tolerated, as there is no v^3 term in the amplitude.

In appearance potential spectroscopy, the alternating part of the signal is, at best, of the order of 10^{-11} A p-p. The fundamental component, which contains information on the first derivative is chosen for detection using a phase sensitive detector, mainly because it has the largest amplitude. Increasing the modulation increases the signal by the same proportion, but the energy resolution of the spectrum obtained cannot be better than the amplitude v. In practice, there is no further improvement gained by decreasing the modulation below about 1 volt, as there are other factors causing a spread in the electron energy, as discussed in sec. 3.5. In the present work, most of the results were obtained using 2 V p-p modulation.

The use of a square wave of the same peak to peak excursion would give 40% more harmonic content, without further degradation of resolution. However, in a transformer coupled modulating circuit

of limited bandwidth, it would cause overshoot and ringing, which must be avoided for full effectiveness of square wave modulation. The detection sensitivity can be improved by increasing the modulation to several volts, but this improvement is at the expense of energy resolution.

3.7 Noise Considerations

The major component of noise in appearance potential spectroscopy is the shot noise associated with the large dc background signal. Since a total detector is used, there is no discrimination against this noise at the detector. The dc background consisting of the bremsstrahlung is more than about 100 times larger than the peak to peak amplitude of the ac part resulting from the modulation of 1% or less. If I represents the current in the detector due to the background signal, the shot noise caused by the statistical fluctuations is proportional to $I^{\frac{1}{2}}$. If I_s is the ac signal current, the true signal to noise ratio at the output of the detector is proportional to $I_s/I^{\frac{1}{2}}$. By increasing the primary electron current hitting the sample, both I_s and I are increased in the same proportion. It can therefore be seen that the signal to noise ratio increases as the square root of the electron current. However, there are practical limitations in increasing the sample current above a few milliamperes. Too high a current would cause overheating of the sample, and possibly, electron induced surface damage and contamination which would alter the surface structure.

Because of poor signal to noise ratio inherent to appearance potential spectroscopy, it becomes imperative to use some tech-

nique such as phase sensitive detection, whereby the signal to noise ratio is improved at the expense of bandwidth. By acting as a narrow band filter, a phase sensitive detector passes only the signal and the component of the noise lying in this narrow frequency range. The smaller the bandwidth, the better the signal to noise ratio at the output of the phase sensitive detector. With this system, the response is reduced to the extent that it cannot record any changes taking place during the interval $\Delta t = 1/\Delta f$, where Δf is the bandwidth. That is, the speed at which the incident energy is scanned must be such that no significant change occurs in the signal in time Δt. Theoretically, unlimited improvement on the signal to noise ratio can be achieved by increasing the time constant and correspondingly slowing down the scan rate, provided the stability of the system permits.

The other sources of noise in appearance potential spectroscopy are

1. shot noise and thermionic noise of a multiplier tube, when a multiplier detector is used,
2. ions entering the detector when the vacuum is poor,
3. accumulation of charge on insulators in the system,
4. slow drift caused by temperature changes of samples during scan,
5. inherent noise in the electronic circuits,
6. power supply instabilities, and
7. electrical, magnetic and vibrational pick-up from the environment.

When a multiplier detector is used to measure low signal levels, the multiplier noise will be the predominant factor. At higher signal levels, in the absence of a multiplier, the noise in the pre-amplifier will be the major component. Very low frequency flicker noise observed, is believed to be a result of charging of small particles of dust on the mesh wires in front of the specimen and on the photocathode. The observed hysteresis effects between the voltage scans in opposite senses, is probably due to temperature changes of the sample. At a vacuum of 10^{-8} torr, the noise due to ions was found to be negligible. Power supply instability and environmental pick-up can be minimized by proper design and adequate shielding.

3.8 X-ray Production Efficiency

The quantum efficiency of production of x-rays from a target bombarded by electrons is very low, most of the energy of the incident electrons being converted into heat. As the electrons experience a deceleration upon entering the target, they emit bremsstrahlung having energies varying from a low value up to the incident electron energy. The quantum efficiency of production of this continuous radiation is given by the semi-empirical relation[31]

$$\eta_b = 1.04 \times 10^{-9} \; Z \; (V_1 - V_c)^{1.65} / V_c^{0.65} \qquad \ldots (3.13)$$

where Z is the atomic number of the target, V_1 the incident electron energy, and V_c the lower energy limit of radiation which escapes from the target.

This relation has been found to be satisfactory for medium

and high atomic number elements and for energies of several keV and above. It becomes increasingly inaccurate for incident energies below 2 keV. There are no other expressions which are considered valid in the low energy range.

The characteristic x-ray production is a function of the overvoltage, (V_1-V_k), where V_k is the absorption edge of the target. The quantum efficiency of production of characteristic radiation can be expressed as[31,54]

$$\eta_k = 1.04 \times 10^{-9} \; Z \; R \; w \; (V_1-V_k)^{1.65}/V_k^{0.65} \qquad \ldots (3.14)$$

where R is the ratio of the probability for K ionization to that for the production of bremsstrahlung of energy greater than V_k, and w the fluorescent yield of K radiation.

For light elements, there is considerable uncertainity in the values of R and w. The equation also loses its validity for values of V_1 close to the absorption edge V_k, as occurs in appearance potential spectroscopy. At energies below 1000 eV, the fluorescent yield is expected to be extremely small, most of the transitions yielding Auger electrons[55]. Cosslett[54], Archard[56] and Campbell[57] have investigated the efficiency of x-ray production from light elements, and experimental measurements have been made using a flow proportional counter for the absolute counting of x-ray quanta by Dolby[58]. The values obtained by different experimenters vary widely. However, it appears that the efficiency of characteristic x-ray production from light elements is an order of magnitude higher than that predicted by the semi-empirical theories.

To be able to calculate the detection sensitivity of appearance potential spectroscopy, it is necessary to know the production efficiency of bremsstrahlung and characteristic radiation for small values of electron energy above the absorption edge. With the data presently available, it is not possible to make even a rough calculation.

CHAPTER 4. DESCRIPTION OF THE APPARATUS

It is less than two years since appearance potential spectroscopy was first demonstrated as a tool for surface analysis, particularly of light elements. At the time the present experiments began, there was very little information available on the sensitivity of detection and inherent limitations of appearance potential spectroscopy. However, rough estimates of signal intensities based on extrapolated values of x-ray production efficiencies showed that there would be measurable output from a Carbon target, for incident electron currents of a few microamperes. Thus, the project on appearance potential spectroscopy was started with an ambitious goal of developing a scanning electron beam spectrometer, capable of producing micrographs of the distribution of light elements in a sample. In this chapter, the experimental developments that led to the present apparatus are described in chronological order.

The first attempt was made with a focused electron beam and a windowless soft x-ray detector with photomultiplier. It did not yield successful results because of very poor signal to noise ratio at the low electron current attainable with a focused beam. It was then realized that currents of the order of a milliampere would be needed to raise signals strong enough for easy detection, and thereby establish the sensitivity of detection to various elements. The subsequent experiments were carried out with a simple Tungsten filament capable of delivering currents up to a few milliamperes, in a flood beam spread over a few cm^2 of specimen surface.

The first x-ray detector was made of a Beryllium Copper cup

as the photocathode and a scintillator-photomultiplier as the photoelectron collector. A vacuum of 5×10^{-8} torr was maintained using a turbomolecular pump. The appearance potential spectrum of Carbon was obtained from this apparatus, using electron currents in the range of a few hundred microamperes, the lowest current that gave a reasonable signal being 15 μA. The noise from the photomultiplier was the limiting factor, as there was no facility for cooling it. Another problem was the contamination of the sample surface by the cracking of residual hydrocarbons in the vacuum under the action of the electron beam. This resulted in the formation of a layer of Carbon which masked the sample surface under examination.

A cleaner vacuum with facilities for baking was found to be necessary to minimize the contamination. An ion pump was therefore added, using the turbomolecular pump for the initial pump down, and the scintillator-photomultiplier was replaced by a simple electron collector connected to a low noise electrometer amplifier. These improvements, together with surface cleaning by ion bombardment, yielded good results from many different samples.

Further modifications were made, as a result of which, the specimen in the form of a thin foil could be heated in vacuo to known temperatures. This not only facilitated surface cleaning, but permitted controlled oxidation of specimens to form known thicknesses of oxide film on the surface.

The details of the experiments summarized above are described in the following sections.

4.1 Attempts with a Focused Electron Beam

The first attempts on appearance potential spectroscopy were made on a modified Material Analysis Co. Scanning Electron Microscope, Model MAC 700. The MAC electron column is capable of delivering beam currents of a few microamperes, focused on to a spot several microns in diameter. The lowest accelerating voltage for which the electron gun is designed to operate, however, is only about 1000 V, and to obtain lower beam energies, it was necessary to float the specimen towards the gun potential. By maintaining an axially symmetric retarding field, the distortion of the spot shape at the specimen could be minimized.

Fig. 4.1 shows the schematic diagram of the apparatus. The electron beam emerging from the final lens with an energy of 1500 eV, travelled through the cylindrical mesh A, before striking the specimen. This mesh and the specimen were at the same potential obtained from a slow dc ramp generator, of range 0 to 1500 V. Thus the incident energy of electrons on the specimen could be made to vary from 0 to 1500 eV. The outer concentric mesh B was maintained at a potential of -1500 V so that the back scattered electrons from the specimen were prevented from entering the detector. A large portion of the x-rays generated at the specimen were transmitted through the two meshes and struck the photocathode made of Beryllium Copper, in the form of a cup. The photoelectrons liberated under the action of the x-rays, were accelerated on to an annular scintillator, the surface of which had a thin conducting layer of evaporated Carbon. A potential of 6 kV was sufficient to ensure that the electrons

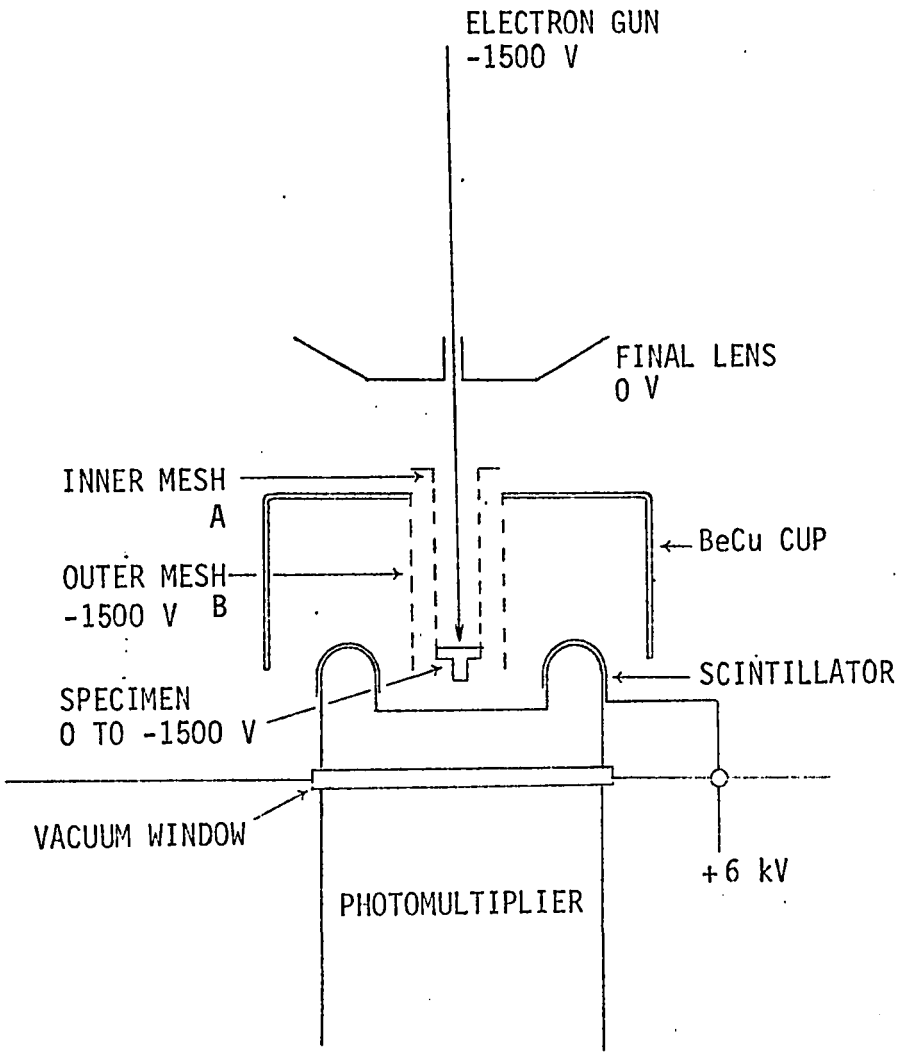

Fig. 4.1 The Detection Scheme with a Focused Beam

were able to penetrate the Carbon film and produce light output at the scintillator.

The complete detector assembly was situated under the final lens and in the specimen chamber, which was evacuated to 2×10^{-7} torr by a large capacity ion pump. A transparent vacuum window transmitted the scintillator output to the photomultiplier located outside the vacuum. The electron energy was modulated by applying a 5 V p-p 2 kHz sinusoidal signal to the gun supply, through an isolating transformer. The output of the photomultiplier was connected to an ac coupled high input impedance operational amplifier, tuned to 2 kHz, and the amplified signal was detected by a phase sensitive detector having the same reference source as the gun modulation. Finally, the dc output of the phase sensitive detector was plotted against the specimen potential using an X-Y recorder.

Contrary to the expectations, the recorder trace failed to show any structure corresponding to an incident beam energy of 284 eV at the specimen, which was an evaporated layer of Carbon. Increasing the detector gain merely increased the slope of the curve and the amplitude of the noise fluctuations. The failure is attributed to the following reasons:

1. Even at the maximum available beam current of 3 μA, the signal to noise ratio was much poorer than expected.

2. The photomultiplier had excessive background noise compared with the available signal, but it was not feasible to cool it to reduce the noise.

3. Internal leakage and arcing limited the maximum scintil-

lator voltage to 6 kV. Higher voltages like 20 kV would have improved the signal to noise ratio.

4.2 Development of the Present Apparatus

After the first attempt failed, it was realized that the basic sensitivity of the technique must be established before using a focused beam. It was decided to use a flood source of electrons obtained from a Tungsten filament, and a sample of a few cm^2 area, so that currents up to a few milliamperes could be produced with practically no surface damage due to heating.

Fig. 4.2 shows the schematic layout of the system. The specimen which was in the form of a disc of 1 cm diameter, was located about 0.5 cm away from the filament made of 0.005" Tungsten wire, bent in a U of total length about 1 cm. The mesh in front of the assembly was biased 50 V negative with respect to the filament, so that electrons emitted from the filament and backscattered by the specimen were prevented from reaching the detector. The photocathode was made of Beryllium Copper, in the form of an open box of triangular shape, with the open end covered by a fine mesh and facing the specimen. The solid angle subtended by the photocathode at the specimen was more than π str., and both the meshes of 50 lines per inch, had a transmission of about 90%. Photoelectrons released from the walls of the box were accelerated through the aperture at the bottom to the scintillator surface, maintained at a potential of 12 kV, and the light output of the scintillator fell on a photomultiplier through an optical window. The light emitted from the filament was prevented from reaching the photomultiplier by the evaporated

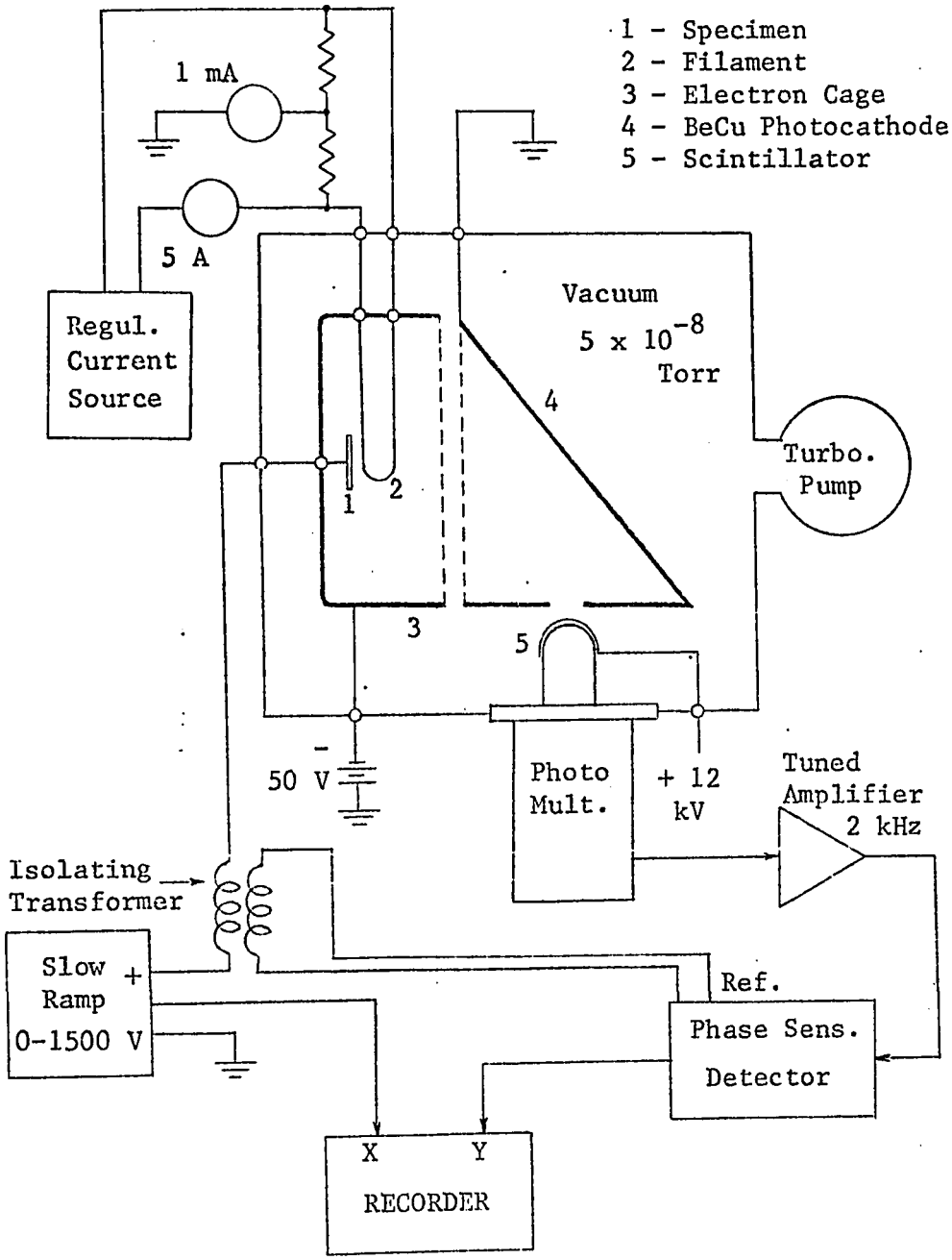

Fig. 4.2 Schematic Diagram of the Appearance Potential Spectrometer

Aluminum coating on the surface of the scintillator. The optimum thickness of the coating, which should be opaque to light but fairly transparent to 12 keV electrons, was found by trial. (It was of the order of 2000 Å.) The filament was heated by a current of 2 to 2.5 A dc obtained from a regulated current source. The specimen potential could be varied continuously from 0 to 2000 V by a motor driven power supply. An isolating transformer was used to apply the modulation, which had a frequency of 2 kHz and amplitude up to 5 V p-p. The photomultiplier output was fed to an ac coupled, narrow band amplifier tuned to 2 kHz. The output of the phase sensitive detector, which is proportional to the first derivative of the total x-ray yield, was plotted in the X-Y recorder to obtain the appearance potential spectrum of the specimen.

4.2.1 The Initial Vacuum System

The vacuum chamber which housed the specimen, electron source and detector, was made from a 6 way Tee, with demountable flanges, all of stainless steel. After several trials, it was found that Gold wire made the best seals. The sealing rings were made of 0.030" pure Gold wire, the ends of which were welded together under a small oxy-acetylene flame. As shown in Fig. 4.3, the flanges were of simple design, with only a step needed to retain the ring which seals against flat surfaces, when bolted tight. The inevitable bead formed at the welded joint in the ring did not cause trouble provided its cross section was not more than about 25% of the original cross section. Heating the entire ring with a flame to dull red heat before inserting on the flange, softened the Gold and facilitated sealing.

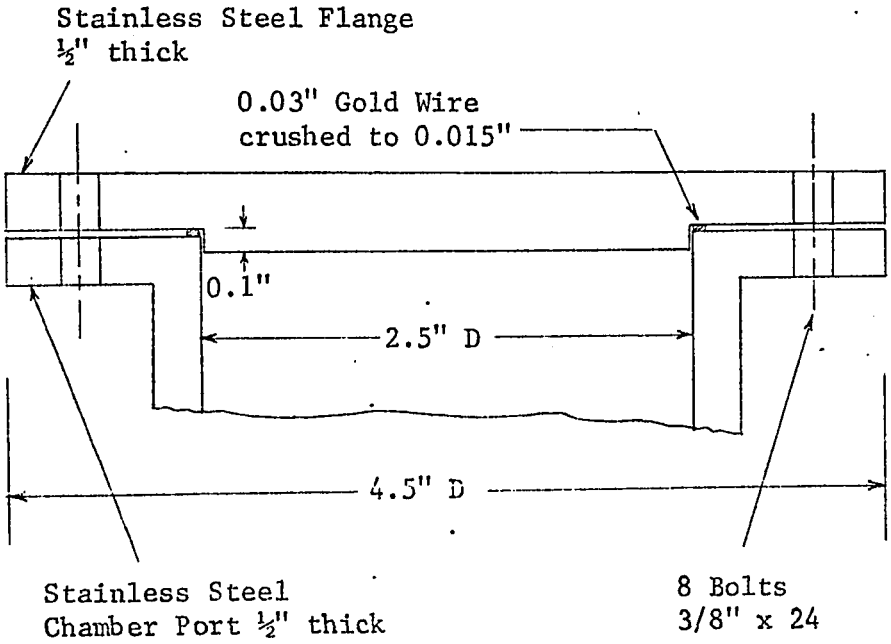

Fig. 4.3 A Typical Gold Wire Vacuum Seal

When carefully handled, the same seal could be used as many as ten times without deterioration in performance. The greatest advantage of Gold wire seals was that the flanges could be easily machined to seal flat faced ports of any size. Though generous quantities of expensive Gold wire were required, there was no loss of material, as the used wire could be recycled, and over a long period this proved to be a very economical vacuum seal technique.

A sensitive mass spectrometer (AEI Model MS10) was fitted to one of the ports and a nude ionization gauge to another. This facilitated leak detection and measurement of pressure close to the specimen. However, because of the use of a plastic scintillator for photoelectron detection, the vacuum system was not bakeable. The chamber was evacuated by a turbomolecular pump of 260 litres per second (Sargent-Welch type 3102D) and ultimate vacuum capability of 2×10^{-9} torr.

4.2.2 Shortcomings of the Initial Vacuum System

The first specimen used for experiment was an evaporated layer of Carbon. The appearance potential spectrum of Carbon was obtained at electron currents varying from 15 μA up to 500 μA. At lower currents, the signal to noise ratio was too poor to give reasonable trace, and at higher currents, the photomultiplier saturated. Fig. 4.4 shows photographs of the specimen, filament and detector, and the results are discussed in the next chapter.

As the system could not be baked, the vacuum measured during experiments was about 5×10^{-8} torr. The mass spectrum of the residual gases (Fig. 5.2) showed significant quantities of hydrocarbons

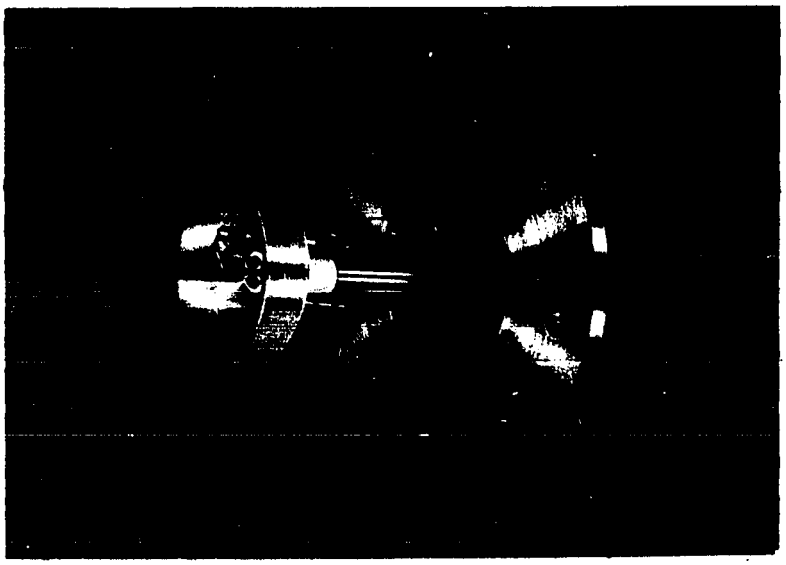

(a) Specimen and Filament

(b) Soft X-ray Detector

Fig. 4.4 Photographs of the Internal Parts

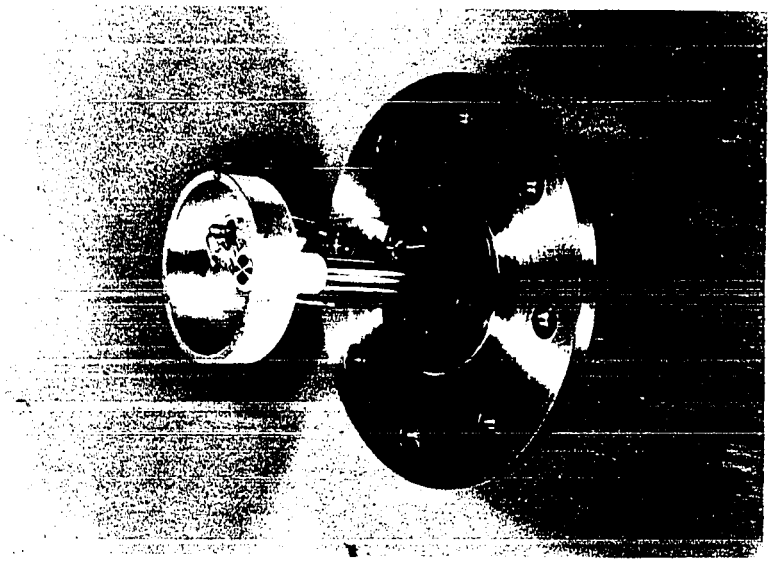

(a) Specimen and Filament

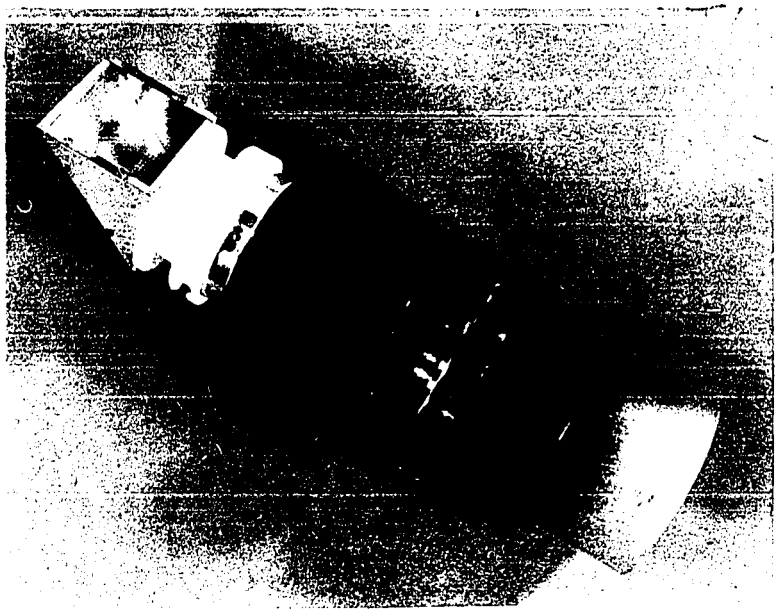

(b) Soft X-ray Detector

Fig. 4.4 Photographs of the Internal Parts

present. This resulted in the deposition of a layer of Carbon on the specimen under the action of the electron beam. Because of this Carbon contamination, the appearance potential spectra of other elements could not be obtained. It was therefore necessary to remove this contamination by improving the vacuum and by surface cleaning techniques.

4.2.3 Improvements in the Vacuum System

If p is the partial pressure of any gas in the system, the rate at which the molecules strike a surface is given by

$$\nu = \frac{3.5 \times 10^{22}}{(MT)^{\frac{1}{2}}} \quad \text{molecules cm}^{-2} \text{ torr}^{-1} \qquad \ldots (4.1)$$

where M is the molecular weight of the gas and T the temperature. If all these molecules stick to the surface and contribute to contamination, the rate of growth of the layer is of the order of 230 $\mathring{A}$/hr at 10^{-8} torr, 23 $\mathring{A}$/hr at 10^{-9} torr and so on. At pressures in the ultrahigh vacuum range (better than about 10^{-8} torr), a reasonable observation time is obtained before contamination becomes serious. In the absence of leaks in a vacuum system, the ultimate pressure reached is decided by the effective pumping speed and the outgassing rate of adsorbed and dissolved gases from the walls and interior parts of the system. Baking the entire vacuum system for several hours at 300 to 400° C will reduce the outgassing rates by two or more orders of magnitude and it will then be possible to maintain an ultrahigh vacuum with a clean pump having reasonable speed.

The first step towards attaining the ultrahigh vacuum needed

for the experiment, was to make the system completely bakeable. The scintillator-photomultiplier detector was replaced by a simple electron collector and electrometer amplifier, as shown in Figs. 4.5 and 4.7. The Beryllium Copper photocathode was also replaced by an Aluminum box of triangular cross section, having an evaporated layer of Gold on its interior. Not only did Gold exhibit good photoelectric yield over a wide range of photon energy, but it was unaffected by exposure to air and had reproducible photoelectric characteristics. It was also easy to replenish the evaporated layer if it was worn off or accidentally scratched. The photoelectrons were collected by a disc shaped electrode having a positive bias of about 50 V, applied through the load resistance of 50 MΩ.

For compatibility with ultrahigh vacuum, all the internal parts were made of stainless steel and Boron Nitride which is a machineable, sintered ceramic with good insulation properties. A 20 litres /second ion pump (Ultek Corp. Model 60-650, Boostivac) with a built-in Titanium sublimation unit, was connected to one of the chamber ports. The original turbomolecular pump was retained for the initial pump down, but a 1½" valve with a polyimide seal was added in order to isolate the chamber when required.

The air admit valve had a Teflon seal, and this limited the temperature of bake-out to about 250° C. The whole chamber and the ion pump could be covered by a demountable box made of Asbestos lined with thin Aluminum sheets, in order to minimize heat losses and to make the temperature distribution more uniform during baking. The heat was provided by 8 heater strips, 125 W each, bolted on to the

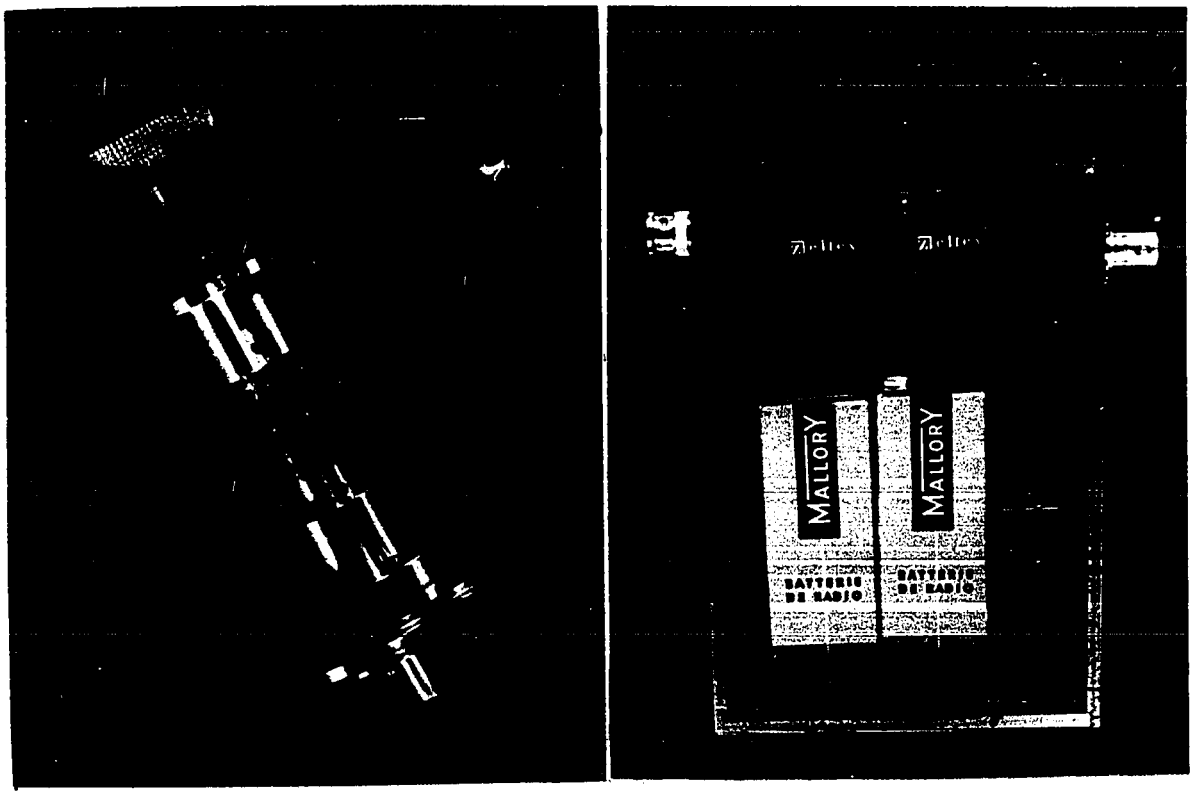

Fig. 4.5 Photographs of the modified Detector and Pre-amplifier

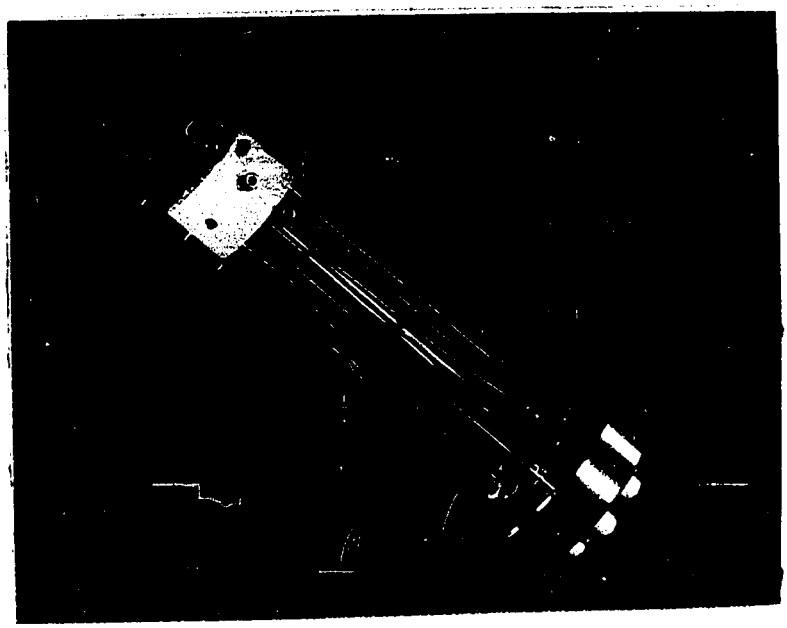

Fig. 4.10 A Photograph of the modified Specimen Holder with Heating facility. The Filament runs across the face of the Specimen, and the Thermocouple is attached to its back.

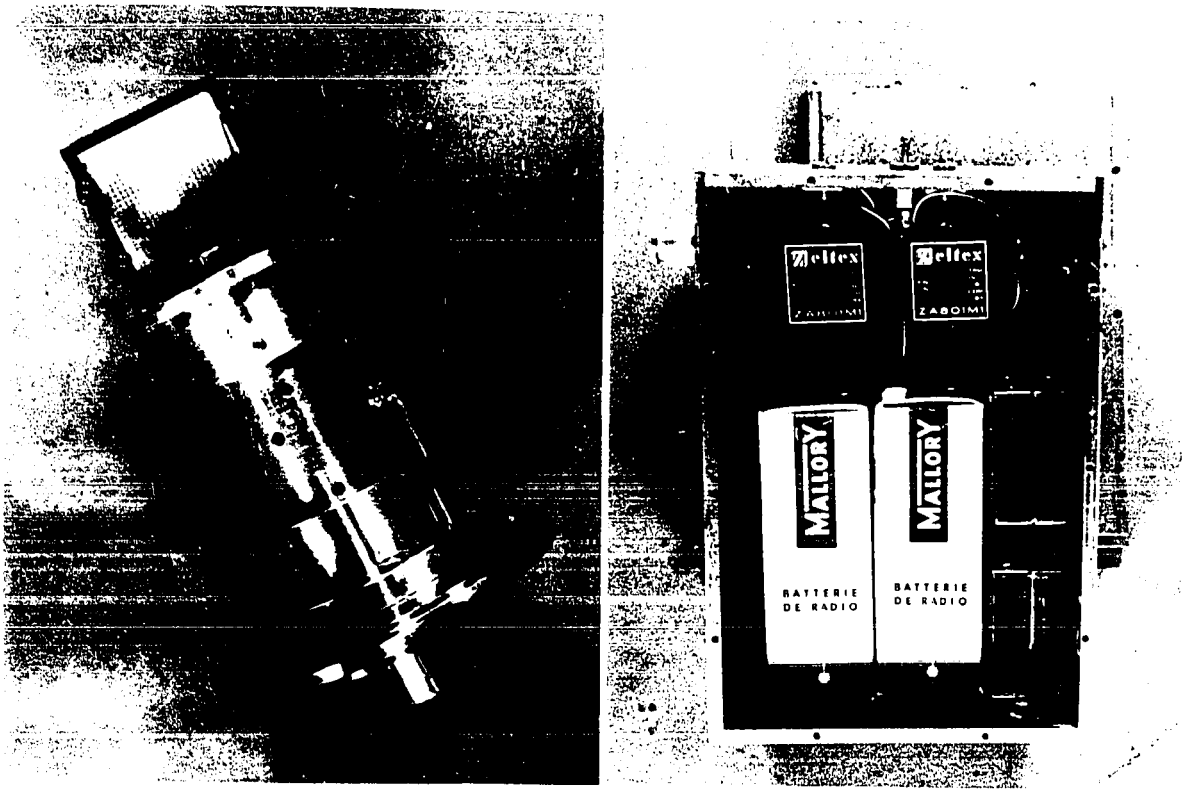

Fig. 4.5 Photographs of the modified Detector and Pre-amplifier

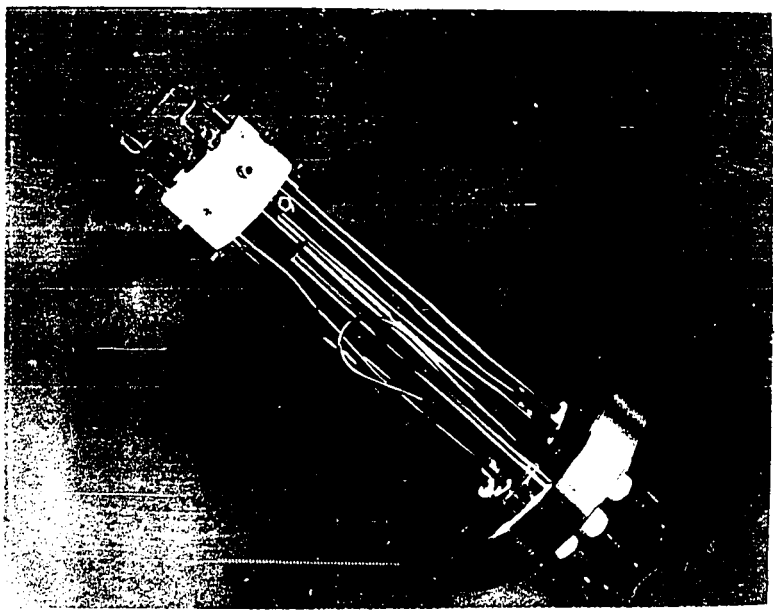

Fig. 4.10 A Photograph of the modified Specimen Holder with heating facilities. The Filament runs across the back of the specimen, and the Thermocouple is spot-welded to the front.

chamber and the pump, and the temperature was monitored by Iron-Constantan thermocouples located at salient points. Severe non-uniformity in temperature near the flanges would cause leaks at the Gold wire seals because of unequal expansion, but this was avoided by uniformly distributing the heaters and by properly shielding the chamber ports against heat losses.

During baking, which usually lasted 12 to 18 hrs, all the pumping was done by the turbomolecular pump, the ion pump being shut off, and the magnets removed. At the finish of the bake-out process, the pressure measured was about 10^{-7} torr, with the chamber still hot. At this point, the ion pump was switched on and after outgassing all filaments for a minute, the turbomolecular pump was isolated and shut off. In about two hours, the chamber cooled down to room temperature and the pressure dropped to about 2×10^{-9} torr, with the help of the Titanium sublimation element. Thereafter, the pressure stayed at that value with only the ion pump operating. The mass spectrum of the residual gases taken under these conditions is given in the next chapter (Fig. 5.4).

4.2.4 Surface Cleaning by Ion Bombardment

Even after the improvements in the vacuum were made, the appearance potential spectrum taken on a stainless steel sample showed mostly Carbon and very faint traces of the true constituents. As the partial pressure of residual hydrocarbons indicated by the mass spectrometer was very low, the contamination must have been the result of deposits present on the specimen in the beginning, perhaps during cleaning with solvents. Heating the specimen to several hundred

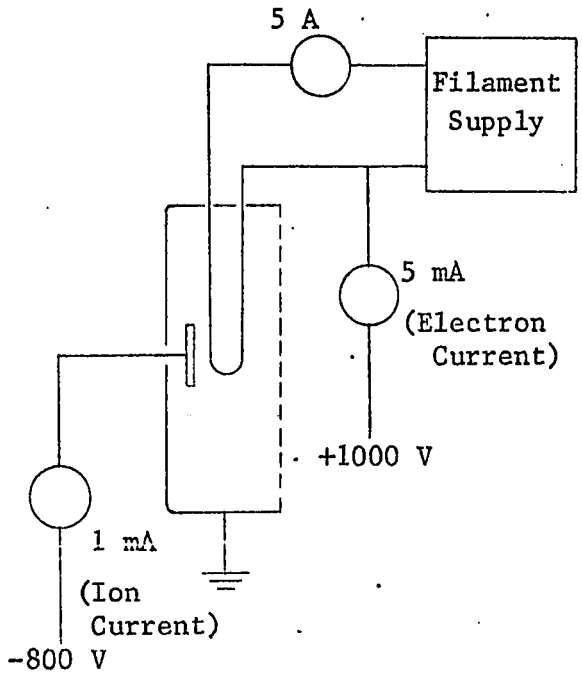

Fig. 4.6 The Circuit Diagram for Ion Bombardment

degrees is one way of getting rid of surface contamination,but this could not be done without further modifications. Bombarding the surface by energetic ions is another effective way of surface cleaning.

Ions of the heavy inert gas, Argon, were used for the bombardment to ensure that there was no contamination by the process itself. The simplest way of performing ion bombardment was to apply a suitable negative potential (500 to 1000 V) to the specimen, with all other electrodes grounded. After shutting off the ion pump, pure Argon was admitted into the system through a controlled leak valve until the pressure was sufficient (of the order of 10^{-2} torr) to maintain a glow discharge between the specimen and other electrodes. The cleaning action took place when the Ar^{+} ions hit the sample surface and sputtered away a layer of material on the surface. At 800 eV, a bombarding current of 1 mA sustained over 15 min was found to be sufficient to remove the Carbon deposit from the specimen.

One serious objection to this method of ion bombardment was that the glow discharge extended over all the connecting leads to the specimen and the material sputtered off deposited itself on the insulators, eventually resulting in a short circuit. It also made it impossible to estimate the fraction of the ion current actually hitting the sample.

Fig. 4.6 shows a better way of performing ion bombardment, making use of thermionic emission from the filament to initiate the production of ions. A current of a few milliamperes was maintained between the hot filament and the cage, to which was applied a poten-

tial of about 1000 V positive with respect to the filament. The ions generated by the interaction of these electrons with the gas molecules, were accelerated towards the specimen surface by the negative potential applied to the specimen. As the ion production was confined to the inside of the cup, sputtering took place only on the specimen and not on the connecting lead located outside the cup. A separate filament and anode could be used to produce the electron current in order to provide better control over the stream of ions hitting the specimen, but it was not necessary in the present case.

Using the circuit described above, ion currents of the order of 100 μA at 800 V were produced, at pressures as low as 5×10^{-4} torr. A dynamic partial pressure of Argon was maintained during the operation, by controlling the leak valve and by partially opening the turbo isolation valve, with the pump running (but the ion pump shut off).. For cleaning the specimen surface, a 50 μA ion current for 10 min at 800 V was found to be sufficient.

In addition to sputtering off the contamination layer, the ions might also induce some surface damage, the more energetic the ions, the more severe the damage. Furthermore, as the rate of etching differs from element to element, the composition of the surface under examination might undergo changes during the process. However, no detailed study was made to find out the extent or type of surface damage, or to optimize the cleaning process for minimum damage.

In the vacuum system, no isolation valve was used between the chamber and the ion pump, because of the difficulty of obtaining

a large diameter bakeable valve. During Argon admission, the pump was thefore exposed to the gas, which is usually undesirable. However, as the turbo pump has good pumping speed for Argon, it was possible to bring the pressure down to 10^{-8} torr, at which point the turbo pump could be isolated. The ion pump, assisted by the sublimation unit, was then able to bring the pressure further down to about 5×10^{-9} torr, a little above the original pressure. There was no problem of contamination, as the extra pressure was due mainly to Argon.

4.2.5 The Pre-amplifier Considerations

The photoelectron current collected by the positively biased electrode, as mentioned before, was detected by a low noise, high gain pre-amplifier mounted directly on the flange. This was done to minimize the input capacitance and thereby increase the speed of response.

The pre-amplifier, shown in Fig. 4.7 is battery operated and well shielded against electrical and magnetic pick up. The photoelectron current flows through the load resistance of 50 MΩ, and the voltage developed across it is amplified by a pair of FET input operational amplifiers with a gain 100 each. The internal circuit ground of the first stage is biased positive with respect to the external ground by the battery B_2, and this establishes the necessary potential at the collector electrode to attract the photoelectrons. The second amplifier stage operates on an independent set of batteries B_3, with the common terminal at ground potential. The use of separate batteries not only permits the internal ground shift, but

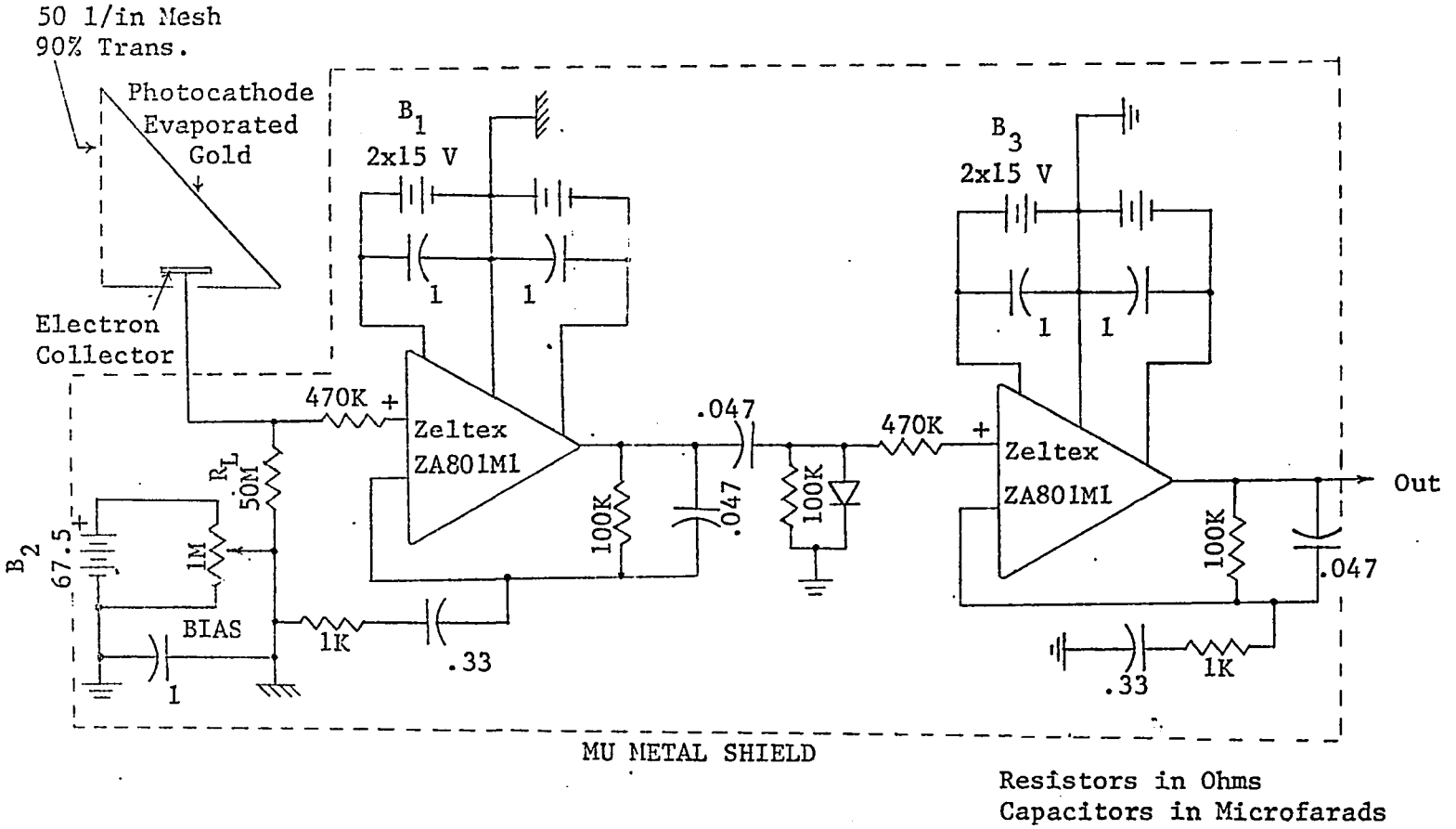

Fig. 4.7 The Schematic Diagram of the Detector and Pre-amplifier

avoids objectionable feedback between the two stages, which would exist with a common battery supply. The diodes at the input of the operational amplifiers offer protection against breakdown of the FET's which may be damaged by voltage surges. The input capacitance of about 30 pF measured between the collector lead and ground, limits the upper cut off frequency to about 1000 Hz, with a load resistance of 50 MΩ. The overall transfer impedance of the pre-amplifier at 500 Hz (the centre frequency) is

$$Z_{eff} = 50 \times 10^{6} \times 10^{4} = 0.5 \times 10^{12}\Omega = 0.5 \text{ V/pA} \quad \ldots (4.2)$$

The RC time constants of the coupling and feedback networks are such that, for frequencies above and below 500 Hz, the gain falls off at 18 db/oct.

The amplifier was tested at input currents in the range of a pA, at 500 Hz. The back ground noise arises mainly from the inherent noise in the input stage of the first amplifier. Because of the all shielded construction and self-contained battery power supplies, the environmental pick up was considerably reduced. There was no noticeable 60 Hz component at the output, but very faint traces of the 8th harmonic (480 Hz) were observed. With an input signal of 10^{-12} A p-p at 500 Hz, the signal to noise ratio measured at the output was about 5.

In the circuit described above, the main factor that decides the maximum frequency of operation is the capacitance presented at the amplifier input by the collector electrode and the connecting lead. Park and Houston[29,30] have devised a simple circuit shown in Fig. 4.8,

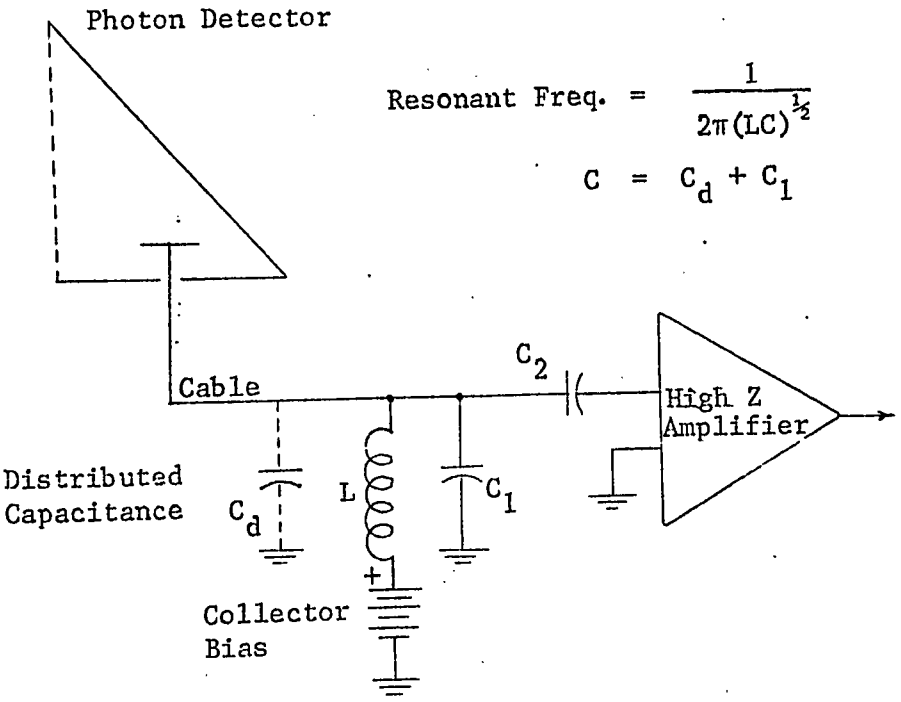

Fig. 4.8 Tuned Circuit to overcome the effect of large Distributed Capacitance

which can tolerate large values of input capacitance. A high Q(≈200) toroidal inductor of several Henrys forms a tuned LC tank circuit, in parallel with the total capacitance at the collector lead. In this circuit, the inductor and the amplifier can be placed in a convenient location, using several feet of coaxial cable for connection. Extra capacitance can be added if a lower resonant frequency is desired.

When signal levels are of the order of 10^{-10} A, this is perhaps the most convenient way of coupling the collector output to the amplifier. At lower currents, the environmental vibration and acoustic noise picked up by the inductor, which is of the order of 10^{-11} A, limits the usefulness of the circuit. Another source of noise is the leakage current through the coupling capacitor which isolates the bias source from the amplifier. Although the circuit permits operation at higher modulating frequencies, it is doubtful if signals below 10^{-11} A could be detected with a signal to noise ratio better than 1, by this method.

Normally, a modulating frequency of 1 kHz or more is preferred, in order to minimize the noise pick up due to power frequency and its harmonics. In the present system, as the pre-amplifier was battery operated and adequately shielded, it was feasible to use a modulating frequency of 500 Hz, without deterioration in performance.

4.2.6 The Emission Regulator

Themionic emission from a filament is very sensitive to

slight changes in the filament current and aging of the wire itself. In addition to this, when the specimen potential is varied, the emission current also changes due to space charge effects, the change being very pronounced at lower potentials. Under these conditions, it is not enough to supply the filament with a constant current. The only way in which the emission current can be kept constant is to use feedback stabilization.

The circuit diagram of the emission regulator is shown in Fig. 4.9. The emission current is sensed between the filament and ground, by the FET input operational amplifier connected as a current to voltage converter. The output of the amplifier energizes a light emitting diode, optically coupled to a photosensitive resistance which forms part of the filament control circuit. Complete isolation between the emission sensing and the filament current circuits is achieved by the use of this optical coupling.

As the filament current circuit is floating above ground, very good isolation of the power supply to ground is necessary to ensure that the leakage current does not interfere with the emission current being sensed by the amplifier. The commercially available mains operated power supplies do not have the isolation needed, and therefore, a 6 V storage battery is used to power the filament circuit.

The stabilizing action of the circuit arises from the negative feedback through the optical coupler, which adjusts the filament current in the proper sense, whenever changes in the emission current occur. The set point can be varied from 0 to 5 mA, and the overall open loop gain adjusted to give the best regulation without introdu-

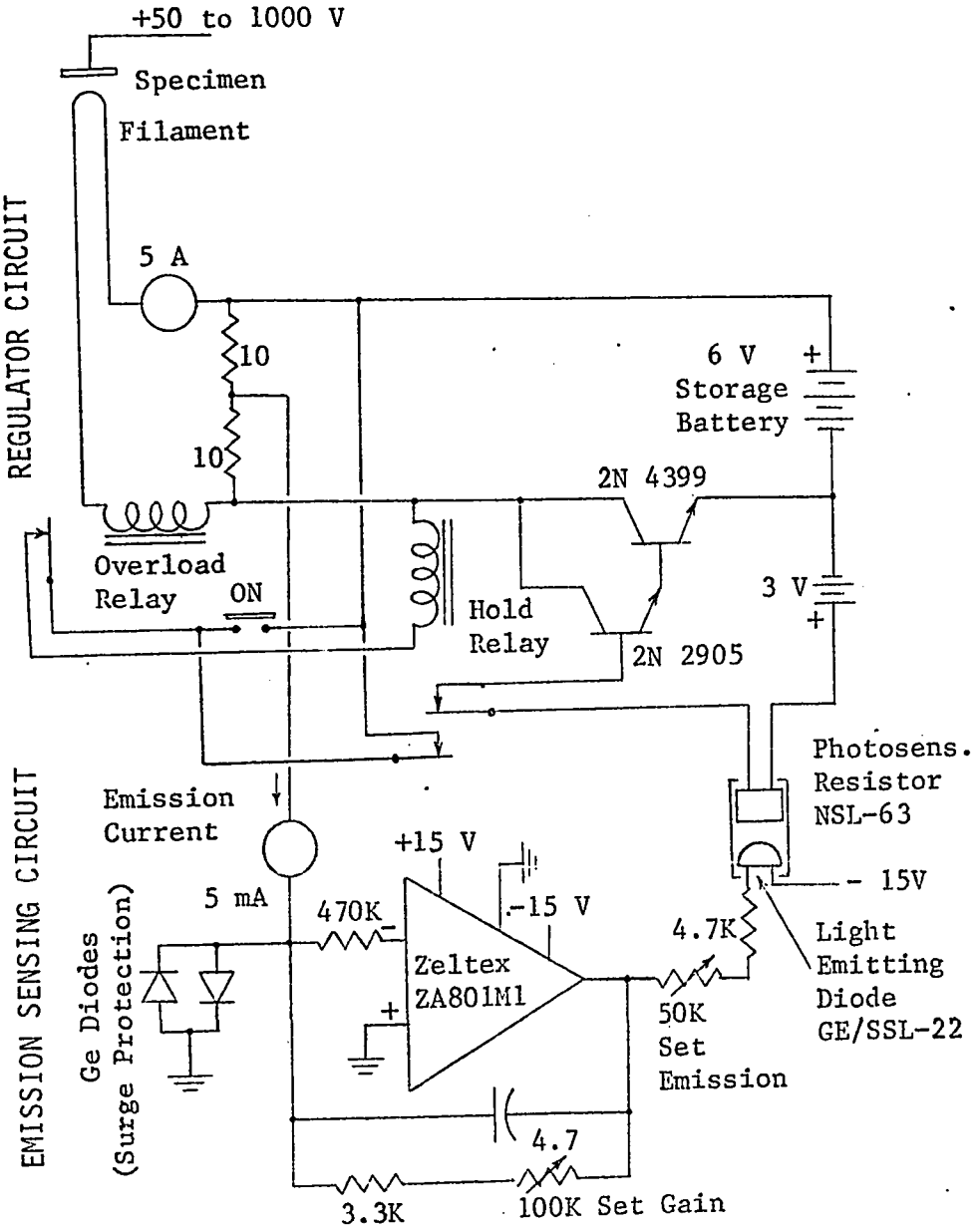

Fig. 4.9 The Circuit Diagram of the Emission Regulator

cing instability and hunting.

While the circuit is operating at a set value of emission current, if the specimen potential is reduced below about 100 V, the effect of space charge around the filament tends to decrease the emission, which is overcome by an automatic increase in the filament current. In the event the specimen potential is accidentally reduced too much, the filament is protected from burning out, by an electro-mechanical relay which shuts off the filament when the current exceeds 3 A.

4.2.7 The Specimen Heating Facility

In the apparatus described so far, disc shaped specimens were used and there was no provision made either to heat the specimen during experiments or to measure its temperature. It was realized that such facilities, if provided, would not only simplify surface cleaning operations but would permit controlled reactions such as oxidation and reduction to form known surface compositions, which could then be used as standards for calibration.

Fig. 4.10 shows a photograph of the modified specimen holder and filament. A thin flat specimen, about 1 cm wide and 2 cm long was spot welded to support electrodes which could be externally connected to a 6 V storage battery capable of delivering several tens of amperes of heating current through the specimen. For heating a 0.010" thick Iron specimen to 800° C in vacuo, the current required was about 25 A, it being less for thinner foils. The temperature of the specimen was measured by a fine thermocouple made of 0.003" dia. Iron and Constantan wires spot welded to its back at the centre. By

using a battery operated electrometer with floating ground, the temperature could be monitored even when the specimen was at a high potential. A quartz window was provided at the top of the chamber for visual inspection of the specimen or to measure the surface temperature with an optical pyrometer. There was some non-uniformity in the temperature distribution on the specimen, as the conduction of heat through the two supporting electrodes kept the ends cooler than the middle. However, an area about 1 cm x 1 cm in the centre, where most of the electrons struck during the experiment, had a reasonably uniform tempertaure.

Fig. 4.10 also shows the Tungsten filament mounted about 0.5 cm away from the specimen, spot welded to two electrodes on the sides of the specimen. The filament did not have a bend as in the previous cases, but ran straight across the width of the specimen strip, the thermionic emission being concentrated to about 0.75 cm in the middle, while carrying a current of 2.5 to 3 A. Two extra electrodes were provided to accommodate an evaporator source from which fresh layers of material could be deposited in vacuo on the specimen surface for examination by appearance potential spectroscopy.

A photograph of the complete apparatus is shown in the next page. The turbomolecular pump is located under the aluminum table which supports the vacuum chamber and the ion pump. The pre-amplifier box can be seen on the right side of the chamber, supported by a bracket.

The results of the experiments are discussed in detail in the next chapter.

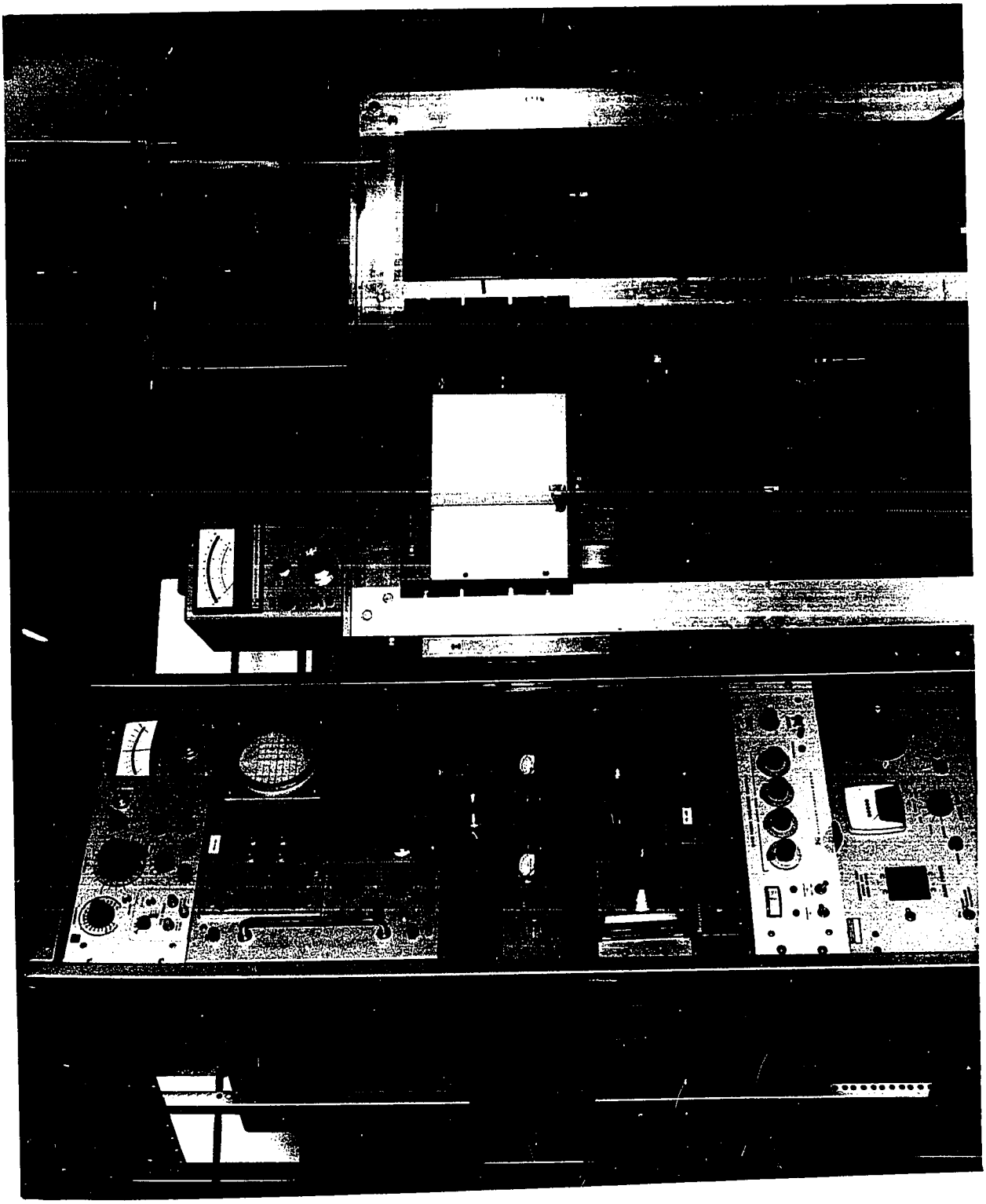

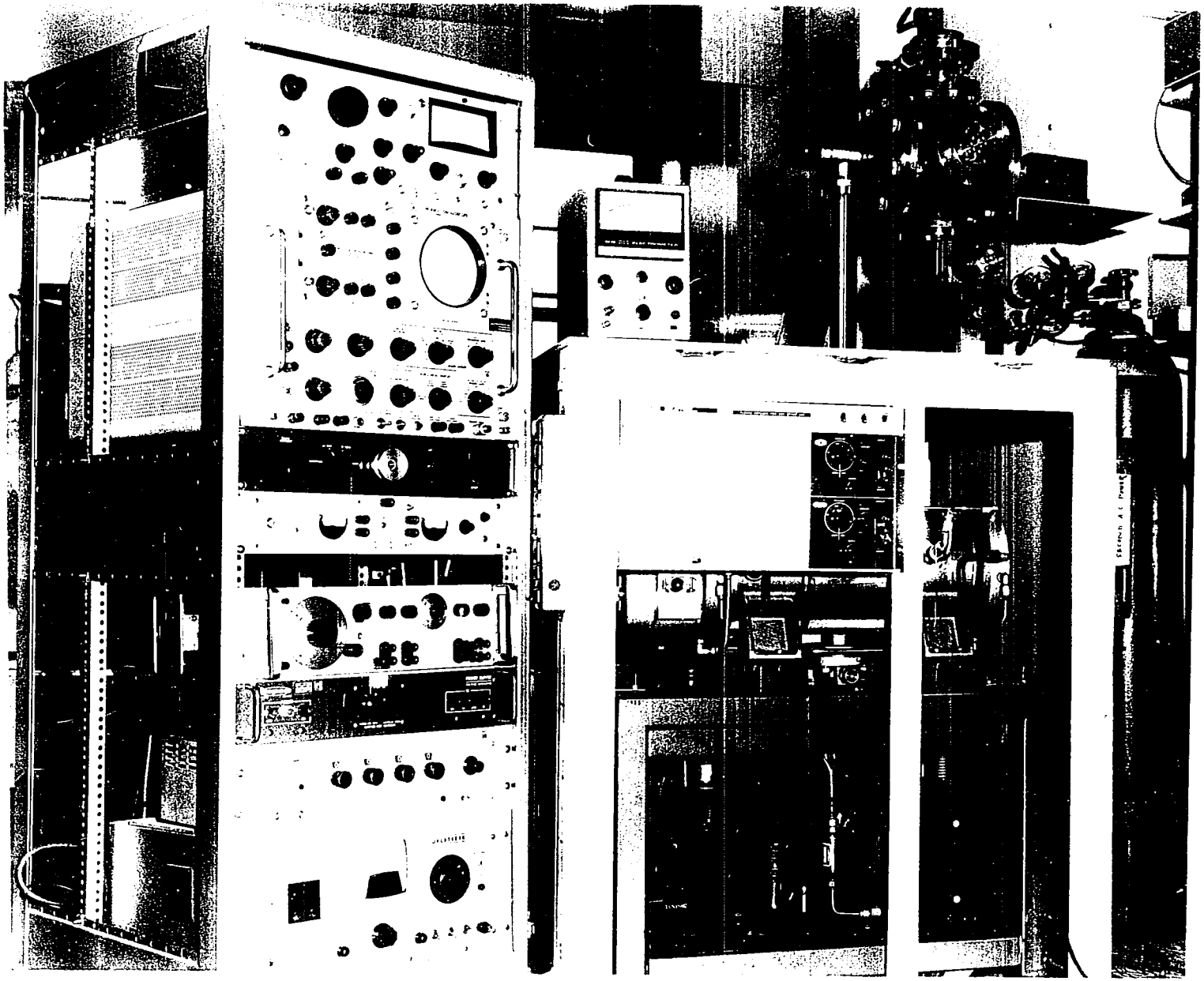

CHAPTER 5. RESULTS AND DISCUSSIONS

In Chapter 4, the experimental techniques of appearance potential spectroscopy were discussed and a description of the basic apparatus and all the subsequent improvements were given. In this chapter, the results of the experiments are presented in chronological order, and the salient features of the appearance potential spectra of various specimens are examined.

The appearance potential spectra of Beryllium, Boron, Carbon, Nitrogen and Oxygen were obtained, when present in trace amounts as constituent elements or as surface contamination. As the primary objective of this project was the detection of light elements, only a few heavier elements were examined. Iron and Nickel were studied in some detail because of their well known oxidation properties. A few materials tested gave no discernible signal. Barium was detected accidentally, as a contaminant from an oxide coated filament. An alloy of Nickel and Iron was examined to reveal the effect of alloying on the appearance potential spectra of the constituents. Considerable anomalous structure from some specimens has been observed.

The following notation is used in explaining the graphs:

I_s specimen current

v_m modulation voltage

τ time constant of the phase sensitive detector

f_m modulation frequency

p residual pressure

The X axis represents the electron beam energy, uncorrected

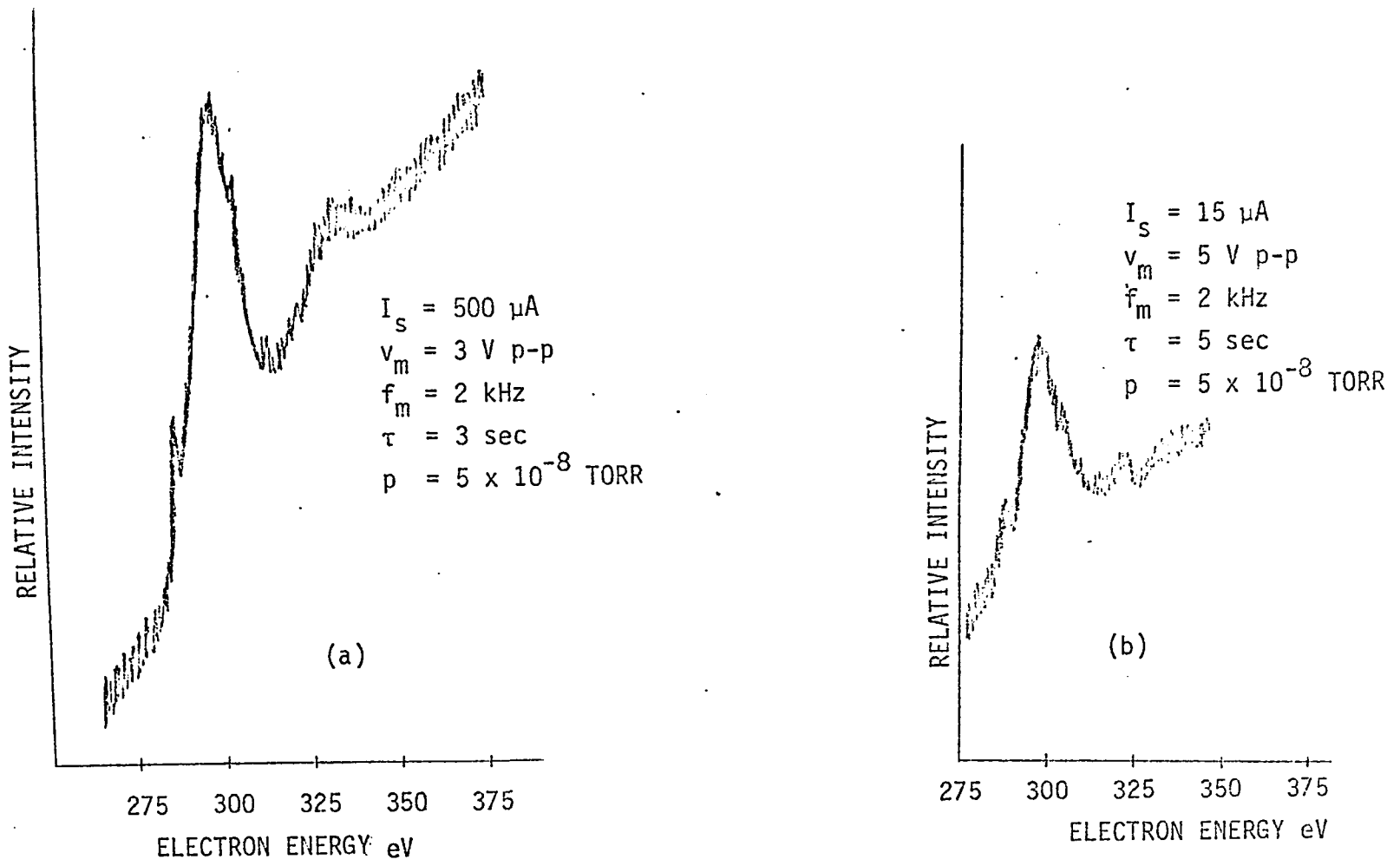

Fig. 5.1 Appearance Potential Spectrum of Carbon at Low Currents Obtained Using a Photomultiplier

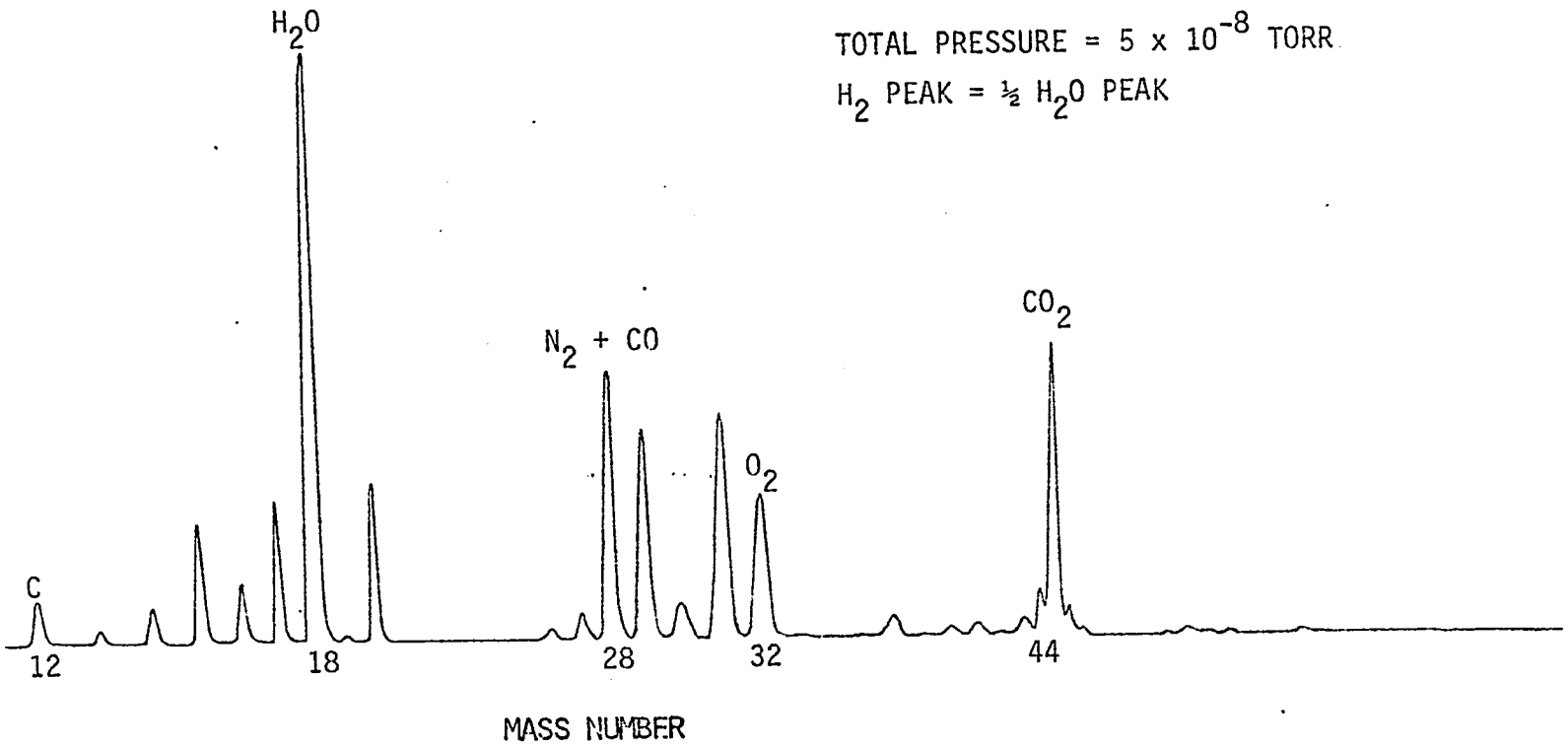

Fig. 5.2 The Mass Spectra of Residual Gases in the First Vacuum System

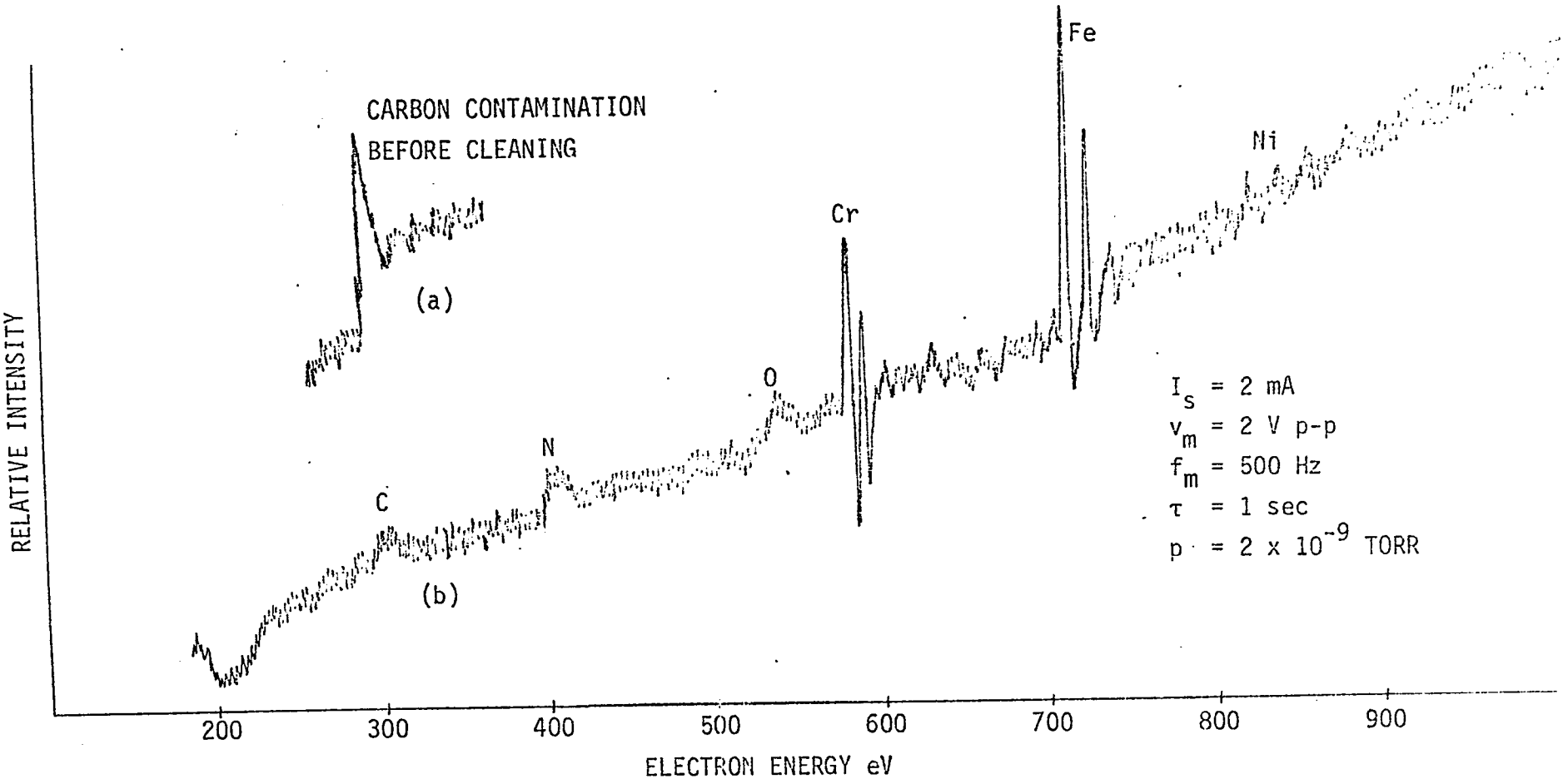

Fig. 5.3 Appearance Potential Spectrum of #304 Stainless Steel (a) Carbon Contamination Before Cleaning (b) Complete Spectrum After Argon Bombardment

for the work function of the filament and the thermal energy of electrons. The work function correction to be added to the electron energy is 4.5 eV for a Tungsten filament and 1.5 eV for an oxide coated filament. The Y axis represents the relative intensity of the first derivative of the total photoelectron yield, as obtained from the phase sensitive detector. For the cases in which the overall gain is known, the Y axis is scaled in terms of the rms value of the fundamental component of the photoelectron yield. The absorption edges of elements compiled from various sources, are tabulated in the appendix.

5.1 Results

Fig. 5.1 shows the results of the experiments with low incident electron currents and a photomultiplier detector. The appearance potential spectrum of Carbon taken at different values of electron currents exhibits a peak at 286 eV, followed by a larger peak occurring at about 296 eV. The shot noise contributed by the photomultiplier is evident, and this masks the less prominent peaks that occur at higher energies. The lowest current at which a reasonable signal was obtained was 15 μA, which suggests the feasibility of using a focused beam, several microns in diameter, without exceeding safe values of current densities at the specimen. The maximum current at which a spectrum was obtained using this set up was 500 μA, as the photomultiplier was approaching saturation at higher currents, because of the large background signal.

The residual pressure measured was 5×10^{-8} torr, with significant amounts of hydrocarbons indicated by mass peaks occurring

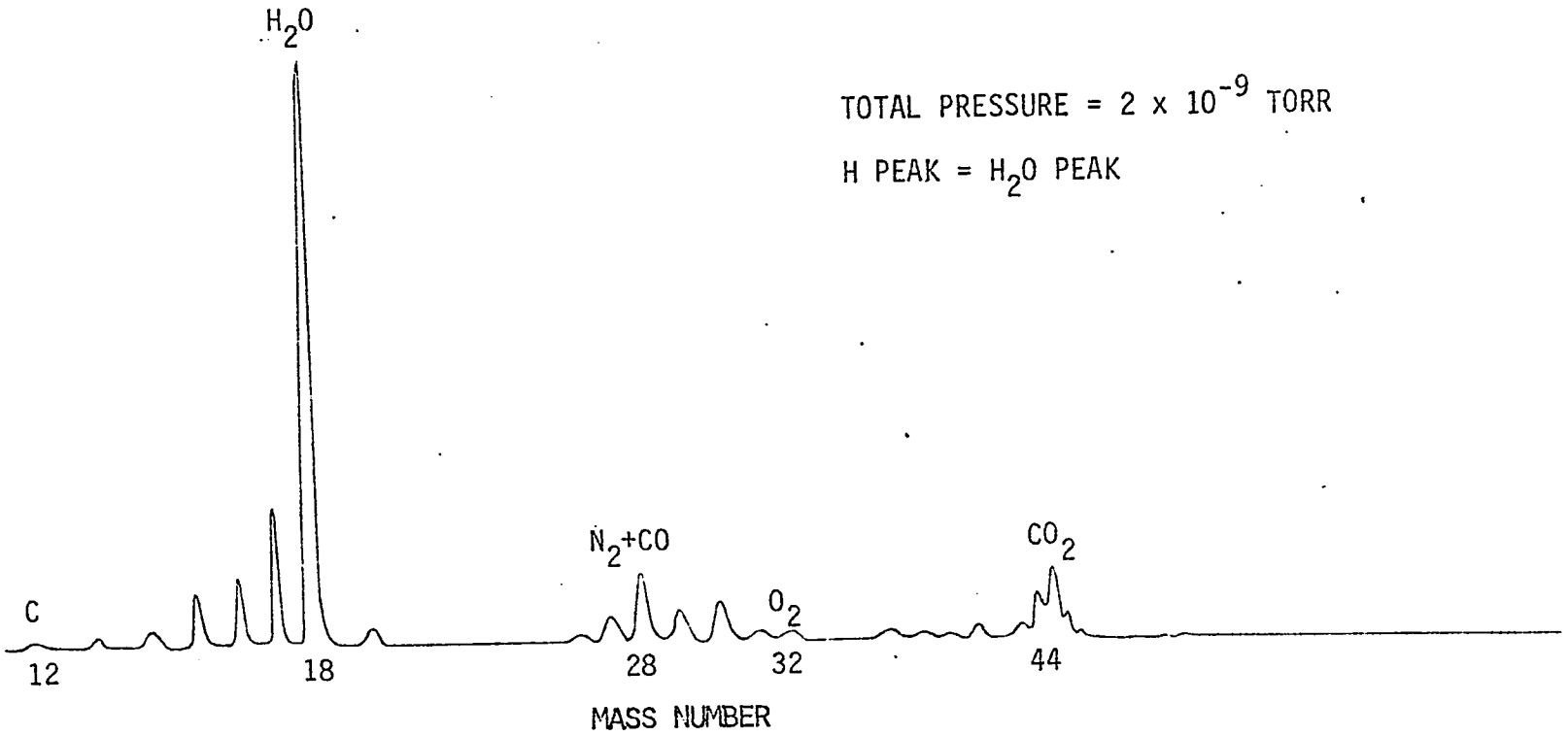

Fig. 5.4 The Mass Spectra of Residual Gases in the Improved Vacuum System

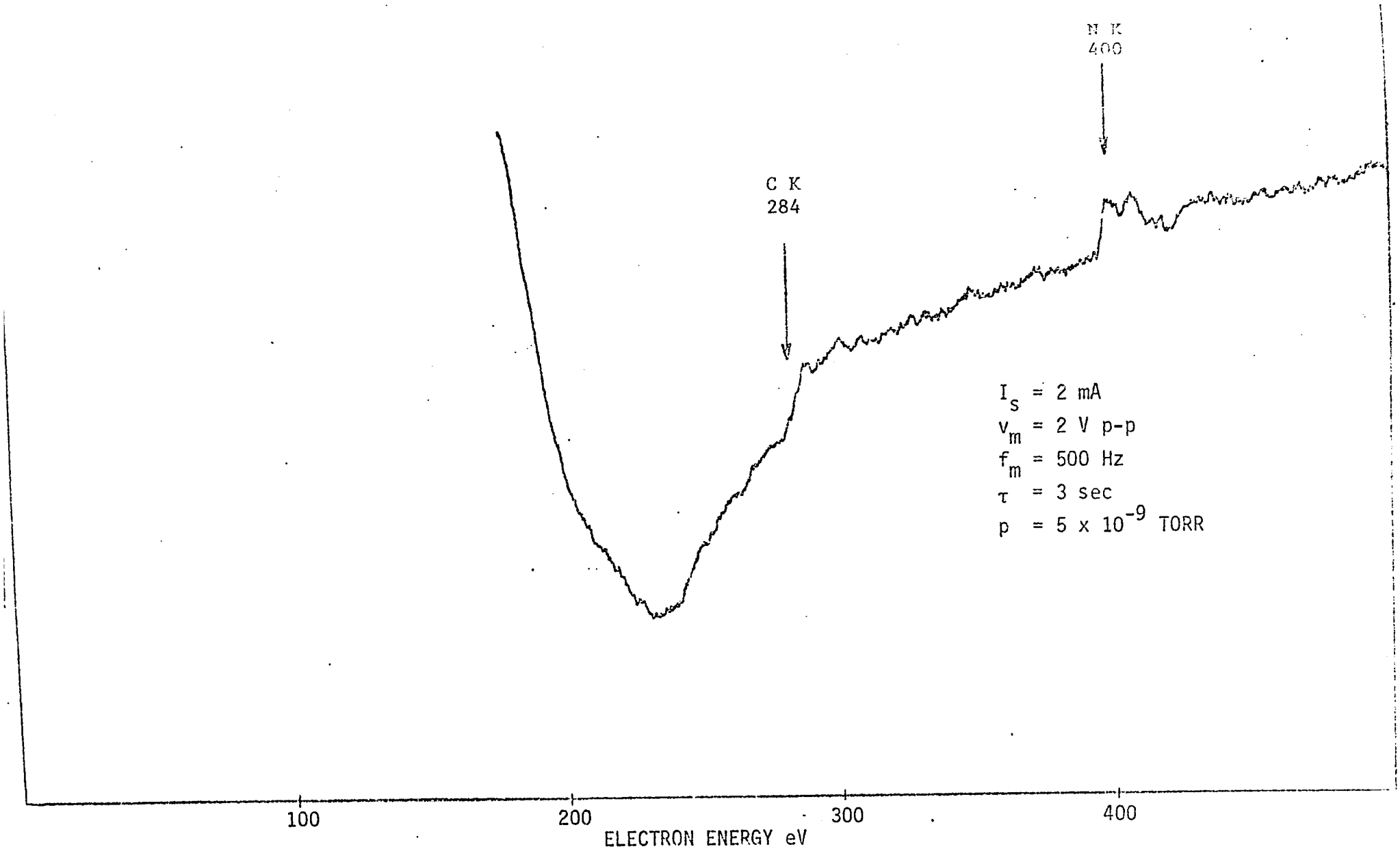

Fig. 5.5 The Expanded Spectrum of #304 Stainless Steel in the Energy Range 0 to 500 eV

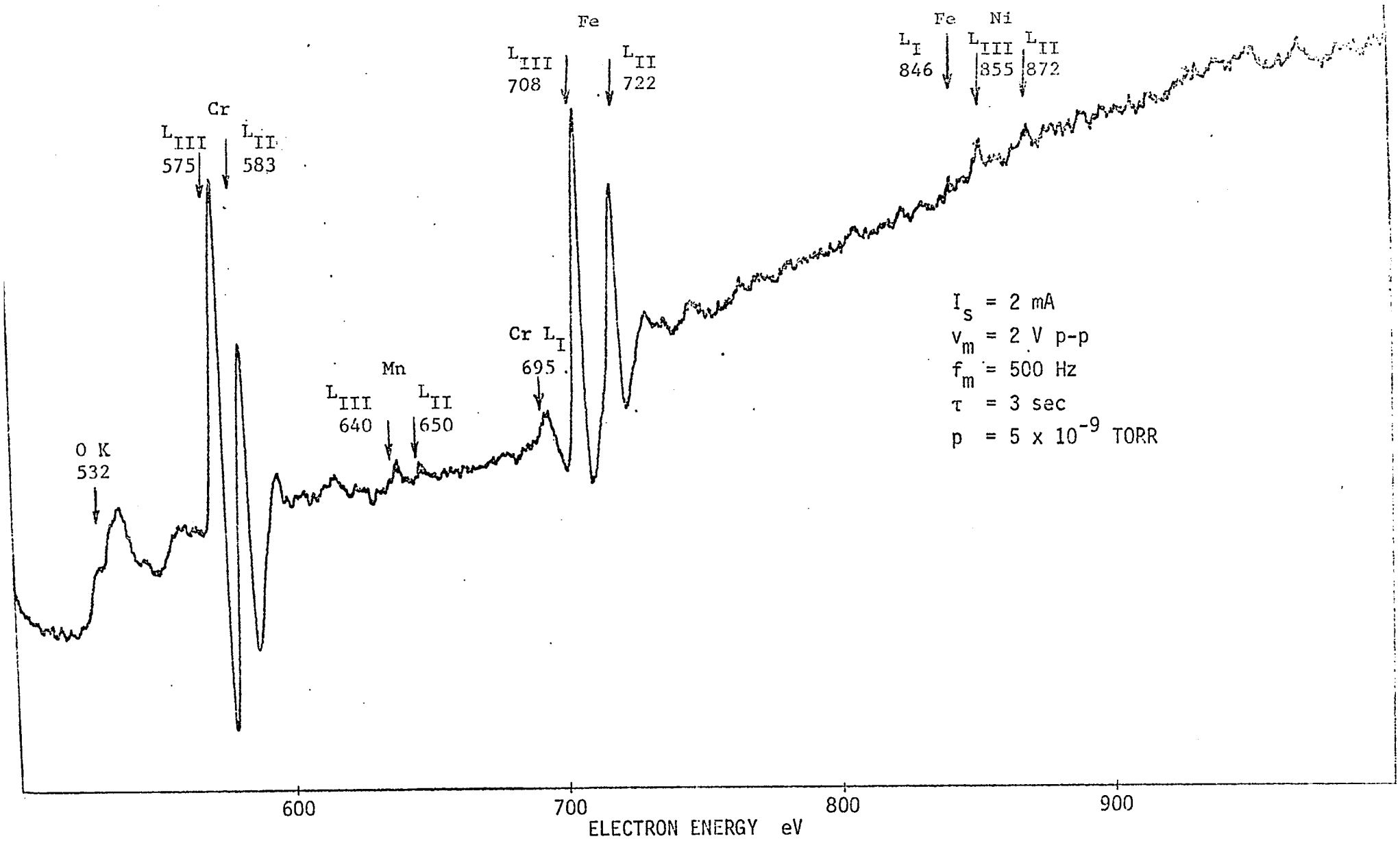

Fig. 5.6 The Expanded Spectrum of #304 Stainless Steel in the Energy Range 500 to 1000 eV

at 12, 15, 20 etc., as shown in Fig. 5.2. Because of the Carbon contamination resulting from the residual hydrocarbons, attempts to get the appearance potential spectra of other elements were not successful.

After improvements in the vacuum system were made and the scintillator-photomultiplier was replaced by a simple electron collector and electrometer amplifier, the first specimen tested was 304 stainless steel. As shown in Fig. 5.3, the appearance potential spectrum showed mostly Carbon before cleaning the surface. The specimen was then bombarded by Argon ions at 800 eV at a total current of 1 mA for 15 min at an Argon pressure of about 10^{-2} torr. It can be seen from the figure that the Carbon peak has fallen considerably (probably to a level corresponding to its concentration in the bulk), while the signals from the other constituents of stainless steel have become prominent. The mass spectra of the residual vacuum is given in Fig. 5.4. After surface cleaning, there was practically no increase in the Carbon signal over several hours of operation. The expanded spectra of stainless steel in the two ranges, 0 - 500 and 500 - 1000 eV (Figs 5.5 and 5.6) show all the constituents of stainless steel and also Nitrogen which may have been adsorbed on the surface, and Oxygen which may have been in the form of an oxide.

Fig. 5.7 shows the expanded spectrum of Carbon contamination initially present on the stainless steel specimen. A number of well defined peaks are seen to occur, in addition to the first one which lies just above the absorption edge of 284 eV. These

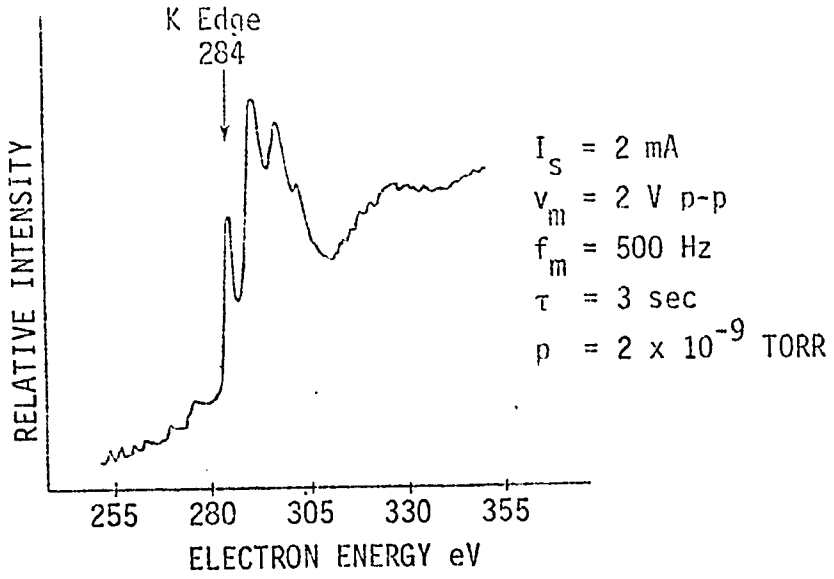

Fig. 5.7 The Expanded Spectrum of Carbon Contamination on Stainless Steel Before Surface Cleaning

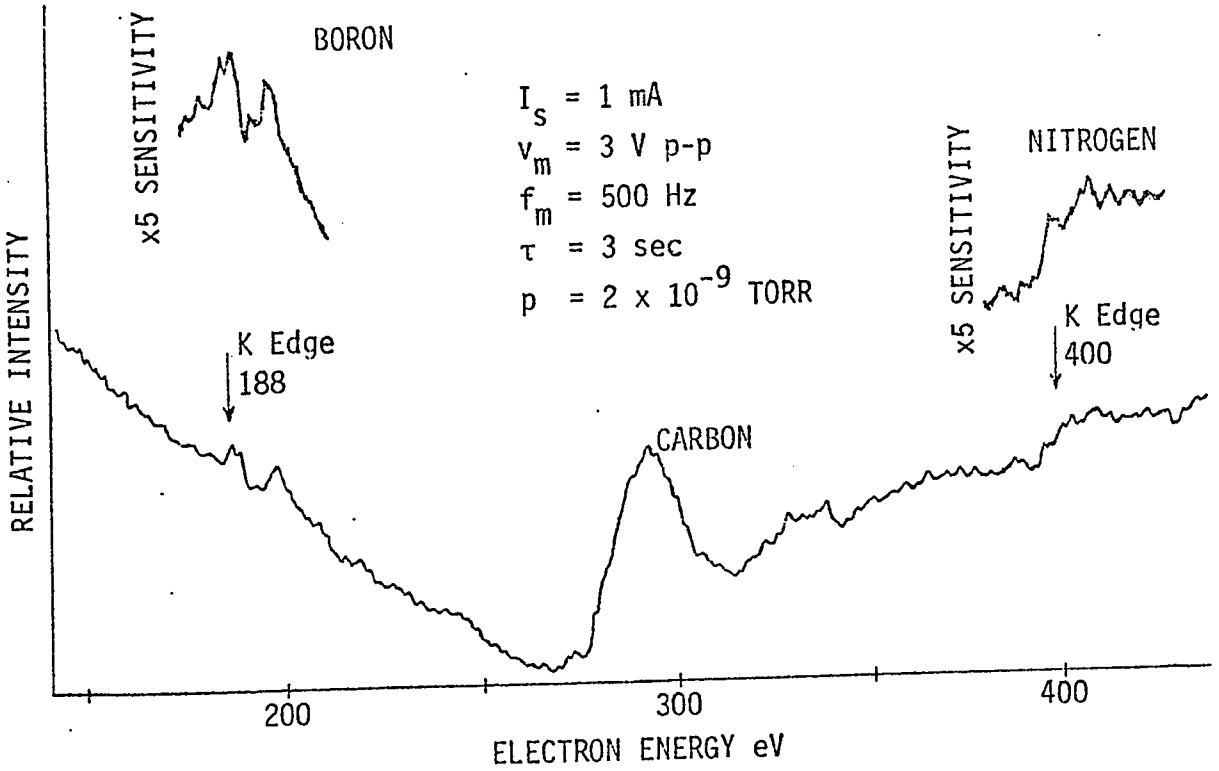

Fig. 5.8 Traces of Boron Nitride Detected on a Copper Beryllium Specimen Before Surface Cleaning

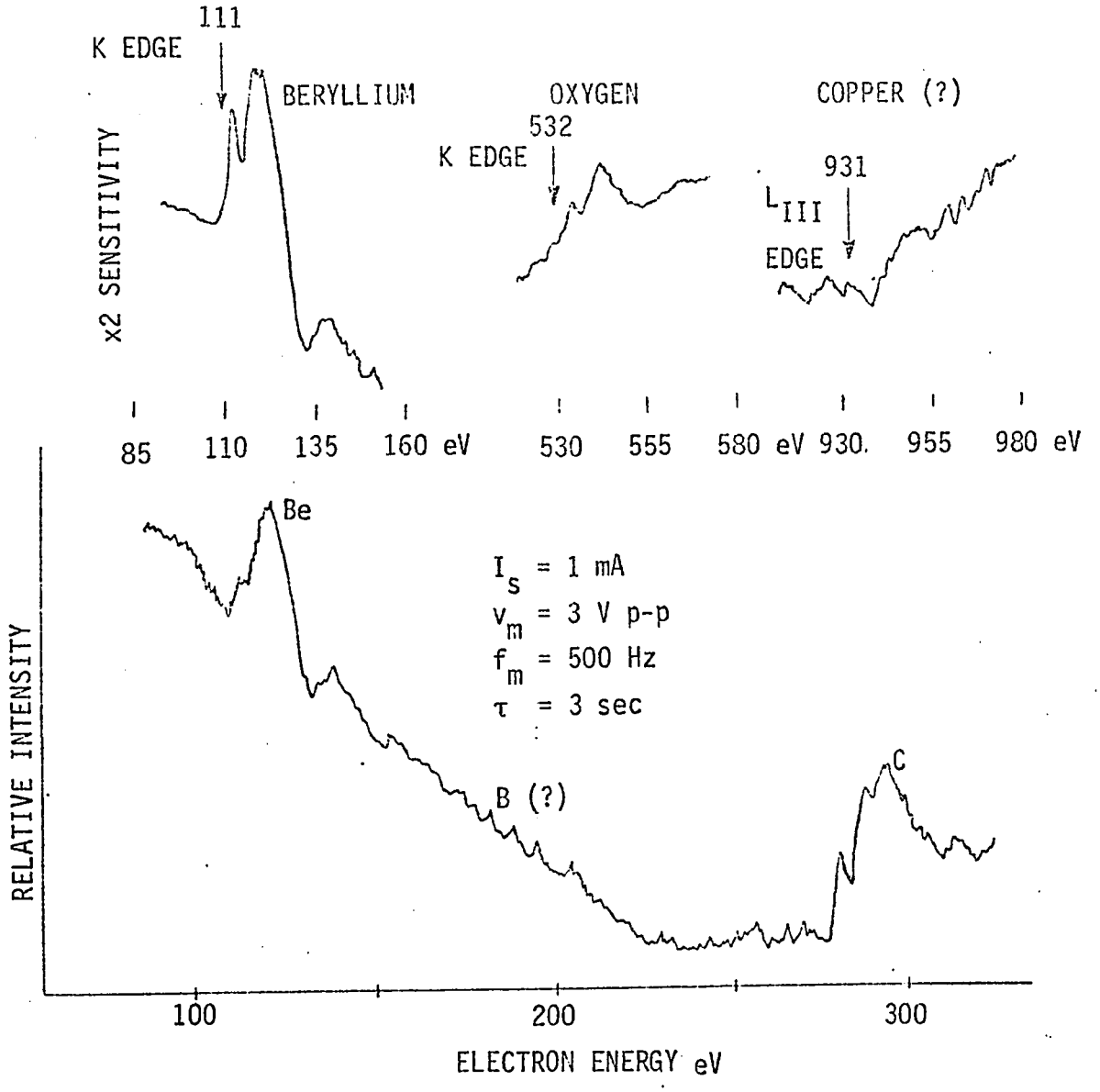

Fig. 5.9 Beryllium, Oxygen and Copper(?) detected from a Beryllium-Copper Specimen

multiple peaks occurring at a spacing of about 7 eV, are believed to be due to plasmon effects[59]. The relative heights of these peaks depend on the crystalline structure of the Carbon layer, which is known to vary considerably from sample to sample.

Attempts to obtain the appearance potential spectrum of Boron Nitride failed at first because of its high resistivity. While cleaning a Beryllium Copper specimen and the freshly machined Boron Nitride insulator together in Methanol, some fine particles of Boron Nitride were accidentally deposited on the specimen surface, when the solvent evaporated. The appearance potential spectrum of this sample before cleaning by ion bombardment, showed weak signals from Boron and Nitrogen (Fig. 5.8). This appears to be an effective technique for examining insulating specimens available in powder form.

After Argon bombardment, the Boron and Nitrogen peaks disappeared and the Carbon peak reduced considerably, but Beryllium and Oxygen were detected from the same specimen (Fig. 5.9), which suggested the presence of a layer of Beryllium Oxide covering the surface. Further Argon bombardment was done to remove the oxide layer and detect Copper, which is the major constituent (98%) in the alloy. However, close to the L_{III} and L_{II} edges of Copper, there was no reproducible structure above the noise fluctuations, as shown in the figure. The small change in slope evident in the spectrum in this energy region is attributed to Copper. This observation supports the explanation presented in sec. 3.2 that, as Copper has a full 3d band and the partially filled 4s band does not have fluctu-

Fig. 5.10 Detection of Small Amounts (≃10 Å) of Oxygen on Nickel

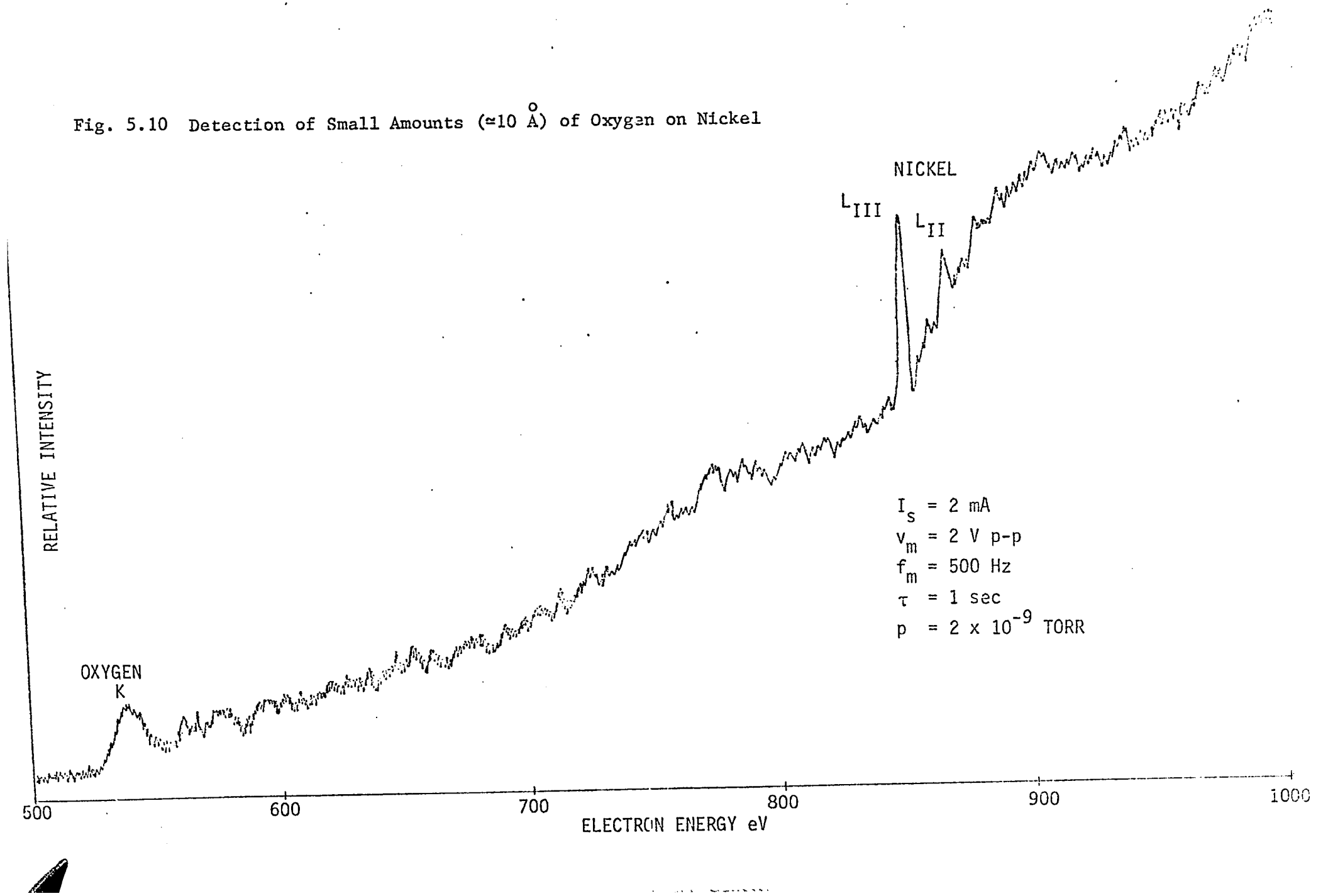

ations in the density of states, the appearance potential spectrum of Copper would not exhibit any marked structure. It can therefore be assumed that the detection sensitivity of Copper in appearance potential spectroscopy is very poor.

Nickel was chosen as the next specimen because it was already detected as a constituent element in stainless steel, and has known oxidation properties. For example, it has been established by oxidation studies[60] that pure Nickel exposed to air for a few minutes or more at room temperature, develops a stable surface layer of oxide having a mean thickness of 10 Å. The specimen was prepared by depositing a layer of Nickel on to a stainless steel substrate, by evaporation from a pure Nickel pellet in a Tungsten boat, using a standard evaporator. It was briefly exposed to air during transfer from the evaporator to the specimen holder, taking care not to touch the surface or to contaminate it by solvents.

After pump down and baking, the appearance potential spectrum obtained showed Nickel peaks, a weak but distinct Oxygen peak and trace amounts of Carbon contamination (Fig. 5.10). The height of the Oxygen peak gives a quantitative measure of the detection sensitivity of Oxygen. In view of the Oxygen signal being the contribution from only a few monolayers (10 Å) on the surface, the sensitivity may be considered good.

5.1.1 Oxidation Studies on Iron[60]

Using the modified specimen holder with heating and temperature measuring facilities, it was possible to perform controlled

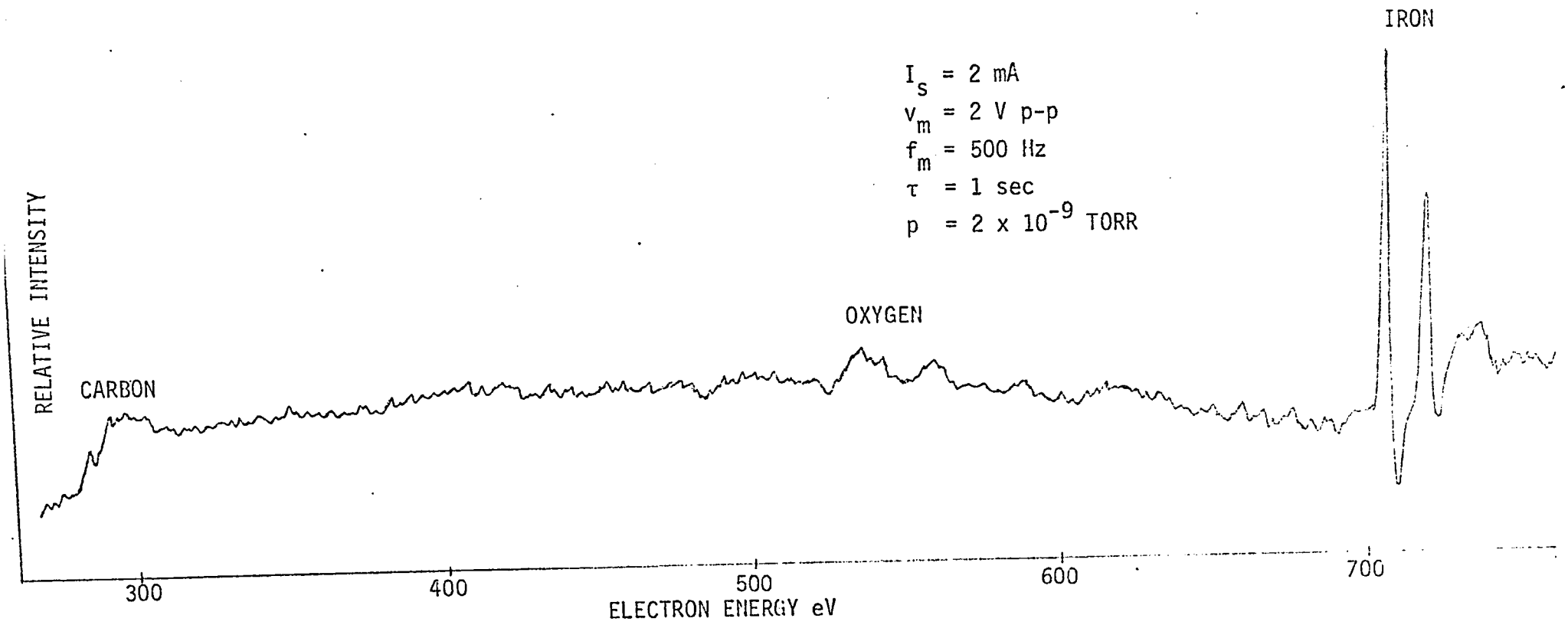

Fig. 5.11 The Spectrum Obtained from a High Purity Iron foil Before Surface Treatments, showing Small Amounts of Carbon and Oxygen

oxidation and reduction of specimens by admitting pure Oxygen and Hydrogen respectively to the chamber, and heating the specimen to known temperatures. A series of tests as detailed below were performed on an Iron sample to demonstrate the capability of appearance potential spectroscopy to distinguish between different valence states of Iron atoms.

High purity Iron foil (99.99% Iron and a few parts per million Carbon), 0.001" thick and having a 0.003" Iron Constantan thermocouple attached to its back (Fig. 4.10), formed the specimen. The appearance potential spectrum showed very small amounts of Carbon and Oxygen, in addition to Iron (Fig. 5.11). On heating the foil to about 500° C for several minutes in vacuo and then cooling it down to room temperature, the Oxygen peak fell below the point of detectability. This suggests the chemical reaction of Carbon and Oxygen on the surface to form Carbon monoxide, the Carbon from the bulk diffusing to the surface during heating. To remove the remaining Carbon, the specimen was exposed to pure Oxygen at about 1 torr at room temperature and heated again after pumping down to 10^{-8} torr. By repeating this process a few times, most of the Carbon was burned off, leaving only a small quantity of Oxygen, which was then removed by heating to 300° C in Hydrogen at 10^{-3} torr. This is a standard technique for removing the Carbon from the bulk of thin specimens and cleaning the surface of Oxygen.

The expanded spectrum of clean Iron after the above treatments is shown in Fig. 5.12a. Oxygen was then admitted at 1 torr for 10 min at a specimen temperature of 200° C, to form a layer of Fe_3O_4

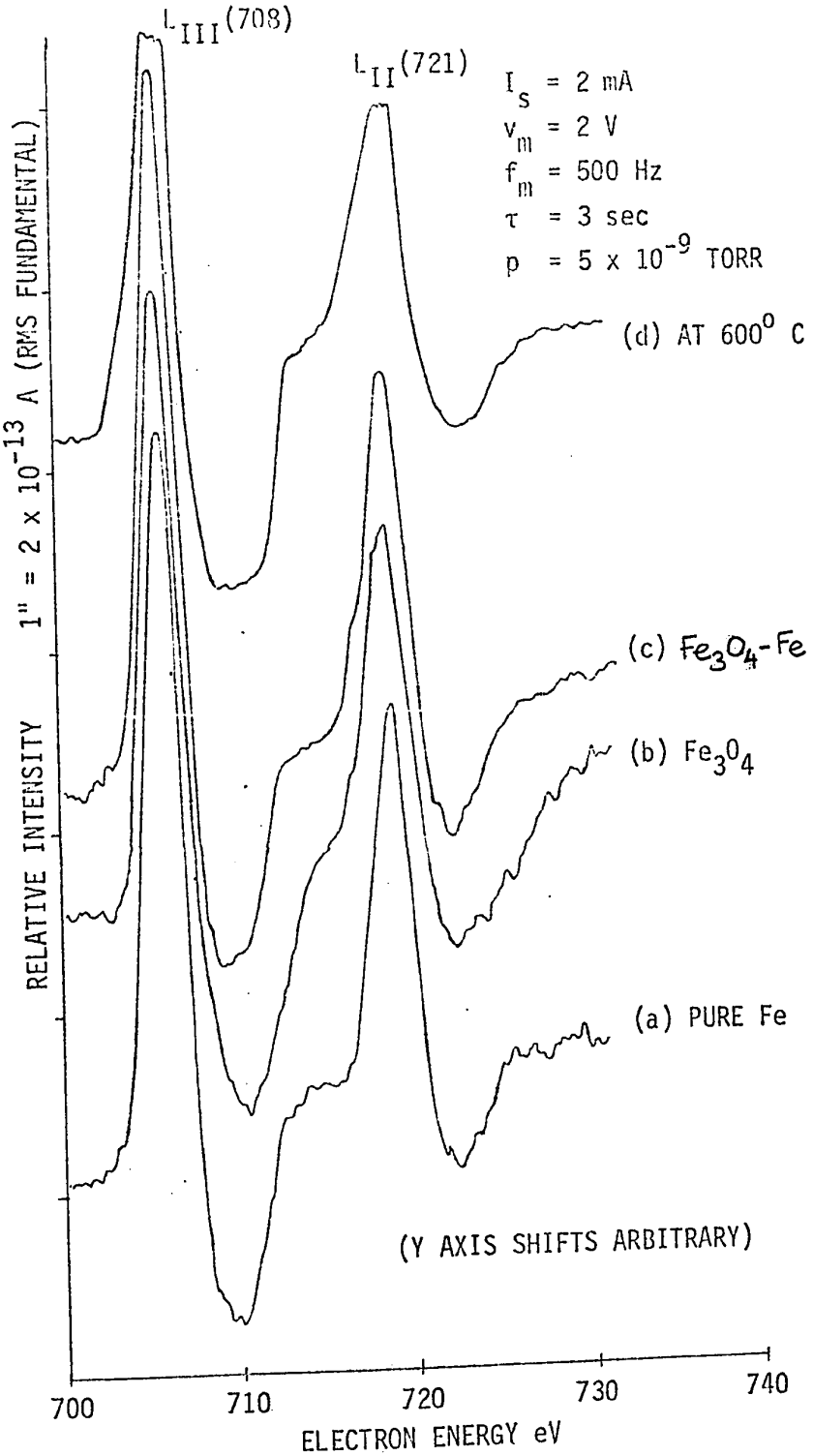

Fig. 5.12 Variations in the Iron Spectrum as a result of Oxidation

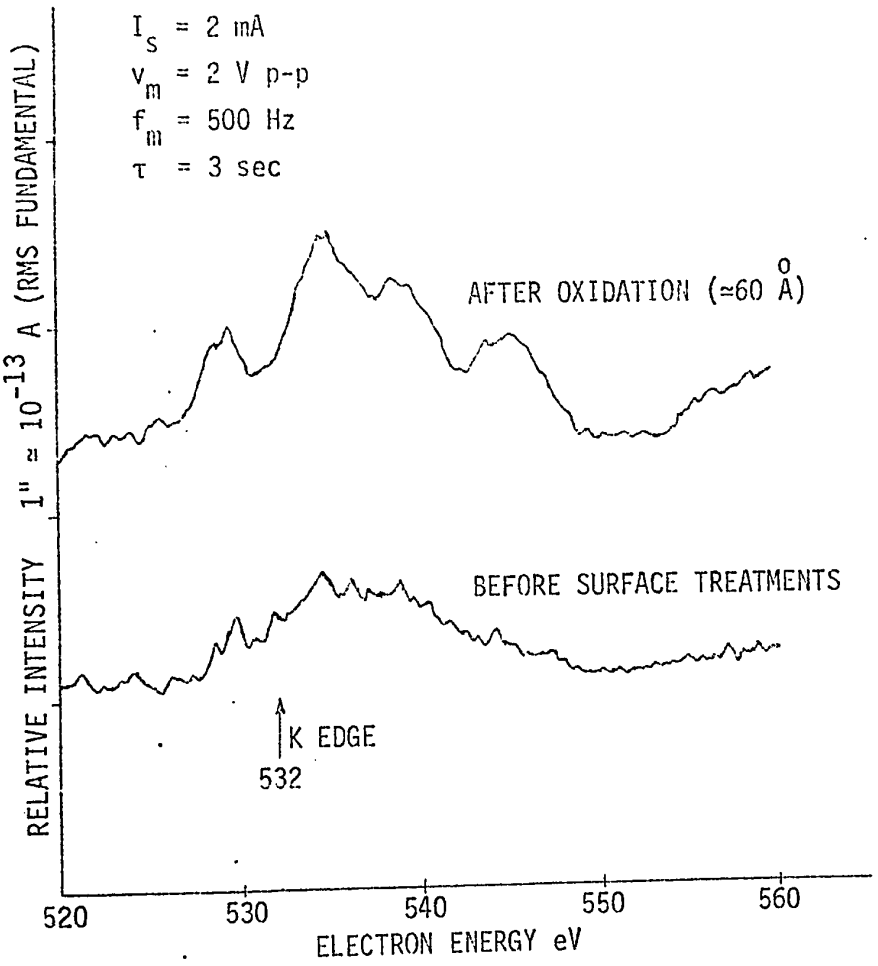

Fig. 5.12 (e) The Oxygen Spectrum obtained from the Iron Sample

of about 60 Å. The appearance potential spectrum of Iron in this form is shown shown at (b). The sample was then heated to 600° C to change the form of the oxide from Fe_3O_4 to ~~Fe_2O_3~~ Fe_3O_4-Fe. The Iron spectrum was obtained while the specimen was hot and also after it cooled down to room temperature, as shown at (d) and (c) respectively.

In all the above spectra of the Iron, the positions of the L_{III} and L_{II} peaks show now significant shift in energy, within the resolution of the instrument (about 2 eV). However, there are noticeable differences in the heights of the peaks and their shapes. These changes are attributed to the different valence states of Iron atoms. If the differences in the spectra can be properly characterized, this technique will provide a simple but powerful means to distinguish between various valence states of elements. The flattening of the peaks while the specimen is hot, as shown at (d), is perhaps due to the partial loss of structure in the density of empty states in the valence band.

Fig. 5.12eshows the expanded spectrum of Oxygen from the Iron specimen, before treatments and after oxidation to form a 60 Å layer of oxide. The spectrum for the latter case shows small peaks occurring at a spacing of about 5 eV, resembling plasmon peaks observed in the Carbon spectrum (Fig. 5.7). Plasmon data on Oxygen is not available at present to verify this presumption.

5.1.2 Experiments with an Oxide Coated Filament.

In all the experiments described above, the best energy resolution attainable was limited by the drop across the filament, which was

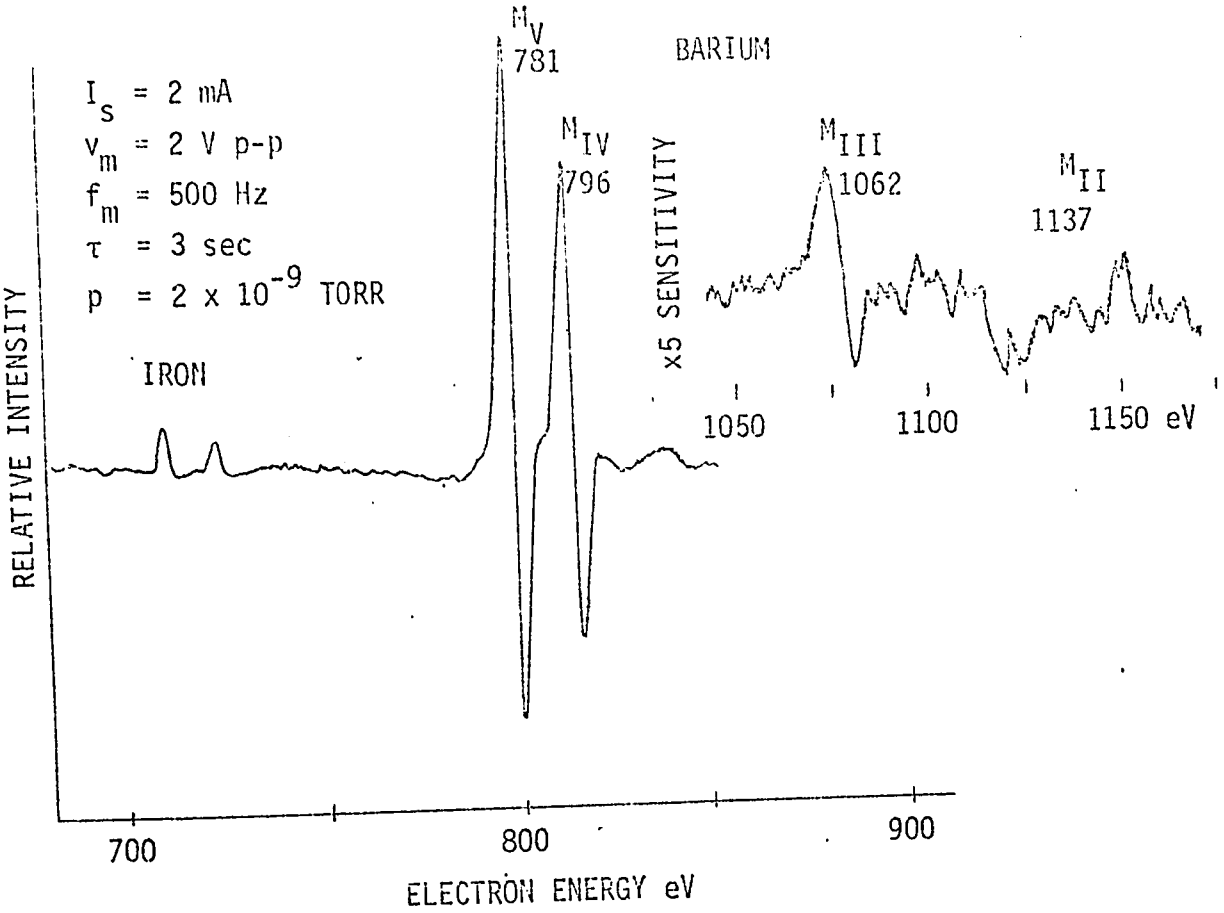

Fig. 5.13 The Spectrum obtained from an Iron Specimen contaminated by Barium from an Oxide Coated Filament

about 2 V. Another problem with Tungsten filaments was the high heat radiation at the temperature of 2800° K, which resulted in the raising of the temperature of thin specimens to about 200° C. The Tungsten filament was therefore replaced by an oxide coated filament from a type 5Y3 tube.

The operating temperature of oxide coated filament being only about 900° K, it was possible to obtain the required emission with a filament current of 3 A and a voltage drop of 0.75 V. However, in order to start the emission, the current had to be raised to 3.5 A for a few seconds, to remove any contamination that occurred during the exposure to air while transferring the filament from the sealed tube to the vacuum system.

The appearance potential spectrum of the Iron sample taken with the oxide coated filament as the electron source, is shown in Fig. 5.13. The Iron peaks have diminished and there are strong peaks which could only have come from Barium evaporated from the filament on to the specimen surface. Other possible constituents such as Strontium and Calcium in commercial oxide coated filaments, were not evident from the appearance potential spectrum of the specimen. The specimen was then heated to about 1000° C in an effort to clean the surface. At first the Barium peaks decreased and the Iron peaks increased. Further heating resulted in the reduction of the Iron peaks to a quarter of the Barium peaks (Fig. 5.15).

The above results suggest the formation of a strong chemical compound between Iron and Barium on the surface, giving rise to several noticeable effects. The Iron spectrum does not exhibit marked negative excursions, which for Iron in the pure and oxidized forms are

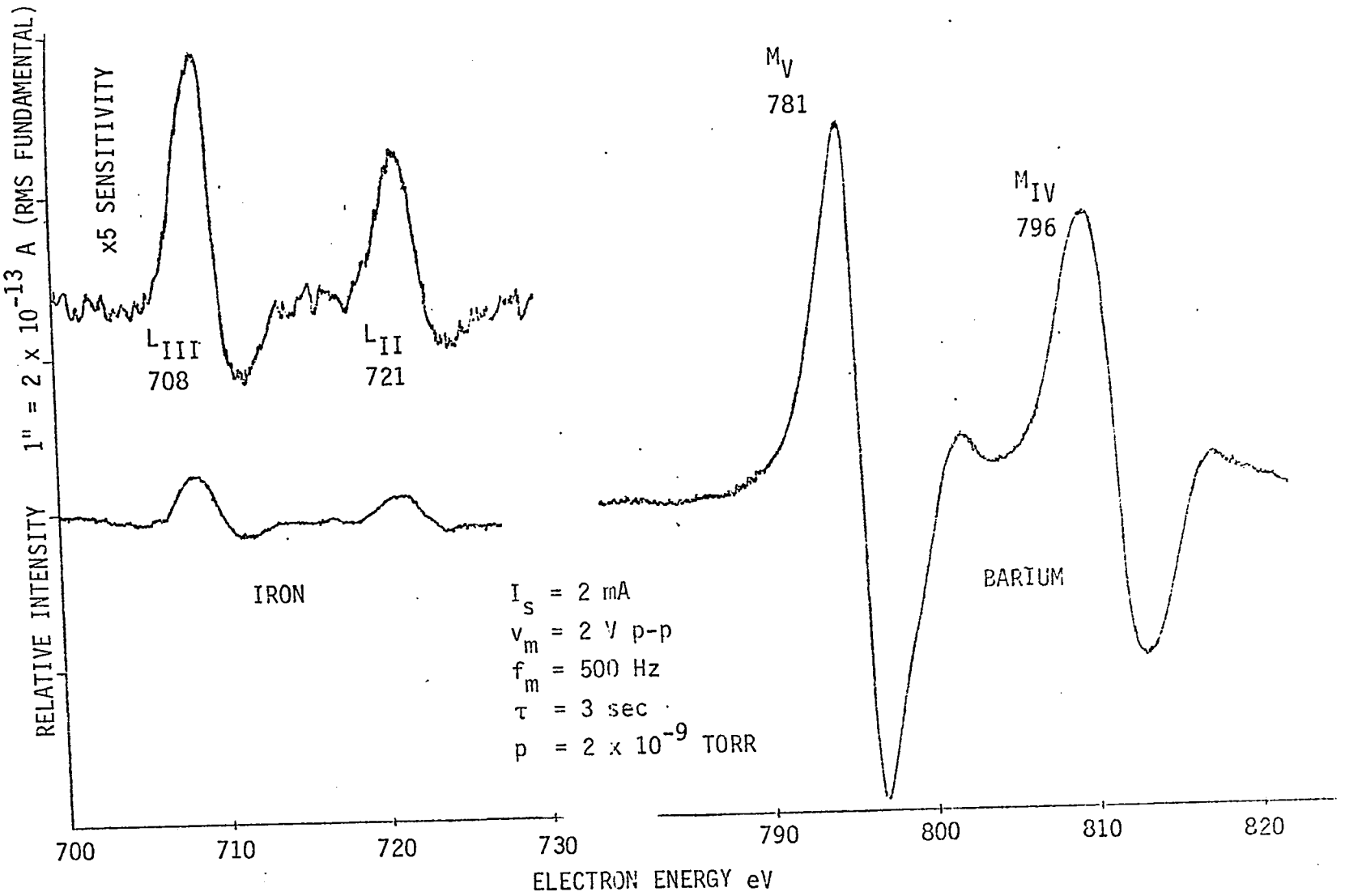

Fig. 5.14 The Expanded Spectra of Iron and Barium before heating

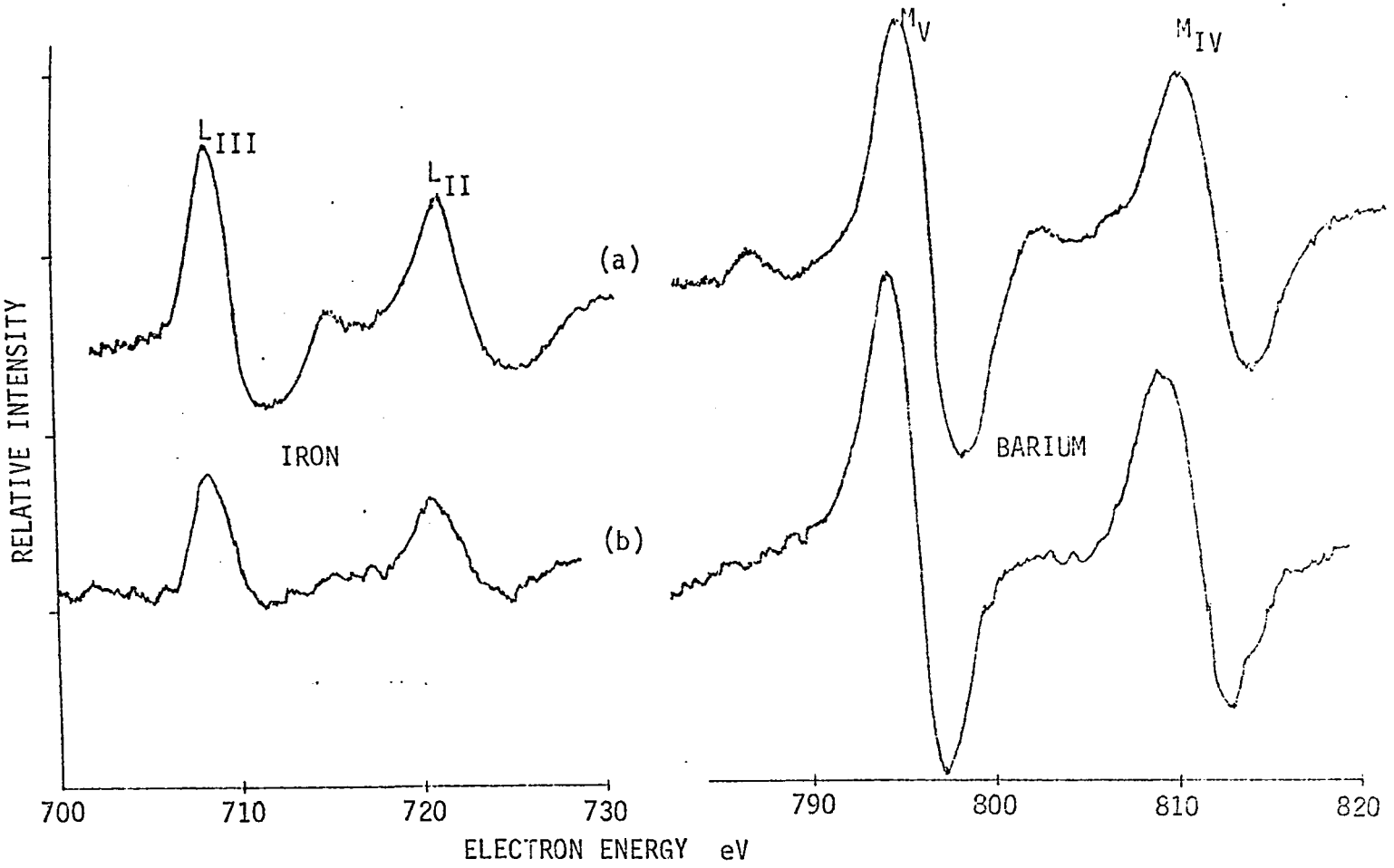

Fig. 5.15 The effect of heating on the Barium Contaminated Iron Specimen
(a) After heating once (b) After prolonged heating

quite pronounced (compare Figs. 5.14 and 15 with Fig. 5.12). The shift in the Iron peaks by about 3 eV compared to the previous results, is because the work function of the oxide coated filament is only 1.5 eV, whereas for the Tungsten filament, it is 4.5 eV. However, the Barium peaks have a shift of about 7 eV with respect to the tabulated values of their absorption edges, even after the correction for the filament work function is applied. This is perhaps the result of chemical shifts which have been observed in the soft x-ray emission spectra of many compounds[61].

From the above results, it is clear that the oxide coated filament, once exposed to air, cannot be used in the apparatus for the analysis of specimen surfaces. It was suggested[62] that the contamination of the filament is perhaps the result of the formation of a hydroxide under the action of moisture in air, and this can be avoided by transferring the filament in a dry Nitrogen environment. It is believed that a clean oxide coated filament normally operates below the temperature at which the constituents start evaporating. However, even when the filament is transferred under a controlled environment, it needs activation by momentarily raising the temperature to a high value, during which time the specimen will have to be protected from contamination by a shutter actuated in vacuum.

From the point of view of contamination, a pure Tungsten filament is the best choice, because it does not need to be activated, and has negligible rate of evaporation at the operating temperature. The potential across the emitting region of the filament can be reduced to less than a volt by etching the centre of the filament by

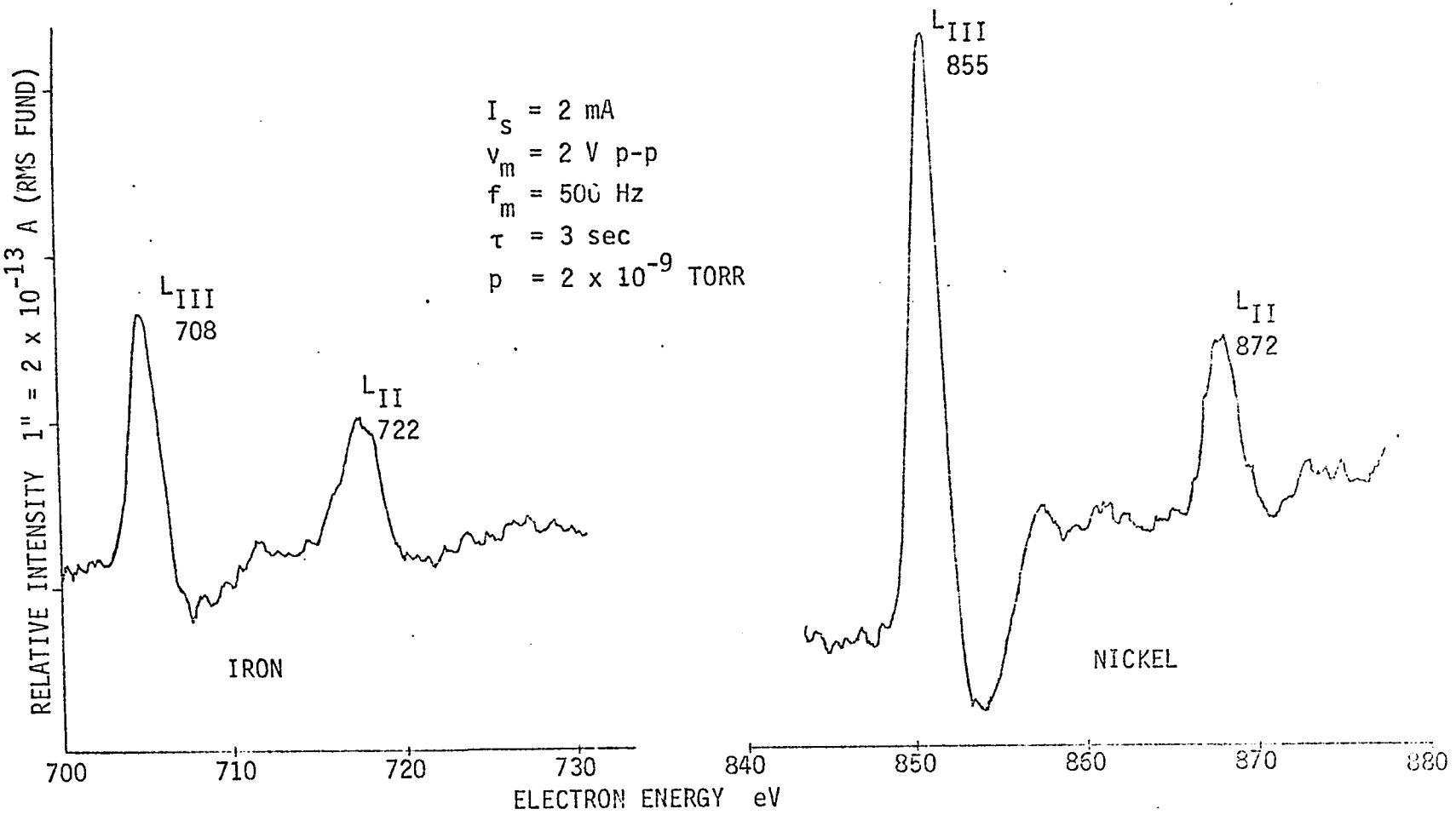

Fig. 5.16 Iron and Nickel Spectra obtained from a Magnetic Shielding Alloy containing about 20% Iron, 80% Nickel and small quantities of Molybdenum

hydrolysis, and thus confining the emission to a small fraction of its total length.

After replacing the oxide coated filament by a Tungsten filament, a magnetic shielding alloy of Nickel (≃80%) and Iron (≃20%) was examined as the specimen, to determine if alloying has any effect on the appearance potential spectra of the constituents. The spectrum given in Fig. 5.16 shows no shift in the position of the Nickel and Iron peaks (compared to the values from Fig. 5.10 and 12) in energy, but there is an enhancement of the negative peaks in Nickel and a corresponding diminution of the negative peaks in Iron. This indicates changes in the valence band structure of the elements, as a result of alloying.

The alloy also contains small quantities (<2%) of Molybdenum; but none of the absorption edges of Molybdenum could be discerned in the spectrum.

5.2 Anomalous Features

Several anomalous features have been found in the appearance potential spectra of different elements. The spectra obtained from disc specimens in the earlier experiments, show a steep rise in the signal below 200 eV (Figs. 5.5, 8 and 9), unlike the spectra from thin specimens (Figs. 5.17 and 18). The latter on the contrary, show considerable structure in the low energy region, some peaks sharp and others broad. In Figs. 5.17 and 18, none of the peaks corresponds to any known absorption edges, except for the Iron M peak that occurs around 55 eV. Similarly, the high energy spectra of Fig. 5.19 obtained from the Nickel Iron alloy, with purpose of lo-

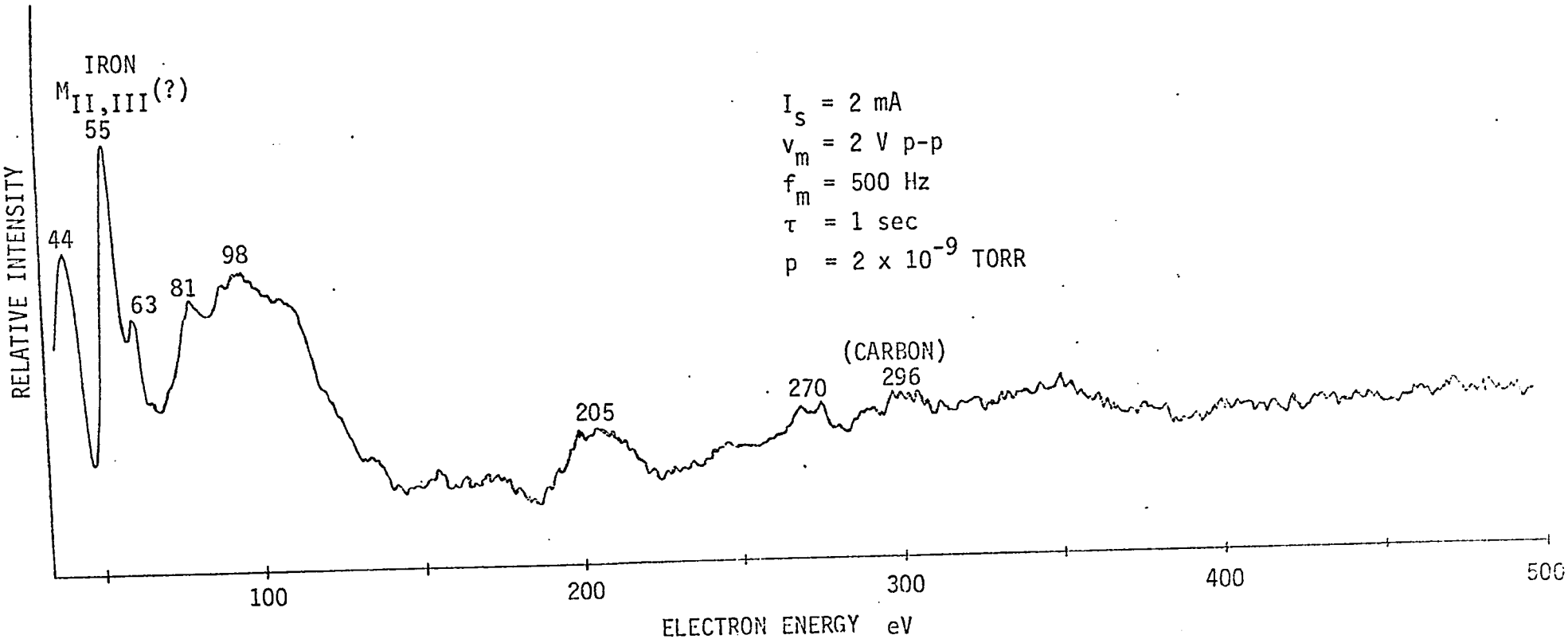

Fig. 5.17 Anomalous Low Energy Structure obtained from a Pure Iron Specimen. The numbers denote the approximate location of the peaks

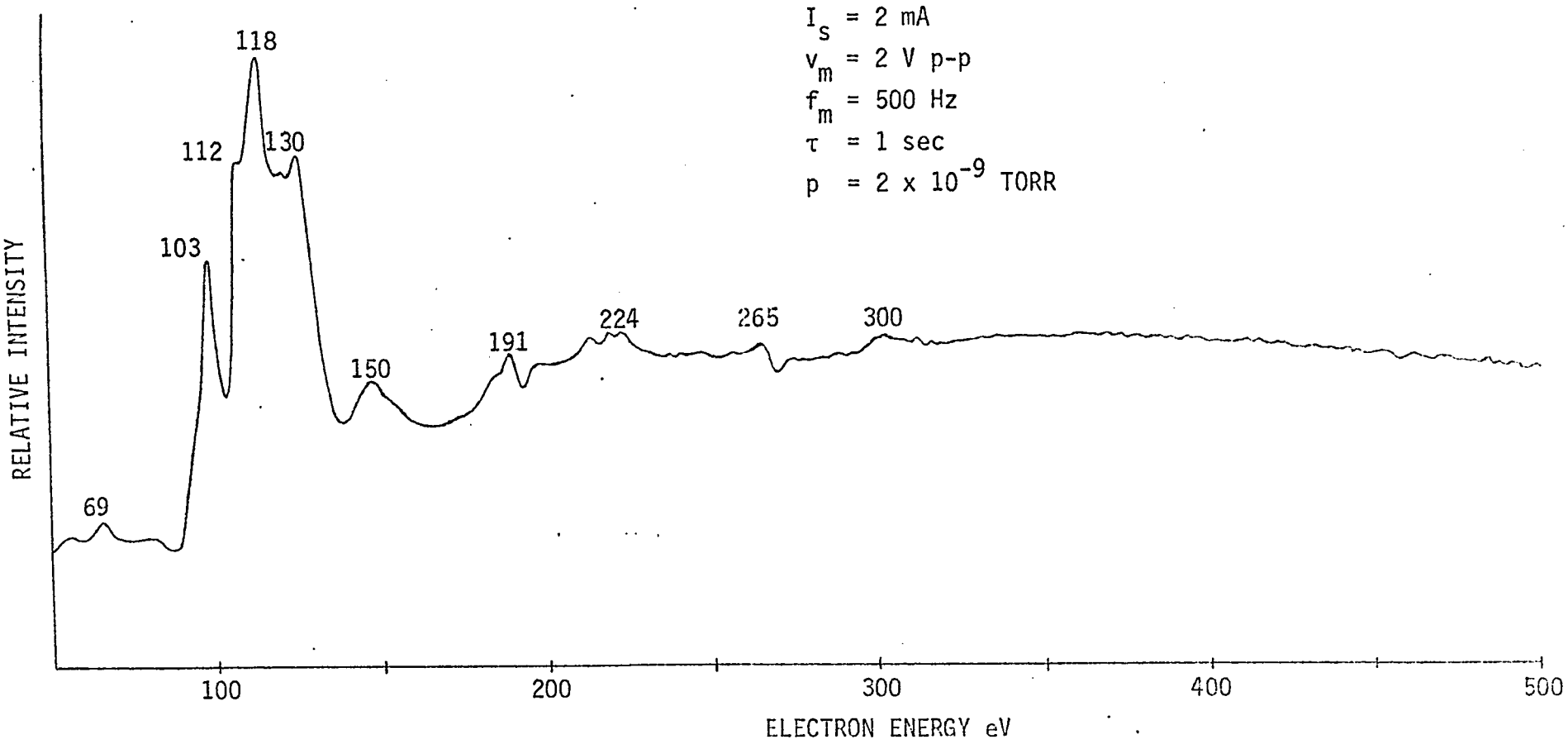

Fig. 5.18 Anomalous Low Energy Structure obtained from a Barium contaminated Iron Specimen. The numbers denote the approximate location of the peaks

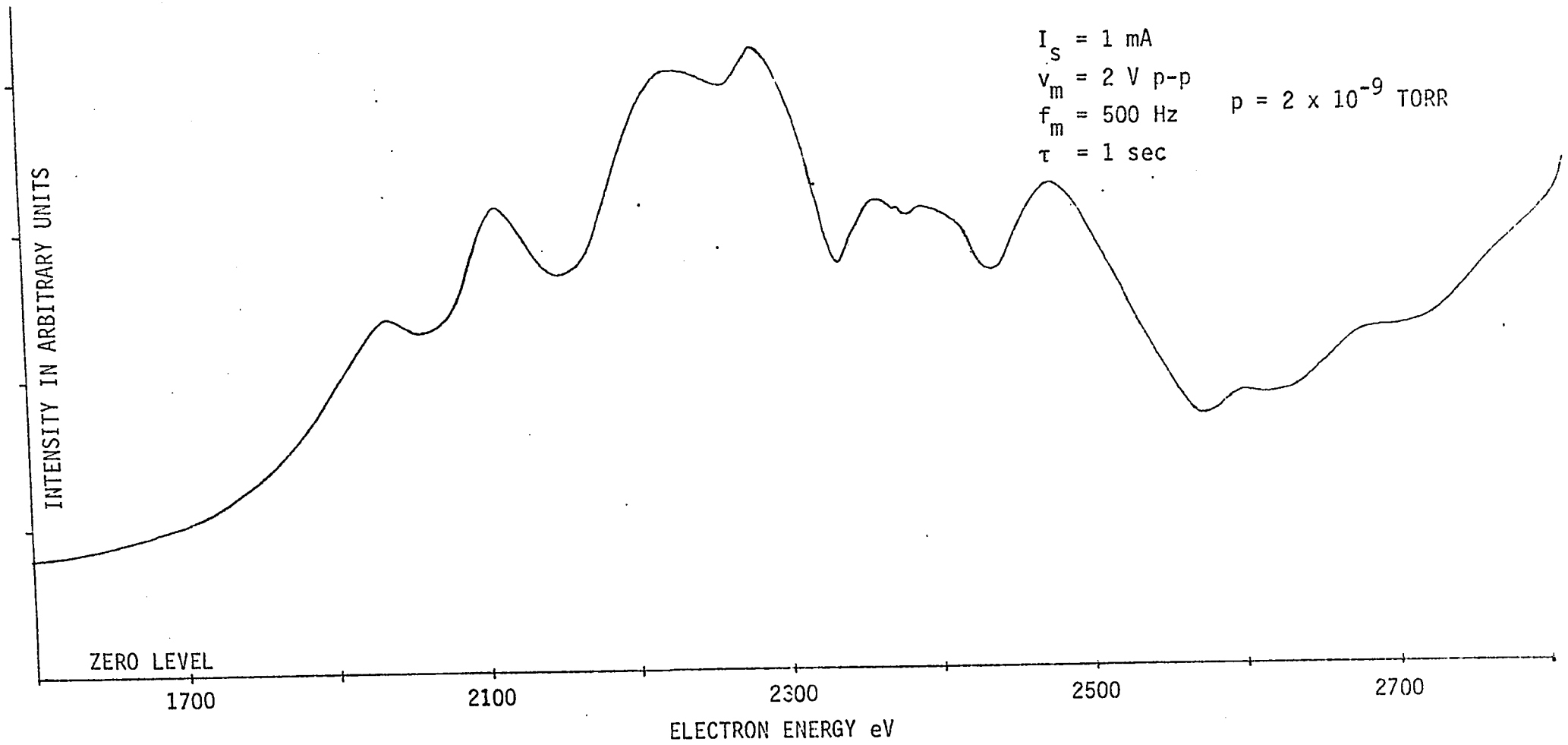

Fig. 5.19 Anomalous High Energy Structure obtained from an Iron-Nickel Alloy. The zero level corresponds to the output with no modulation

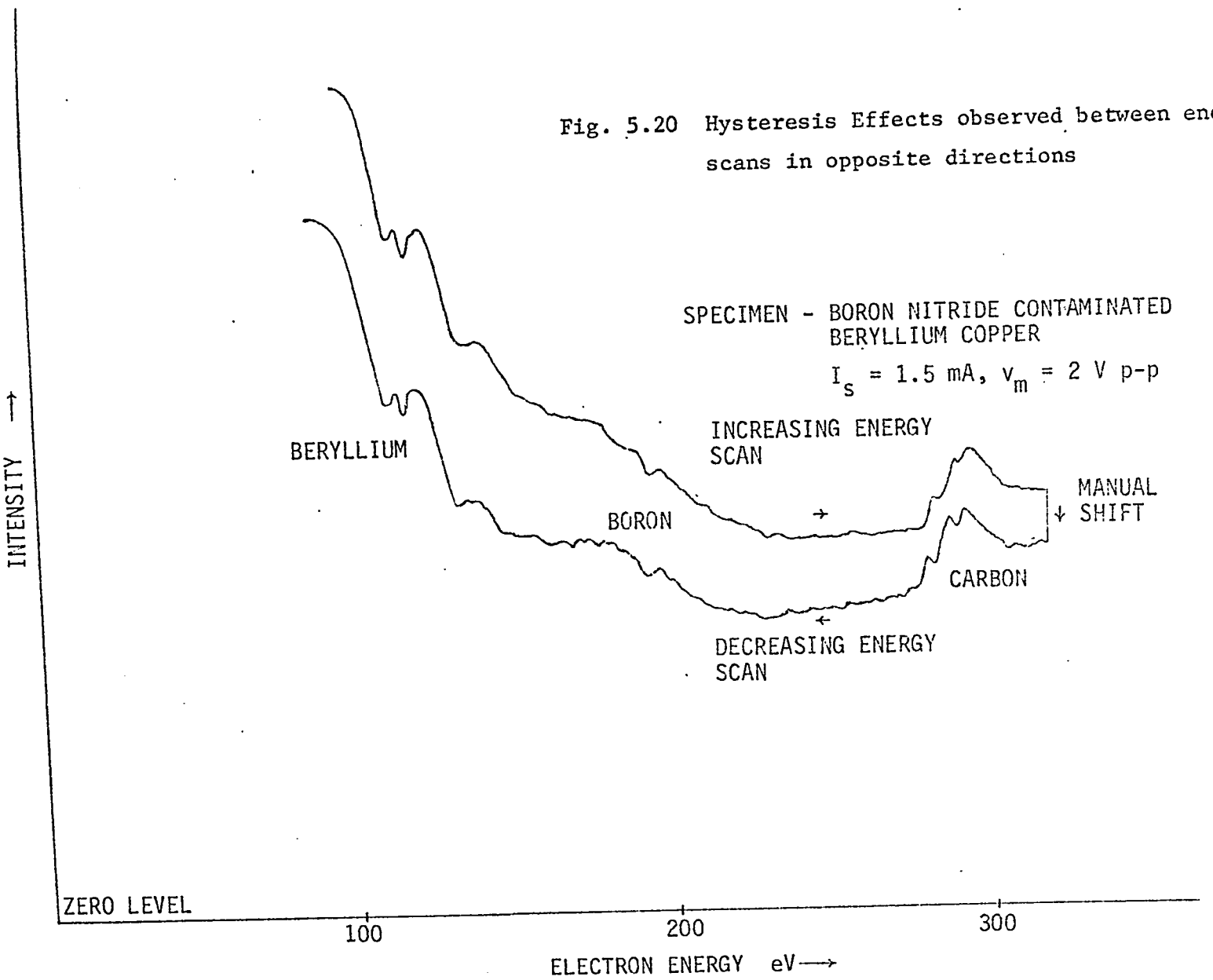

Fig. 5.20 Hysteresis Effects observed between energy scans in opposite directions

cating the Molybdenum L edges, show broad structure which does not correspond to any absorption edges.

It is presumed that the anomalous structure observed is associated with the crystalline structure of the specimen, and the energy dependence of bremsstrahlung from the material[63]. At first it was suspected that the anomalous structure might have been due to ions, and therefore, an extra grid biased positive, was added in front of the detector in order to stop any stray ions from entering it. There was a consequent reduction in the signal level, but the structure was unchanged.

With thin samples, the temperature measured during the experiment was found to rise to 100 to 200^{o} C, whereas for thick specimens there was much more conduction of heat to keep the surface relatively cool. This may be one of the factors causing the difference in the spectra between thin and thick specimens.

Another effect noticed with thick specimens is the divergence between the traces for increasing and decreasing energies. The former was always found to lie above the latter, the separation increasing with the decrease in energy, as shown in Fig. 5.20. This may partly be due to the hysteresis in the temperature changes during energy scans. More work needs to be done in order to explain these anomalous effects satisfactorily.

5.3 Contemporary Work in Appearance Potential Spectroscopy

During the past year, the newly established technique of appearance potential spectroscopy has attracted the attention of physicists, chemists and technologists alike. A number of experiments

have been done by various groups in the recent months, illustrating the different facets of appearance potential spectroscopy and demonstrating its unique capabilities in the field of material analysis. In this section, a summary of the contemporary works (most of them yet to be published) done in appearance potential spectroscopy is presented.

Redhead and Richardson[64] have examined Thorium by appearance potential spectroscopy. The Thorium specimen was formed as a film evaporated in situ on a substrate by evaporation from a Thoriated filament. Several O and N edges were detected in the spectrum, and after oxidation of the film, new satellite peaks were observed.

Thomas Dooley[65] showed how a standard LEED display apparatus could be modified to obtain the appearance potential spectra of the target material. Determination of the crystal structure from diffraction experiments under identical conditions in such an apparatus would greatly aid the capabilities of appearance potential spectroscopy in surface studies.

Houston and Park[66] measured the L_3/L_2 peak intensity ratio in the appearance potential spectrum of Chromium and compared it with the expected statistical weighting ratio of 2, based on the total Auger yield. They postulate that the measured ratio would provide a sensitive test for models of the electronic structure of surface atoms.

Park, Houston and Shreiner[67] studied the Chromium depletion of vacuum annealed stainless steel surfaces by appearance potential spectroscopy. A multiple sample consisting of Chromium,

Iron, Nickel and 304 stainless steel was used in the experiment so that the constituent elements could be examined under the same conditions as the stainless steel specimen to determine the surface composition. The results of the experiment suggest that the susceptibility of vacuum annealed stainless steel to corrosion is due to the depletion of Chromium concentration on the surface.

A direct comparison of Auger electron spectroscopy with appearance potential spectroscopy was made by Musket[68]. By combining a cylindrical mirror electron energy analyzer and a large solid angle windowless photon detector into one system, he was able to obtain the two spectra under identical conditions. The results from a stainless steel specimen show that the detection sensitivity of the two methods are considerably different for the same element, and that the information obtained by the two methods is complementary. It was also apparent that, whereas Auger electron spectroscopy is, in general, more sensitive for elemental analysis, appearance potential spectroscopy is better suited for the study of chemical binding states of surface atoms.

Houston and Park[69] studied the effect of alloying Titanium and Nickel on the band structure of these transition elements, by appearance potential spectroscopy. They were able to obtain alloys of different concentrations by evaporating one metal onto another in situ, and demonstrate chemical shifts as a result of alloying.

Another study comparing with Auger Electron Spectroscopy was made by Tracy[46]. From the results, he concludes that the detection sensitivity of elements in appearance potential spectroscopy varies

from being almost as good as, to considerably worse than that of Auger electron spectroscopy. Certain elements have shown complete insensitivity to appearance potential spectroscopy. However, the appearance potential spectrum could reveal surface effects not easily detectable by other methods.

Houston and Park[70] showed the effect of Oxygen on the appearance potential spectra of the 3d transition elements, Titanium, Chromium and Nickel. Accurate determination of the binding energies of these metals reveals measurable shifts due to oxidation. The Oxygen spectrum in Nickel oxide shows complex multipeak structure, attributed to plasmon effects. In another experiment[71], they examined the oxide and hydride of Titanium in detail and observed chemical shifts in the appearance potential spectra.

In a recent experiment, Park and Houston[72] obtained the L appearance potential spectra of all the 3d transition elements, Scandium, Titanium, Vanadium, Chromium, Manganese, Iron, Cobalt and Nickel, under identical conditions by mounting pure specimens of these metals in a multiple holder in their apparatus. All the spectra exhibit variations that reflect the density distribution of the empty states in the valence band, caused by the overlapping 3d and 4s bands. The absolute binding energies measured are found to be lower than the tabulated values, apparently due to surface effects. The intensity ratios L_3/L_2 also show variations with atomic number, and the ratio approaches the statistical weighting of 2 only for the nearly empty and the nearly filled 3d band.

5.4 Suggestions for Future Work

At the present time, the detection sensitivity of appearance potential spectroscopy is unimpressive compared with that of other methods of microanalysis. Before the technique of appearance potential spectroscopy could be adapted to the standard electron microprobe, its sensitivity must be improved by 2 to 3 orders of magnitude.

In appearance potential spectroscopy, the wanted signal is small in comparison with the back ground noise. The signal to noise ratio could be improved greatly, using an energy sensitive detector, which would ideally select the characteristic radiation from the specimen.. Even a detector with a variable high pass characteristics would remove much of the back ground due to the bremsstrahlung.

The cut off frequency of such a high pass filter should be continuously varied as the incident energy is scanned, so that the detector would be sensitive to photons of energy close to the incident energy. This can be achieved in principle by the energy sensitive selection of photoelectrons released from the photocathode. The energy of the electrons released by a photon of energy E, will lie between 0 and $(E-\phi)$ eV, where ϕ is the work function of the cathode. If these electrons are retarded by a negatively biased grid maintained at a potential of $-(E-\phi-\Delta E)$, only those electrons released by photons of energy $(E-\Delta E)$ or more would reach the detector, where ΔE is the desired pass band of the system.

Though energy discrimination is achieved in this fashion, the loss of signal strength may be excessive. This is because only a very small fraction of the photoelectrons will have energies close to $(E-\phi)$, most of them having very low energies. As little is known about the energy distribution of photoelectrons from various cathodes, it is not feasible to estimate whether an overall improvement in the signal to noise ratio could be achieved by this technique.

Bremsstrahlung, which causes the major component of the background signal when the target is excited by electrons, is either very weak or not produced at all when the excitation is in the form of photons or ions. The appearance potential technique has already been successfully demonstrated[26] using x-ray excitation, obtained from a separate target excited by electrons of variable energy. Because of the practical impossibility of producing reasonably monochromatic x-rays whose mean energy can be varied as required, there is only a small advantage gained in the above case, for, a considerable part of the unfiltered primary radiation consisting of all energies up to a maximum, diffracted and scattered by the specimen, would still fall on the detector. In addition to this, x-rays, unlike electrons and ions, cannot be focused or deflected.

Ion excitation in appearance potential spectroscopy seems to be a promising possibility. The near absence of bremsstrahlung would greatly improve the signal to noise ratio and thus reduce the exciting currents needed to give a reasonable signal to microamperes, obtainable from a focused beam. This technique does not appear to have been tried in appearance potential spectroscopy so far. The

main problem associated with the ion excitation is the relatively high pressures (over 10^{-5} torr) required to produce ions. By using an inert gas like Neon or Argon, the contamination of the specimen due to the residual molecules can be avoided and the noise due to ions entering the detector can be minimized by interposing properly biased grids. An ultrahigh vacuum could still be maintained near the specimen, if need be, by passing the ions through a small aperture and pumping differentially.

Though focusing of heavy ions is not as easy as focusing electrons, ion guns capable of producing beams of a few microamperes confined to sub-millimetre sized spots have been made. Surface damage caused by the low energy probing beam of ions is not expected to be very severe. There is also the added facility of performing controlled etching of the surface merely by increasing the energy of the ions.

The principle of appearance potential spectroscopy can be extended to specimen current and back scattered electrons as well. At low energies, as Auger type transitions predominate over radiative transitions, considerable structure can be expected in the specimen current and the back scattered electrons, when the incident energy is scanned. Preliminary results obtained using the present apparatus showed complicated structure in the back scattered electron yield, which could not be explained. It is hoped that careful investigation of these phenomena would greatly add to the efficacy of appearance potential spectroscopy.

So far, appearance potential spectroscopic studies have been made only in the low energy ranges. There is no apparent

reason why the technique cannot be extended to energies as high as several keV. Because of the simplicity of the method, this facility can be easily added to any standard electron probe apparatus. As x-ray production is much more efficient at higher energies, it may be feasible to get reasonable signal to noise ratios even at low beam currents.

The occurrence of considerable anomalous structure in the appearance potential spectra at low and high energies needs to be investigated in detail. As postulated, if such a structure is related to the crystalline structure of the surface, it will prove to be an additional tool in surface studies. By modifying LEED apparatus for appearance potential spectroscopy, any possible relation between the crystal structure and the anomalous peaks observed can be established.

5.5 Conclusion

Appearance potential spectroscopy is a newly developing technique for the analysis of solid surfaces. The apparatus is simple, consisting of a source of electrons of variable energy and a total x-ray detector. By modulating the energy of the electrons striking the specimen and detecting the harmonic content of the emitted x-rays using phase sensitive detection techniques, the derivative of the x-ray yield is obtained. The derivative plotted against energy exhibits characteristic structure at the absorption edges of the constituent elements in the sample. Because of the use of low energy electrons (below 1000 eV), this is basically a tool for surface analysis. The K edges of light elements and the L, M

and the higher edges of heavier elements have been detected by this method. The shape of the appearance potential spectrum of an element is strongly dependent on the density distribution of empty states in the valence band and therefore is sensitive to the changes in the valence state of the element. The appearance potential studies made on Iron and its oxides, and on an Iron Nickel alloy have clearly shown this effect. This type of information is not easily obtained from other methods of material analysis. However, much theoretical and experimental work needs to be done before the features observed in the appearance potential spectra can be properly characterized.

Because of poor signal to noise ratio at low levels, electron currents in the range of a milliampere from a flood source were normally required in the experiments. Although sample spectra were produced at a current of 15 μA, the need for a multiplier tube worsened the already poor signal to noise ratio to the point where finer details were submerged. The prospects of using a finely focused electron beam are not bright in the present apparatus. Because of the absence of the bremsstrahlung with ion excitation, a focused beam of ions may provide a solution to the problem.

The present results indicate that the detection sensitivity of appearance potential spectroscopy is considerably inferior to that of other methods, and certain materials have not been detected at all by this method. It is hoped that further improvements such as ion excitation would considerably improve the sensitivity and versatility of this new and evolving technique.

APPENDIX

X-RAY ATOMIC ENERGY LEVELS[73,74]

a. In the order of Increasing Energy in the range 50 to 1000 eV

Element	Level	eV	Element	Level	eV	Element	Level	eV
76 Os	$N_{6,7}$	50	77 Ir	N_6	63	75 Re	O_1	82
53 I	$N_{4,5}$	51	11 Na	L_1	63	79 Au	N_7	83
46 Pd	$N_{2,3}$	51	54 Xe	$N_{4,5}$	63	25 Mn	M_1	84
67 Ho	O_1	51	77 Ir	O_2	63	76 Os	O_1	84
77 Ir	O_3	51	72 Hf	O_1	65	79 Au	N_6	86
78 Pt	O_3	51	23 V	M_1	67	82 Pb	O_3	86
12 Mg	$L_{2,3}$	51	88 Ra	$O_{4,5}$	67	30 Zn	$M_{2,3}$	87
40 Zr	N_1	51	28 Ni	$M_{2,3}$	67	90 Th	O_5	88
69 Tm	O_1	53	43 Te	N_1	68	12 Mg	L_1	89
70 Yb	O_1	54	35 Br	M_5	69	36 Ke	$M_{4,5}$	89
21 Sc	M_1	54	48 Cd	$N_{2,3}$	70	50 Sn	$N_{2,3}$	89
79 Au	O_3	54	35 Br	M_4	70	56 Ba	N_5	90
26 Fe	$M_{2,3}$	54	78 Pt	N_7	71	56 Ba	N_4	93
3 Li	K	55	73 Ta	O_1	71	82 Bi	O_3	93
47 Ag	N_3	56	92 U	P_1	71	26 Fe	M_1	93
34 Se	$M_{4,5}$	57	79 Au	O_2	72	91 Pa	$O_{4,5}$	94
71 Lu	O_1	57	13 Al	$L_{2,3}$	73	90 Th	O_4	94
41 Nb	N_1	58	24 Cr	M_1	74	47 Ag	N_1	95
76 Os	O_2	58	29 Cu	$M_{2,3}$	74	92 U	O_5	96
80 Hg	O_3	58	78 Pt	N_6	74	51 Sb	$N_{2,3}$	98
87 Fr	O_4	58	44 Ru	N_1	75	57 La	$N_{4,5}$	99
22 Ti	M_1	60	47 In	$N_{2,3}$	77	80 Hg	N_7	99
77 Ir	N_7	60	55 Cs	N_5	77	81 Tl	O_2	100
68 Er	O_1	60	74 W	O_1	77	14 Si	$L_{2,3}$	101
27 Co	$M_{2,3}$	60	55 Cs	N_4	79	27 Co	L_1	101
77 Ir	$N_{6,7}$	61	89 Ac	$O_{4,5}$	80	78 Pt	O_1	102
42 Mo	N_1	62	45 Rh	N_1	81	80 Hg	N_6	102
47 Ag	N_2	63	80 Hg	O_2	81	31 Ga	M_3	103

Element	Level	eV
82 Pb	O_2	105
31 Ga	M_2	107
48 Cd	N_1	107
79 Au	O_1	108
52 Te	$N_{2,3}$	110
58 Ce	$N_{4,5}$	110
4 Be	K	111
37 Rb	M_4	111
28 Ni	M_2	112
37 Rb	M_5	112
59 Pr	$N_{4,5}$	113
83 Bi	O_2	117
13 Al	L_1	118
60 Nd	$N_{4,5}$	118
81 Tl	N_7	119
29 Cu	M_1	120
61 Pm	$N_{4,5}$	120
80 Hg	O_1	120
49 In	N_1	122
53 I	$N_{2,3}$	122
81 Tl	N_6	123
32 Ge	M_2	128
62 Sm	$N_{4,5}$	129
15 P	$L_{2,3}$	132
38 Sr	M_5	133
63 Er	$M_{3,4}$	133
38 Sr	M_4	135
30 Zn	M_1	136
50 Sn	N_1	136
81 Tl	O_1	136
82 Pb	N_7	138
33 As	M_3	140
82 Pb	N_6	143
33 As	M_2	146
54 Xe	$N_{2,3}$	147
65 Tb	$N_{4,5}$	147
82 Pb	O_1	147
14 Si	L_1	149
51 Sb	N_1	152
88 Ra	O_3	152
66 Dy	$N_{4,5}$	154
38 Y	M_5	157
83 Bi	N_7	157
31 Ga	M_1	158
83 Bi	O_1	159
39 Y	M_4	160
67 Ho	$N_{4,5}$	161
83 Bi	N_6	161
34 Se	M_3	162
55 Cs	N_3	162
16 S	$L_{2,3}$	165
34 Se	M_2	168
52 Te	N_1	168
68 Er	N_5	168
55 Cs	N_2	172
68 Er	N_4	177
32 Ge	M_1	180
40 Zr	M_5	180
56 Ba	N_3	180
69 Tm	$N_{4,5}$	180
35 Br	M_3	181
40 Zr	M_4	182
90 Th	O_3	182
70 Yb	N_5	184
53 I	N_1	186
5 B	K	188
15 P	L_1	189
35 Br	M_2	189
57 La	N_3	191
56 Ba	N_2	192
71 Lu	N_5	195
72 U	O_3	195
70 Yb	N_4	198
17 Cl	L_3	200
88 Ra	O_2	200
17 Cl	L_2	202
33 As	M_1	204
41 Nb	M_5	204
57 La	N_2	205
71 Lu	N_4	205
41 Nb	M_4	207
58 Ce	N_3	207
36 Kr	M_3	214
59 Pr	N_3	218
91 Pa	$O_{2,3}$	222
36 Ke	O_2	223
58 Ce	N_2	223
60 Nd	N_3	225
42 Mo	M_5	227
16 S	$L_{2,3}$	229
90 Th	O_2	229
42 Mo	M_4	230
55 Cs	N_1	231
34 Se	M_1	232
59 Pr	N_2	236
37 Rb	M_3	239
73 Ta	N_4	241
61 Pm	$N_{2,3}$	242
60 Nd	N_2	243

Element	Level	eV
18 Ar	L_3	245
74 W	N_4	245
62 Sm	N_3	247
18 Ar	L_2	247
37 Rb	M_2	247
43 Tc	M_5	253
56 Ba	N_1	253
88 Ra	O_1	254
43 Tc	M_4	256
35 Br	M_1	257
63 Eu	N_3	257
74 W	N_4	259
92 U	O_2	259
75 Re	N_5	260
62 Sm	N_2	266
38 Sr	M_3	269
17 Cl	L_1	270
57 La	N_1	270
64 Gd	N_3	271
76 Os	N_5	273
75 Re	N_4	247
44 Ru	M_5	279
38 Sr	M_2	280
6 C	K	284
63 Eu	N_2	284
44 Ru	M_4	284
64 Gd	N_2	289
76 Os	N_4	289
58 Ce	N_1	290
90 Th	O_1	290
19 K	L_3	293
66 Dy	N_3	293
77 Ir	N_5	295
19 K	L_2	296
88 Ra	$N_{6,7}$	299
39 Y	M_3	300
59 Pr	N_1	305
45 Rh	M_5	307
67 Ho	N_3	307
65 Tb	N_2	310
91 Pa	O_1	310
77 Ir	N_4	311
39 Y	M_2	312
45 Rh	M_4	312
78 Pt	N_5	313
60 Nd	N_1	315
18 Ar	L_1	320
68 Er	N_3	320
37 Rb	M_1	322
92 U	O_1	324
40 Zr	M_3	331
78 Pt	N_4	331
66 Dy	N_2	332
46 Pd	M_5	334
79 Au	N_5	334
90 Th	N_1	335
69 Tm	N_3	336
46 Pd	M_4	340
67 Ho	M_2	344
70 Yb	N_3	344
90 Th	N_6	344
62 Sm	N_1	346
20 Ca	L_3	346
20 Ca	L_2	350
79 Au	N_4	352
38 Sr	M_1	358
71 Lu	N_3	359
91 Pa	N_7	359
63 Eu	N_1	360
80 Hg	N_5	360
41 Nb	M_3	363
68 Er	N_2	366
47 Ag	M_5	367
91 Pa	N_6	371
47 Ag	M_4	372
64 Gd	N_1	376
19 K	L_1	377
41 Nb	M_2	378
80 Hg	N_4	378
72 Hf	N_3	380
92 U	N_7	381
65 Tb	N_3	385
81 Tl	N_5	386
92 U	N_6	391
42 Mo	M_3	392
39 Y	M_1	394
70 Yb	N_2	397
65 Tb	N_1	398
7 N	K	402
48 Cd	M_5	404
73 Ta	N_3	405
21 Sc	L_2	406
81 Tl	N_4	407
42 Mo	M_3	410
71 Lu	N_2	410
82 Pb	N_5	413
48 Cd	M_4	413
66 Dy	N_1	416
43 Tc	M_3	425

Element	Level	eV	Element	Level	eV	Element	Level	eV
74 W	N_3	425	78 Pt	N_3	519	23 V	L_1	628
40 Zr	M_1	530	23 V	L_2	521	53 I	M_4	631
82 Pb	N_4	435	45 Rh	M_2	521	88 Ra	N_4	636
72 Hf	N_2	437	51 Sb	M_4	527	25 Mn	L_3	644
67 Ho	N_1	437	46 Pd	M_3	531	82 Pb	N_3	645
20 Ca	L_1	437	8 O	K	532	48 Cd	M_2	650
83 Bi	N_5	440	85 At	N_4	583	25 Mn	L_2	651
49 In	M_5	443	51 Sb	M_4	536	76 Os	N_1	654
75 Re	N_3	444	72 Hf	N_1	538	49 In	M_3	664
43 Tc	M_2	445	79 Au	N_3	545	46 Pd	M_1	670
68 Er	N_1	449	76 Os	N_2	547	54 Xe	M_4	672
49 In	M_4	451	46 Pd	M_2	559	89 Ac	N_4	675
22 Ti	L_3	455	22 Ti	L_1	564	90 Th	N_5	676
44 Ru	M_3	460	73 Ta	N_1	566	80 Hg	N_2	677
22 Ti	L_2	461	86 Rn	N_4	567	83 Bi	N_3	679
83 Bi	N_4	463	47 Ag	M_3	571	9 F	K	685
73 Ta	N_2	465	80 Hg	N_3	571	77 Ir	N_1	690
41 Nb	M_1	468	52 Te	M_5	572	25 Cr	L_1	695
76 Os	N_3	468	24 Cr	L_3	575	49 In	M_2	702
69 Tm	N_1	472	77 Ir	N_2	577	84 Po	N_3	705
44 Ru	M_2	482	87 Fr	N_5	577	26 Fe	L_3	708
50 Sn	M_5	484	52 Te	M_4	583	91 Pa	N_5	708
70 Yb	N_1	487	24 Cr	L_2	584	50 Sn	M_3	714
74 W	N_2	492	44 Ru	M_1	585	90 Th	N_4	714
50 Sn	M_4	493	74 W	N_1	595	47 Ag	M_1	717
77 Ir	N_3	494	47 Ag	M_2	602	26 Fe	L_2	721
45 Rh	M_3	496	87 Fr	N_4	603	81 Tl	N_2	721
21 Sc	L_1	500	78 Pt	N_2	609	78 Pt	N_1	722
84 Po	N_4	500	81 Tl	N_3	609	55 Cs	M_5	725
42 Mo	M_1	505	48 Cd	M_3	616	92 U	N_5	738
71 Lu	N_1	506	53 I	M_5	619	55 Cs	M_4	739
23 V	L_3	513	75 Re	N_1	625	85 At	N_3	740
75 Re	N_2	518	45 Rh	M_1	627	91 Pa	N_4	743

Element	Level	eV
50 Sn	M_2	756
79 Au	N_1	759
82 Pb	N_2	764
51 Sb	N_3	765
86 Rn	N_3	768
25 Mn	L_1	769
48 Cd	M_1	770
92 U	N_4	780
56 Ba	M_5	781
27 Co	L_3	779
27 Co	L_2	794
56 Ba	M_4	796
80 Hg	N_1	800
83 Bi	N_2	805
87 Fr	N_3	810
51 Sb	M_2	811
49 In	M_1	825
80 Hg	N_1	825
57 La	M_5	832
26 Fe	L_1	846
57 La	M_4	848
84 Po	N_2	851
28 Ni	L_3	855
10 Ne	K	867
52 Te	M_2	870
28 Ni	L_2	871
53 I	M_3	875
88 Ra	N_3	879
58 Ce	M_5	883
50 Sn	M_1	884
85 At	N_2	886
89 Ac	N_3	890
82 Pb	N_1	894

Element	Level	eV
58 Ce	M_4	901
27 Co	L_1	926
86 Rn	N_2	929
59 Pr	M_5	931
53 I	M_2	831
29 Cu	L_3	931
54 Xe	M_3	937
83 Bi	N_1	938
51 Sb	M_1	943
29 Cu	L_2	951
59 Pr	M_4	951
90 Th	N_3	967
60 Nd	M_5	978
87 Fr	N_2	980
84 Po	N_1	995
55 Cs	M_3	999
60 Nd	M_4	1000

b. In the order of increasing atomic number (50 to 1000 eV range)*

Level	1 H	2 He	3 Li	4 Be	5 B	6 C	7 N	8 O
K	13.6	24.6	55	111	188	284	402	532
	9 F	10 Ne	11 Na	12 Mg	13 Al	14 Si	15 P	16 S
K	685	867						
L_1			63	89	117	149	189	229
$L_{2,3}$				51	73	100	132	165
	17 Cl	18 Ar	19 K	20 Ca	21 Sc	22 Ti	23 V	24 Cr
L_1	270	320	377	438	500	564	628	694
L_2	202	247	296	350	407	462	521	584
L_3	200	245	294	346	402	456	513	575
M_1					54	60	67	74
	25 Mn	26 Fe	27 Co	28 Ni	29 Cu	30 Sn	31 Ga	32 Ge
L_1	769	846	926					
L_2	651	721	794	872	951			
L_3	640	708	779	855	931			
M_1	94	93	101	112	120	135	158	180
M_2		54	60	68	74	87	107	128
M_3		54	60	68	74	87	103	121
	33 As	34 Se	35 Br	36 Kr	37 Rb	38 Sr	39 Y	40 Zr
M_1	204	232	257		322	358	384	430
M_2	146	168	189	223	247	280	312	344
M_3	141	162	182	214	239	269	300	330
M_4		57	70	89	112	135	160	182
M_5		57	69	89	110	133	157	180
N_1								51

* Energy values outside the range 50 to 1000 eV are excluded from this tabulation

Level*	41 Nb	42 Mo	43 Tc	44 Ru	45 Rh	46 Pd	47 Ag	48 Cd
M_1	468	504		585	627	670	718	770
M_2	378	410	445	483	521	559	602	651
M_3	363	392	425	461	496	532	571	617
M_4	207	227	253	279	307	335	367	404
N_1	58	61		75	81	86	95	108
N_2						51	63	67
N_3						51	56	67

	49 In	50 Sn	51 Sb	52 Te	53 I	54 Xe	55 Cs	56 Ba
M_1	826	884	944					
M_2	702	756	812	870	931	999		
M_3	664	714	766	819	875	937	998	
M_4	451	493	537	583	631		740	796
M_5	443	485	528	572	619	672	726	781
N_1	122	137	152	168	186		231	253
N_2	77	89	98	110	123	147	172	192
N_3	77	89	98	110	123	147	162	180
N_4							79	93
N_5							77	90

	57 La	58 Cs	59 Pr	60 Nd	61 Pm	62 Sm	63 Eu	64 Gd
M_4	849	901	951	1000				
M_5	832	883	931	978				
N_1	270	290	305	315		346	360	376
N_2	206	223	236	243	242	266	284	289
N_3	191	207	218	225	242	247	257	271
$N_{4,5}$	99	110	113	118	120	129	133	141

* Energy values outside the range 50 to 1000 eV are excluded from this tabulation

Level*	.65 Tb	66 Dy	67 Ho	68 Er	69 Tm	70 Yb	71 Lu	72 Hf
N_1	398	416	436	449	471	487	506	538
N_2	310	332	344	366	386	397	410	437
N_3	385	293	307	320	337	343	359	380
N_4	147	154	161	177	180	198	205	224
N_5	147	154	161	168	180	185	195	214
O_1		63	51	60	53	54	57	65
	73 Ta	74 W	75 Re	76 Os	77 Ir	78 Pt	79 Au	80 Hg
N_1	566	595	635	654	690	722	759	800
N_2	465	492	518	547	577	609	644	677
N_3	405	425	444	468	494	519	545	571
N_4	241	259	274	289	311	331	352	378
N_5	229	245	260	273	295	313	334	360
N_6					63	74	86	102
N_7					61	71	83	99
O_1		77		84	95	102	108	120
O_2				58	63	65	71	80
O_3					51	52	54	58
	81 Tl	82 Pb	83 Bi	84 Po	85 At	86 Rn	87 Fr	88 Ra
N_1	846	894	938	995				
N_2	721	764	805	851	886	929	980	
N_3	609	644	679	705	740	768	810	879
N_4	407	435	464	500	533	567	603	636
N_5	386	413	440	473			577	603
N_6	123	143	162					299
N_7	119	138	157					254

* Energy values outside the range 50 to 1000 eV are excluded from this tabulation

Level	81 Tl	82 Pb	83 Bi	84 Po	85 At	86 Rn	87 Fr	88 Ra
O_1	136	147	159					254
O_2	100	105	117					200
O_3	75	86	93					153
$O_{4,5}$								67

	89 Ac	90 Th	91 Pa	92 U
N_3	890	967		
N_4	675	714	743	780
N_5		676	708	738
N_6		344	371	391
N_7		335	360	381
O_1		290	310	324
O_2		229	223	259
O_3		182	223	195
O_4		94	94	105
O_5		88	94	96
P_1		60		71

* Energy values outside the range 50 to 1000 eV are excluded from this tabulation

REFERENCES

1. O. W. Richardson and C.B. Bazzoni, Phil. Mag., 42, 1015 (1921)
2. E. H. Kurth, Phys. Rev., 18, 461 (1921)
3. A. Ll Hughes, Phil. Mag., 43, 145 (1922)
4. P. Holweck, Ann. de Chimie et de Physique, 17, 5 (1922)
5. Mohler and Foote, Sci. Papers of the Bureau of Standards, 425 (1921)
6. J. Holtsmark, Phys. Zeits., 23, 252 (1922)
7. McLennan and Clark, Roy. Soc. Proc., A 102, 389 (1923)
8. Horton, Andrews and Davis, Phil. Mag., 46, 721 (1923)
9. P. Lukirskii, Phil. Mag., 47, 466 (1924)
10. Bazzoni and Chu, Journ. Franklin Inst., 183 (1924) Feb.
11. G. K. Rollefson, Phys. Rev., 23, 35 (1924)
12. J. C. Boyce, Phys. Rev., 23, 575 (1924)
13. M. Levi, Trans. R. S. Canada, 18, 159 (1924)
14. J. A. Becker, Phys. Rev., 24, 478 (1924)
15. C. H. Thomas, Phys. Rev., 25, 322 (1925)
16. C. H. Thomas, Phys. Rev., 26, 739 (1925)
17. Stuhlman, Science, 56, 344 (1922)
18. O. W. Richardson and F. C. Chalklin, Proc. Roy. Soc., 110A, 247 (1926)
19. Andrews, Davies and Horton, Phil. Mag., 2, 1253 (1926)
20. Andrews, Davies and Horton, Proc. Roy. Soc., 117A, 649 (1928)
21. Compton and Thomas, Phys. Rev., 28, 601 (1926)
22. H. W. B. Skinner, Roy. Soc. Lond. Proc., 135A, 84 (1932)
23. G. Shinoda, T. Suzuki and S. Kato, J. Phys. Soc. Jap., 7, 44 (1952)

24. T. Shinoda, T. Suzuki and S. Kato, Technology Report of the Osaka University, 4, 1 (1954)

25. G. Shinoda, T. Suzuki and S. Kato, Phys. Rev., 95, 840 (1954)

26. R. Voparil, J. Phys. E: Sci. Instr., 3, 798 (1970)

27. R. L. Park, J. E. Houston and D. G. Shreiner, Rev. Sci. Inst. 41, 1810 (1970)

28. J. E. Houston and R. L. Park, J. Vac. Sci. Tech., 8, 91 (1971)

29. R. L. Park and J. E. Houston, Surf. Sci., 26, 664 (1971)

30. R. L. Park and J. E. Houston, Report of the Sandia Laboratories, New Mexico, 1970. Also, Solid State Comm. 10, 91 (1972)

31. V. E. Cosslett and W. C. Nixon, *X-ray Microscopy*, Cambridge University Press, 1960

32. A. E. Sandstrom, Handb. Phys., 30, 78 (1957)

33. Borovskii, *private communication*

34. D. W. Aitken, IEEE Trans. Nucl. Sci., NS-15, 10 (1968)

35. P. B. Sewel, *private communication*

36. B. L. Henke and R. E. Lent, *Advances in X-ray Analysis*, 480 (1969), Plenum Press, N. Y.

37. A. H. McIlraith, J. Sci. Instr., 39, 504 (1962)

38. J. J. Grodski, Norelco Reporter, 14, 107 (1967)

39. J. J. Grodski and B. W. Schumacher, Rev. Sci. Instr., 39, 702 (1968)

40. R. W. Bauer and R. C. Weingart, IEEE Trans. Nucl. Sci., NS-15, 147 (1968)

41. A. P. Lukirskii, Rumsh and Smirnov, Optics and Spectr. (USSR), 9, 265 (1968)

42. Lukirskii, Rumsh and Karpovich, Optics and Spectr. (USSR), 9, 343 (1960)

43. Rumsh, Lukirskii and Shchemetev, Soviet Physics, Doklady 5, 1231 (1960)

44. Manson, Hinteregger and McMahon, J. Opt. Soc. Am., 55, 103 (1965)

45. C. C. Chang, Surf. Sci, 25, 53 (1971)

46. J. C. Tracy, Appl. Phys. Let., 19, 353 (1971)

47. D. H. Tamboulian, Handb. Phys., 30, 246 (1957)

48. P. A. M. Dirac, *Principles of Quantum Mechanics*, 3rd ed., 245, Oxford Univ.

49. B. Dev and H. Brinkman, Nederlands Tijdschrift Voor Vacuum-techiek, 8, 176 (1970)

50. R. L. Park and J. E. Houston, Phys. Rev. B, to be published

51. C. Kittel, *Introduction to Solid State Physics*, 3rd ed., 232, J. Wiley

52. Arakawa, Herickhoff and Birkhoff, Phys. Rev. Let., 12, 319 (1964)

53. G. E. Laramore, Solid State Comm., 10, 85 (1972)

54. V. E. Cosslett, *X-ray Microscopy and X-ray Microanalysis*, 346 Amsterdam, 1960

55. H. E. Bishop and J. C. Riviere, J. App. Phys., 40, 1740 (1969)

56. Archard, *X-ray Microscopy and X-ray Microanalysis*, 331, Amsterdam, 1960

57. Campbell, Proc. Roy. Soc. A(G.B.), 274, 319 (1963)

58. Dolby, Brit. J. App. Phys., 11 64 (1960)

59. J. E. Houston and R. L. Parm, Sol. St. Comm., 10, 91 (1972)

60. P. B. Sewel, *Private communication*

61. J. E. Holliday, *Advances in X-ray Analysis*, 13, 136 (1970), Plenum Press, N. Y.

62. P. A. Redhead, *private communication*

63. S. T. Stephenson, Handb. Phys., 30, 337 (1957)

64. P. A. Redhead and G. W. Richardson, J. Appl. Phys., 43, 2970 (1972)

65. T. W. Haas, S. Thomas and G. J. Dooley, Surf. Sci., 28, 645 (1971)

66. J. E. Houston and R. L. Park, *unpublished*

67. R. L. Park, J. E. Houston and D. G. Shreiner, J. Vac. Sci. Tech., 9, 1023 (1972)

68. R. G. Musket, J. Vac. Sci. Tech., 9, 603 (1972)

69. J. E. Houston and R. L. Park, *unpublished*

70. J. E. Houston and R. L. Park, *unpublished*

71. R. L. Park and J. E. Houston, *unpublished*

72. R. L. Park and J. E. Houston, *unpublished*

73. J. A. Beardon and A. F. Burr, Rev. Mod. Phys., 39, 125 (1967)

74. K. Siegbahn, *Alpha-, Beta-, and Gamma-Ray Spectroscopy*, North-Holland Publ. Co., Amsterdam, 1965

PUBLICATION

C. D. Cox and K. N. Ramachandran, *An Energy Modulated Electron Probe Analysis Technique*, paper presented at the 70th Annual Convention of the Canadian Ceramic Society, Feb. 1972, Quebec City

EDUCATIONAL BACKGROUND

Degree Obtained	Year	University
B Sc.(Engineering) Electrical Engineering	1961	University of Kerala Trivandrum, India
M Sc.(Engineering) Electrical Machine Design	1963	University of Kerala Trivandrum, India
M. Tech. Applied Electronics	1967	Indian Institute of Technology, Bombay

NAME: KOVILVILA NARAYANA RAMACHANDRAN